



AFRL-RB-WP-TR-2008-3032

HIGH-ORDER METHODS FOR WAVE PROPAGATION

Miguel R. Visbal, Scott E. Sherer, and Michael D. White

**Computational Sciences Branch
Aeronautical Sciences Division**

**JANUARY 2008
Final Report**

Approved for public release; distribution unlimited.

See additional restrictions described on inside pages

STINFO COPY

**AIR FORCE RESEARCH LABORATORY
AIR VEHICLES DIRECTORATE
WRIGHT-PATTERSON AIR FORCE BASE, OH 45433-7542
AIR FORCE MATERIEL COMMAND
UNITED STATES AIR FORCE**

NOTICE AND SIGNATURE PAGE

Using Government drawings, specifications, or other data included in this document for any purpose other than Government procurement does not in any way obligate the U.S. Government. The fact that the Government formulated or supplied the drawings, specifications, or other data does not license the holder or any other person or corporation; or convey any rights or permission to manufacture, use, or sell any patented invention that may relate to them.

This report was cleared for public release by the Air Force Research Laboratory Wright-Patterson Air Force Base (AFRL/WPAFB) Public Affairs Office and is available to the general public, including foreign nationals. Copies may be obtained from the Defense Technical Information Center (DTIC) (<http://www.dtic.mil>).

AFRL-RB-WP-TR-2008-3032 HAS BEEN REVIEWED AND IS APPROVED FOR PUBLICATION IN ACCORDANCE WITH ASSIGNED DISTRIBUTION STATEMENT.

//Signature//

Miguel R. Visbal, Technical Area Leader
Computational Sciences Branch
Aeronautical Sciences Division

//Signature//

Reid B. Melville, Chief
Computational Sciences Branch
Aeronautical Sciences Division

//Signature//

Matthew Burkinshaw, Technical Advisor
Computational Sciences Branch
Aeronautical Sciences Division

This report is published in the interest of scientific and technical information exchange, and its publication does not constitute the Government's approval or disapproval of its ideas or findings.

*Disseminated copies will show “//Signature//” stamped or typed above the signature blocks.

REPORT DOCUMENTATION PAGE				<i>Form Approved</i> OMB No. 0704-0188	
The public reporting burden for this collection of information is estimated to average 1 hour per response, including the time for reviewing instructions, searching existing data sources, gathering and maintaining the data needed, and completing and reviewing the collection of information. Send comments regarding this burden estimate or any other aspect of this collection of information, including suggestions for reducing this burden, to Department of Defense, Washington Headquarters Services, Directorate for Information Operations and Reports (0704-0188), 1215 Jefferson Davis Highway, Suite 1204, Arlington, VA 22202-4302. Respondents should be aware that notwithstanding any other provision of law, no person shall be subject to any penalty for failing to comply with a collection of information if it does not display a currently valid OMB control number. PLEASE DO NOT RETURN YOUR FORM TO THE ABOVE ADDRESS.					
1. REPORT DATE (DD-MM-YY) January 2008		2. REPORT TYPE Final		3. DATES COVERED (From - To) 31 October 1994 – 30 September 2002	
4. TITLE AND SUBTITLE HIGH-ORDER METHODS FOR WAVE PROPAGATION				5a. CONTRACT NUMBER In-house	
				5b. GRANT NUMBER	
				5c. PROGRAM ELEMENT NUMBER 0601102	
6. AUTHOR(S) Miguel R. Visbal and Scott E. Sherer (AFRL/RBAC) Michael D. White (Ohio Aerospace Institute)				5d. PROJECT NUMBER A04Y	
				5e. TASK NUMBER	
				5f. WORK UNIT NUMBER 0A	
7. PERFORMING ORGANIZATION NAME(S) AND ADDRESS(ES) Computational Sciences Branch (AFRL/RBAC) Aeronautical Sciences Division Air Force Research Laboratory, Air Vehicles Directorate Wright-Patterson Air Force Base, OH 45433-7542 Air Force Materiel Command, United States Air Force				8. PERFORMING ORGANIZATION REPORT NUMBER AFRL-RB-WP-TR-2008-3032	
9. SPONSORING/MONITORING AGENCY NAME(S) AND ADDRESS(ES) Air Force Research Laboratory Air Vehicles Directorate Wright-Patterson Air Force Base, OH 45433-7542 Air Force Materiel Command United States Air Force				10. SPONSORING/MONITORING AGENCY ACRONYM(S) AFRL/RBAC	
				11. SPONSORING/MONITORING AGENCY REPORT NUMBER(S) AFRL-RB-WP-TR-2008-3032	
12. DISTRIBUTION/AVAILABILITY STATEMENT Approved for public release; distribution unlimited.					
13. SUPPLEMENTARY NOTES PAO Case Number: WPAFB 08-0122, 22 Jan 2008. Report contains color.					
14. ABSTRACT In order to meet the demanding accuracy requirements in the simulation of wave propagation phenomena, a numerical approach based on high-resolution spatial schemes is presented. The time-domain AFRL code, FDL3DI, solves either the time-dependent Maxwell's equations (for CEM) or the Euler equations (for acoustics) employing 6th-order accurate compact-differences and low-pass spatial filters of up to 10th-order accuracy. The solver has been made applicable to general curvilinear grids through the incorporation of a careful treatment of the coordinate transformation metrics. In addition, the method has been extended to multi-body scattering applications through the use of overset grids and high-order interpolation. A robust absorbing boundary condition exploiting the transfer function of the low-pass filter has been developed. To evaluate the solver, several benchmark problems have been considered. Application to communication through weakly ionized plasma has also been studied.					
15. SUBJECT TERMS					
16. SECURITY CLASSIFICATION OF:			17. LIMITATION OF ABSTRACT: SAR	18. NUMBER OF PAGES 76	19a. NAME OF RESPONSIBLE PERSON (Monitor) Miguel R. Visbal 19b. TELEPHONE NUMBER (Include Area Code) N/A
a. REPORT Unclassified	b. ABSTRACT Unclassified	c. THIS PAGE Unclassified			

Contents

1	SUMMARY	1
2	INTRODUCTION	3
3	METHODS AND PROCEDURES	5
3.1	Governing Equations	5
3.2	Numerical Procedure	5
4	COMPUTATIONAL AEROACOUSTICS	11
4.1	Introduction	11
4.2	Governing Equations	11
4.3	Results	12
5	PREPROCESSING TOOLS FOR HIGH-ORDER OVERSET-GRIDS	33
5.1	Introduction	33
5.2	Preprocessing Elements	33
5.3	Flow Solver	42
5.4	Examples	43
6	COMMUNICATION THROUGH PLASMA	47
6.1	Introduction	47
6.2	Non-Dimensionalization of Governing Equations	47
6.3	Hypersonic Model	49
6.4	Results	51
7	CONCLUSIONS	57
	REFERENCES	59
	NOMENCLATURE	63

List of Figures

3.1	Incoming wave showing effect of scattered and total field zones.	8
3.2	Spectral function of some near-boundary filter formulas at point 2	10
4.1	Schematic of vertical 5-point mesh overlap for multi-domain applications	13
4.2	Mesh with abrupt change in spacing	14
4.3	Propagation of 1-D pulse through sudden mesh coarsening with <i>E2</i> scheme and without filter.	14
4.4	Propagation of 1-D pulse through sudden mesh coarsening with <i>C6F8</i> scheme.	14
4.5	Propagation of 2-D pressure pulse on smoothly-stretched Cartesian mesh: (a) grid, (b) unfiltered <i>C6</i> and (c) filtered <i>C6F10</i> results	16
4.6	Effect of high-order filter on computed pressure along $y = 0$ at $t = 4.5$ for the 2-D acoustic pulse propagation of Fig. 4.5.	17
4.7	Computation of 2-D acoustic source on mesh with abrupt stretching. (a) Grid (b) Pressure contours (c) Pressure along diagonal	17
4.8	Pressure at $x = 2$, $y = 2$ for 2-D pulse propagation on mesh with abrupt stretching. a) Pressure history, b) discrepancy between stretched and uniform grid solutions	18
4.9	Propagation of a vortical disturbance at 45° to the horizontal. a) Grid. Contours of perturbation velocity magnitude at b) $t=2$, c) $t=6$ and d) $t=8$	19
4.10	Perturbation velocity magnitude along diagonal for convecting vortical disturbance. Symbols and lines denote computed and exact solutions respectively	19
4.11	Pressure contours at various instants for acoustic pulse scattered by a circular cylinder	20
4.12	History of pressure at point 'A' on Grid <i>G2</i> for scattered pulse	20
4.13	History of pressure at point 'C' on Grid <i>G2</i> for scattered pulse	21
4.14	History of pressure at point 'A' on Grid <i>G1</i> for scattered pulse	21
4.15	Pressure history at a point for periodic acoustic source problem	22
4.16	Interference pattern due to scattering by a cylinder of periodic acoustic source	23
4.17	Computed directivity of radiated sound at $r/D = 5$ with <i>C6F10</i>	24
4.18	Computed directivity of radiated sound at $r/D = 10$ with <i>C6F10</i>	24
4.19	Effect of scheme on computed directivity at $r/D = 5$	25
4.20	Effect of filter boundary treatment on directivity at $r/D = 5$. HO=Higher order boundary formulas, LOC=Lower-order centered, OLOC=Optimized lower-order centered	26
4.21	Comparison of (a) implicit and (b) explicit near-boundary high-order filters	26
4.22	Schematic of mesh overlap for multi-domain cylinder scattering problem	27
4.23	Pressure contours for multi-domain scattering simulation in vicinity of mesh overlap region	28
4.24	Comparison of directivity at $r/D = 5$ for multi-domain and single-domain calculations	29
4.25	Three-dimensional spherical pulse. (a) Mesh, (b) and (c) Pressure contours with standard and new metrics respectively	30
4.26	Effect of metric evaluation on computed pressure along line through spherical pulse at $t = 10$	31
5.1	Workflow diagram for the high-order overset-grid process.	34
5.2	Situations showing linkage between holes and minimum stencil sizes	35
5.3	Sample boundary condition input (to <i>PEGASUS</i>) and output (from <i>BELLERO</i>)	38
5.4	Example of intragrid boundary connectivity	40
5.5	Example of periodic O-grid boundary connectivity	40

5.6	Example of intergrid boundary connectivity	41
5.7	Results from acoustic scattering validation problem	44
5.8	Overset grid system used for scattering from sphere	46
5.9	Results for EM scattering from sphere	46
6.1	Comparison of electron density along the stagnation line with original and modified free-stream values. Distance is normalized by nose radius ($R_n=15.24$ cm).	50
6.2	Comparison of atomic oxygen on surface of vehicle for fully catalytic walls.	52
6.3	Plasma shielding incoming 9 GHz wave. Left: no plasma, right: plasma	52
6.4	Comparison of electron density profile normal to antenna location #2 with catalytic and non-catalytic boundary conditions.	53
6.5	RAM C-II re-entry vehicle with locations of various antennas (ref: <i>NASA TN D-6062</i>). . . .	53
6.6	Computational grids. Left: RAM vehicle prior to decomposition. Right: Grid subset near location #2 for embedded horn.	54
6.7	Horn driven at 9.2 GHz from antenna location #2. Left: no plasma, right: plasma	54
6.8	Different frequencies and different configurations for radiation from location #2.	54
6.9	Magnitude of instantaneous electric field normal to the center of the radiating antenna for different time-steps and grid densities.	55

List of Tables

3.1	Coefficients for filter formula at interior points [1]. α_f is a free parameter in the range $0 < \alpha_f \leq 0.5$	9
3.2	Coefficient for 6th-order boundary filter formula at point 3	10
3.3	Coefficients for boundary filter formulas at point 2	10
4.1	Grid parameters for pulse scattering problem in region of interest ($r/D \leq 7$)	18
4.2	Grid parameters for source scattering problem, λ = spatial wavelength	22
5.1	Block decomposition data for acoustic scattering case (NP = number of processors, MBV = maximum block volume, SVR = average surface-to-volume ratio, MMR = minimum volume to maximum volume ratio)	45
5.2	Block decomposition data for electromagnetic scattering case (see Table 5.1 for column headings)	45

Chapter 1

SUMMARY

Advances in Air Force systems require commensurate advancement of the understanding of the pacing physics and technology challenges. Some of these challenges involve the propagation of wave phenomena through atmospheric media. Electro-magnetic responses are key to the performance of sensors and stealth technology. Acoustic responses will drive observability and component fatigue. The Air Force needs an advanced set of computational tools for computational discovery and numerical analysis of wave propagation as it relates to flight vehicle performance.

For the past 14 years, scientists in the Computational Sciences Branch of the Air Force Research Laboratory have systematically pursued a research program to develop, validate and demonstrate numerical approaches for computational electromagnetics/acoustics in the time domain. These efforts span research in high resolution techniques and methods for applying them to Air Force relevant challenges, as well as application to both canonical and representative configurations and regimes. This technical report documents the development and demonstration of high-order time-domain computational approaches for electromagnetics, acoustics and aero-optic applications. The methods and procedures for the numerics common to all applications are detailed in Chapter 3.

Chapter 4 of the report covers details of the high-order methodologies for accurate simulation of wave propagation phenomena in general configurations and though dispersive/non-homogeneous media. In order to accurately represent the wave propagation, a 6th-order field solver, *FDL3DI*, was developed that could retain the essential features of the wavefront. The impact of mesh stretching in the generation of high-frequency spurious modes is examined and the need for a discriminating higher-order filter procedure is established and resolved. The incorporation of these filtering techniques also permits a robust treatment of outflow radiation condition by taking advantage of energy transfer to high-frequencies caused by rapid mesh stretching. For conditions on the scatterer, higher-order one-sided filter treatments are shown to be superior in terms of accuracy and stability compared to standard explicit variations. Computations demonstrate that these algorithmic components are also crucial to the success of interface treatments created in multi-domain and domain-decomposition strategies. For three-dimensional computations, special metric relations are employed to assure the fidelity of the scheme in highly curvilinear meshes. A variety of problems, including several benchmark computations, demonstrate the success of the overall computational strategy.

Chapter 5 documents the critical extension of the methodology to overset grid systems. Overset grids allow the efficient and accurate representation of wave propagation of the complex geometry often associated with Air Force systems and their components. A new preprocessing code *BELLERO* has been developed to automate many of the tasks associated with domain decomposition for the parallel, high-order overset-grid (HO-OG) flow solver *FDL3DI*. The previous approach required considerable user involvement as well as manual modifications to the code to set up problems for processing using the parallel HO-OG algorithm. Highlighted capabilities of *BELLERO* include; (1) automatic generation of the grid indices for the domain decomposition, taking into account minimum stencil requirements for the high-order algorithm, (2) automatic generation of the block-level connectivity including periodic boundary conditions, (3) automated decomposition of the grid-level boundary conditions, thus eliminating the need to manually specify block-level boundaries in the code, and (4) calculation of high-order interpolation coefficients and management of hole points to fully implement the HO-OG approach. Improvements have also been made to the *FDL3DI* solver

itself in order to further enhance the overall flexibility of the HO-OG implementation. The new capability is validated using the benchmark problems of acoustic electromagnetic scattering.

Chapter 6 documents the culminating demonstration of the high-order methodology on a critical Air Force challenge: radio frequency propagation through ionized gases. Re-entry systems are engulfed in a plasma that interferes with the communication signals to and from the vehicle. This section includes details of the research required to characterize the distribution of ions in the plasma sheath and the construction of detailed grid system to represent both the flight vehicle and the horn antennae. The high-order, overset method was applied to the RAM-C re-entry configuration and flight conditions and representative results for the wave propagation response are detailed.

This report describes the development and successful demonstration of high-order methods for wave propagation for Air Force relevant challenges. In-house researchers in the Computational Sciences Branch of the Air Force Research Laboratory will exploit this new technology and extend the work in this area in pursuit of other Air Force priorities. The next phase of investigation will focus on the impact of aerodynamic degradation for directed energy weapons, using the tools and methods developed under this concluding project.

Chapter 2

INTRODUCTION

An important aspect of both civilian and military aircraft operation is the impact of aerodynamically generated sound on communities and structures. Examples of applications of current interest include weapon cavity acoustics, jet screech, sonic boom, cabin noise, and sound generated by blade/vortex interactions. In particular, the need to meet more stringent community noise level standards has resulted in increased attention being given to the relatively new field of time-domain computational aeroacoustics (CAA). CAA focuses on the accurate prediction of aerodynamic sound generated by airframe components and propulsion systems, as well as on its propagation and far-field characteristics. Both aspects of the problem (*i.e.*, sound generation and propagation) are extremely demanding from a time-domain computational standpoint due to the large number of grid points and small time-steps that are typically required. Therefore, for realistic aeroacoustic simulations to become more feasible, higher-order accurate and optimized numerical schemes are sought in order to reduce the required number of grid points per wavelength while still ensuring tolerable levels of numerically-induced dissipation and dispersion. These strict simulation requirements are shared by other time-domain linear wave propagation disciplines such as computational electromagnetics.

Recent reviews of computational aeroacoustics have been given by Tam [2] and Wells and Renaut [3] who discuss various numerical schemes currently popular in CAA. These include among others the dispersion-relation-preserving (DRP) scheme of Tam and Webb [4], the method for minimization of group velocity errors (MGV) due to Holberg [5], the family of high-order compact differencing schemes of Lele [6] and Essentially Non-Oscillatory (ENO) schemes [7]. The DRP, MGV and compact schemes are all centered non-dissipative schemes, a property which is desirable for linear wave propagation. However, the inherent lack of numerical dissipation may also result in spurious numerical oscillations and instability in practical applications involving general geometries, approximate boundary conditions or non-linear features. In the DRP approach for instance, artificial selective damping must be employed under these conditions [2]. While quite robust, standard upwind and upwind-biased formulations may be undesirable for situations involving linear wave propagation due to their excessive dissipation. To overcome this difficulty, higher-order upwind [8] or ENO approaches must be employed. The above spatial semi-discretizations are typically combined with high-order explicit time-integration methods such as the multi-stage Runge-Kutta procedure. In addition to the spatial and temporal discretizations, another critical aspect in CAA simulations is the accurate treatment of the physical and computational boundary conditions. A recent review of radiation, outflow and wall boundary treatments has been provided in Ref. [9].

This work effort focused on the development and evaluation of a high-order computational methodology for aeroacoustic and electromagnetic simulation on general geometries. There are two primary components to the algorithm chosen in the present work. The first refers to the differencing scheme, for which the choice rests primarily on Pade-type tridiagonal-based fourth- and sixth-order compact-difference formulas [6, 10]. As compared to explicit schemes, this approach incurs an increase in computational cost but lowers the dispersion error and reduces the number of points near the boundary where special formulations are required. As noted earlier, the non-dissipative nature of centered schemes make them susceptible to the unrestricted growth of spurious perturbations. The remedy employed here is based on filtering, which comprises the second and equally important component of the overall scheme. The filters considered in the present work are based on Padé-type formulas requiring the solution of tridiagonal systems of equations in the general

case. The expressions are taken from Ref. [1], where up to 10th-order filters were employed to stabilize finite-volume electromagnetics calculations, and have been successfully extended to solve the Navier-Stokes equations [11, 12, 13, 14]. The filtering strategies of Ref. [11] were also shown to be promising for simple aeroacoustic simulations on stretched Cartesian meshes [15].

To accurately simulate complex configurations, overset-grid methods[16] (also referred to as “Chimera” methods) are widely used today. The approach typically grids the entire computational domain using multiple overlapping structured component meshes. The use of overlapping component grids relieves many of the inherent limitations associated with structured grids when dealing with complex geometries. Overset grid methods have been shown to be an effective way of dealing with complex geometries[17, 18], moving-body problems[19], or providing a grid-adaptation capability[20]. A summary of current overset-grid research for a variety of applications may be found in Ref. [21].

High-order finite-difference methods[22, 23] for general curvilinear grids[24] using Padé-type formulations for the differencing and filtering operations[6] have also been employed to perform numerical simulations for a variety of problems. This approach has been shown to provide highly accurate results for computations involving turbulent flows[25, 26], aeroacoustics[27], electromagnetics[28, 1] and magnetogasdynamics[29]. Recently, this algorithm has been extended to handle general overset grids in order to provide additional flexibility to the algorithm for handling more complex geometries and to provide localized grid refinement.[30] This high-order overset-grid (HO-OG) approach has been validated against fundamental benchmark problems in turbulent flow[31], aeroacoustics[32] and electromagnetics[33].

Another longstanding problem for the military is the radio-blackout problem for re-entry vehicles. At high Mach numbers, the flow behind the shock can become hot enough to ionize the flow. This has long caused problems with communication and has been an active area of research for nearly half a century. The problem has been difficult to address because of the complexity of the chemistry during re-entry as well as the disparate length scales between the wavelength of the signal and the dimensions of the vehicle. A number of studies of transmission blackout were studied in the 1960s using rocket launched experimental probes. These tests, known as the Radio Attenuation Measurement or RAM-C tests attempted to measure the electron density and signal attenuation at hypersonic speeds [34, 35]. Recently progress has been made in simulating these sorts of non-equilibrium flows by Josyula and Bailey [36].

For simulating wave propagation in dispersive media, a common method is to use an auxiliary difference equation approach [37]. For simulating wave propagation through weak plasmas, a more physical model of the difference equation has been used with 4th-order FDTD by Young [38] and more recently a similar formulation with 3rd-order MUSCLE by Shang [39]. The current effort has applied the technology developed in simulation for acoustics and electromagnetics as well as the tools for overset-grid technology to investigate this problem.

Chapter 3

METHODS AND PROCEDURES

3.1 Governing Equations

In order to develop a procedure suitable for nonlinear aeroacoustic and plasma applications over complex configurations, the equations are cast in strong conservative form by introducing a general curvilinear coordinate transformation $(x, y, z) \longrightarrow (\xi, \eta, \zeta)$. In vector notation, these equations are:

$$\frac{\partial}{\partial t} \left(\frac{\mathbf{U}}{J} \right) + \frac{\partial \hat{\mathbf{F}}}{\partial \xi} + \frac{\partial \hat{\mathbf{G}}}{\partial \eta} + \frac{\partial \hat{\mathbf{H}}}{\partial \zeta} = \frac{\mathbf{S}}{J} \quad (3.1)$$

Here \mathbf{U} denotes the solution vector; J is the transformation Jacobian; $\hat{\mathbf{F}}, \hat{\mathbf{G}}, \hat{\mathbf{H}}$ are the fluxes and \mathbf{S} is a vector source term.

3.2 Numerical Procedure

A finite-difference approach is employed to discretize the above equations. All discrete quantities are therefore assumed to be pointwise in nature. This choice is motivated by the relative ease of formal extension to higher-order accuracy.

3.2.1 Differencing Scheme

For any scalar quantity, ϕ , such as a metric, flux component or flow variable, the spatial derivative ϕ' is obtained in the transformed plane by solving the tridiagonal system:

$$\alpha \phi'_{i-1} + \phi'_i + \alpha \phi'_{i+1} = b \frac{\phi_{i+2} - \phi_i - 2}{4} + a \frac{\phi_{i+2} - \phi_i - 2}{2} \quad (3.2)$$

where α , a and b determine the spatial properties of the algorithm. The formula yields the compact five-point, sixth-order $C6$, and three-point fourth-order $C4$ schemes with $\alpha = 1/3$, $a = 14/9$, $b = 1/9$ and $\alpha = 1/4$, $a = 3/2$, $b = 0$ respectively. Equation 3.2 also incorporates the standard explicit fourth-order E4 ($\alpha = 0$, $a = 4/3$ and $b = -1/3$) and second-order E2 ($\alpha = 0$, $a = 1$, $b = 0$) schemes. At boundary points 1, 2, $IL - 1$ and IL , higher-order one-sided formulas are utilized which retain the tridiagonal form of the equation set. These are described in more detail in Ref. [40].

The derivatives of the fluxes are obtained by first forming these fluxes at the nodes and subsequently differentiating each component with the above formulas.

3.2.2 Metric Evaluation

The extension of high-order schemes to non-trivial 3-D geometries demands that issues of freestream preservation and metric cancellation be carefully addressed. These errors, which arise in finite-difference discretizations of governing equations written in strong-conservation form, can catastrophically degrade the fidelity

of higher-order approaches. In Ref. [11], it was shown that on highly distorted curvilinear 2-D meshes, the compact scheme exhibits very small metric cancellation errors when the metrics are evaluated with the same finite-difference expressions as those employed for the fluxes. This work also clearly showed that the practice of prescribing analytic metrics on stretched curvilinear meshes can lead to unacceptable errors and therefore should in general be avoided.

The situation is far different in 3-D however. As discussed in Refs. [41] and [42] for the second-order scheme, the previous straightforward approach of calculating the metrics, although effective in 2-D, fails to provide metric cancellation for general 3-D curvilinear meshes. To illustrate this point, consider the metric relations:

$$\begin{aligned}\xi_x/J &= y_\eta z_\zeta - y_\zeta z_\eta \\ \eta_x/J &= y_\zeta z_\xi - y_\xi z_\zeta \\ \zeta_x/J &= y_\xi z_\eta - y_\eta z_\xi\end{aligned}\tag{3.3}$$

Associated with this component of the surface area vectors, there is the corresponding metric identity [42]

$$(\xi_x/J)_\xi + (\eta_x/J)_\eta + (\zeta_x/J)_\zeta = 0\tag{3.4}$$

which must be satisfied numerically to ensure freestream preservation. Similar relations exist for the other two components of the surface area vectors. Evaluation of the y and z derivatives in Eqn. 3.3 using explicit or compact centered schemes does not satisfy the identity of Eqn. 3.4. Therefore grid-induced errors may appear, for instance in regions of large grid variation or near singularities. Pulliam and Steger [41] introduced a simple averaging procedure which guarantees freestream preservation on general 3-D curvilinear meshes. This approach, which works very well for the 2nd-order scheme, is not readily extendable to higher-order formulations. An alternate method to enforce the metric identities consists in rewriting the metric expressions of Eqn. 3.3 prior to discretization in the equivalent “conservative” form[42]:

$$\begin{aligned}\xi_x/J &= (y_\eta z)_\zeta - (y_\zeta z)_\eta \\ \eta_x/J &= (y_\zeta z)_\xi - (y_\xi z)_\zeta \\ \zeta_x/J &= (y_\xi z)_\eta - (y_\eta z)_\xi\end{aligned}\tag{3.5}$$

with similar relations for the remaining metric terms. When the metric expressions of Eqn. 3.5 are adopted, and the derivatives are evaluated with the same high-order formulas employed for the fluxes, freestream preservation is again recovered in general 3-D curvilinear grids[12].

3.2.3 Time Integration

The equations are integrated in time with the classical fourth-order four-stage Runge-Kutta method. With R denoting the residual, the governing equation is:

$$\frac{\partial \mathbf{U}}{\partial t} = R = -J \left(\frac{\partial \hat{\mathbf{F}}}{\partial \xi} + \frac{\partial \hat{\mathbf{G}}}{\partial \eta} + \frac{\partial \hat{\mathbf{H}}}{\partial \zeta} - \frac{\mathbf{S}}{J} \right)\tag{3.6}$$

The classical four stage method integrates from time t_0 (step n) to $t_0 + \Delta t$ (step $n+1$) through the operations:

$$\begin{aligned}k_0 &= \Delta t R(\mathbf{U}_0) & k_1 &= \Delta t R(\mathbf{U}_1) \\ k_2 &= \Delta t R(\mathbf{U}_2) & k_3 &= \Delta t R(\mathbf{U}_3) \\ \mathbf{U}^{n+1} &= \mathbf{U}^n + \frac{1}{6}(k_0 + 2k_1 + 2k_2 + k_3)\end{aligned}\tag{3.7}$$

where $\mathbf{U}_0 = \mathbf{U}^n = \mathbf{U}(x, y, z, t_0)$, $\mathbf{U}_1 = \mathbf{U}_0 + k_0/2$, $\mathbf{U}_2 = \mathbf{U}_0 + k_1/2$ and $\mathbf{U}_3 = \mathbf{U}_0 + k_2$. The scheme is implemented in the low storage form described in Ref. [43] requiring three levels of storage.

3.2.4 Scattered Field / Total Field formulation

For many problems in (linear) acoustics and electromagnetics, it is desirable to be able to allow the incident waves to propagate from outside the domain. In order to model these waves, the solution is divided into what is known as total field and scattered field zones (TFZ/SFZ) [44, 45, 46]. In the typical TFZ/SFZ interface, the incident field is added or subtracted from the solution when the zonal interface is crossed. Consider the following discrete field distribution:

$$\mathbf{U}_j = \mathbf{U}_j^{scat}, \forall j < j_f \quad (3.8)$$

$$\mathbf{U}_j = \mathbf{U}_j^{tot}, \forall j > j_f \quad (3.9)$$

where j_f is the interface location located between two grid points and $\mathbf{U}^{tot} = \mathbf{U}^{scat} + \mathbf{U}^{inc}$. So for a simple central difference located at $j_f \pm \frac{1}{2}$ would give:

$$\partial_x \mathbf{U}^{scat} \Big|_{j_f - \frac{1}{2}} \approx \frac{\mathbf{U}_{j_f + \frac{1}{2}}^{total} - \mathbf{U}^{inc}(x = x_{j_f + \frac{1}{2}}) - \mathbf{U}_{j_f - \frac{1}{2}}^{scat}}{2\Delta x} \quad (3.10)$$

$$\partial_x \mathbf{U}^{total} \Big|_{j_f + \frac{1}{2}} \approx \frac{\mathbf{U}_{j_f + \frac{1}{2}}^{total} - \mathbf{U}_{j_f - \frac{1}{2}}^{scat} - \mathbf{U}^{inc}(x = x_{j_f - \frac{1}{2}})}{2\Delta x} \quad (3.11)$$

However, for high-order schemes, addition of this interface requires extensive modification to the compact stencils [47]. Instead, the current parallel version of the code utilizes the multiple grid paradigm to accomplish the zonal interface. In this formulation, each grid is designated as either a total field grid (ZONE=1) or a scattered field grid (ZONE=0). When the data is received from another grid, it is modified by:

$$Field = Field + (ZONE(current\ grid) - ZONE(donor\ grid)) * [Incident\ Field] \quad (3.12)$$

Figure 3.1 shows the flexibility of the zonal interfaces using grid.

As the imposed incident field is an analytical function in time, it has been shown that implementation of the field in the standard form for Runge-Kutta can introduce errors that reduce the temporal accuracy of the solution [48, 47]. In standard form, the Runge-Kutta stages would be:

$$\begin{aligned} k_0 &= \Delta t R(\mathbf{U}^{inc}(t_0), \mathbf{U}_0) & k_1 &= \Delta t R(\mathbf{U}^{inc}(t_0 + \Delta t/2), \mathbf{U}_1) \\ k_2 &= \Delta t R(\mathbf{U}^{inc}(t_0 + \Delta t/2), \mathbf{U}_2) & k_3 &= \Delta t R(\mathbf{U}^{inc}(t_0 + \Delta t), \mathbf{U}_3) \\ \mathbf{U}^{n+1} &= \mathbf{U}^n + \frac{1}{6}(k_0 + 2k_1 + 2k_2 + k_3) \end{aligned} \quad (3.13)$$

However, for linear problems the errors can be reduced [48, 47] if the incident field functions are replaced by the following analytical expression to match the truncation terms of the individual steps:

$$\begin{aligned} \mathbf{U}_0^{inc} &= \mathbf{U}^{inc}(t_0) \\ \mathbf{U}_1^{inc} &= \mathbf{U}^{inc}(t_0) + \frac{\Delta t}{2} \frac{\partial \mathbf{U}^{inc}}{\partial t}(t_0) \\ \mathbf{U}_2^{inc} &= \mathbf{U}^{inc}(t_0) + \frac{\Delta t}{2} \frac{\partial \mathbf{U}^{inc}}{\partial t}(t_0) + \frac{\Delta t^2}{4} \frac{\partial^2 \mathbf{U}^{inc}}{\partial t^2}(t_0) \\ \mathbf{U}_3^{inc} &= \mathbf{U}^{inc}(t_0) + \Delta t \frac{\partial \mathbf{U}^{inc}}{\partial t}(t_0) + \frac{\Delta t^2}{2} \frac{\partial^2 \mathbf{U}^{inc}}{\partial t^2}(t_0) + \frac{\Delta t^3}{4} \frac{\partial^3 \mathbf{U}^{inc}}{\partial t^3}(t_0) \end{aligned} \quad (3.14)$$

3.2.5 Interior filtering scheme

The filtering procedure forms an important component of the present centered algorithm since its function is to suppress numerical instabilities arising from unresolved scales, mesh non-uniformities and boundary conditions. If a typical component of the solution vector is denoted by ϕ , filtered values $\hat{\phi}$ satisfy,

$$\alpha_f \hat{\phi}_{i-1} + \hat{\phi}_i + \alpha_f \hat{\phi}_{i+1} = \sum_{n=0}^N \frac{a_n}{2} (\phi_{i+n} + \phi_{i-n}) \quad (3.15)$$

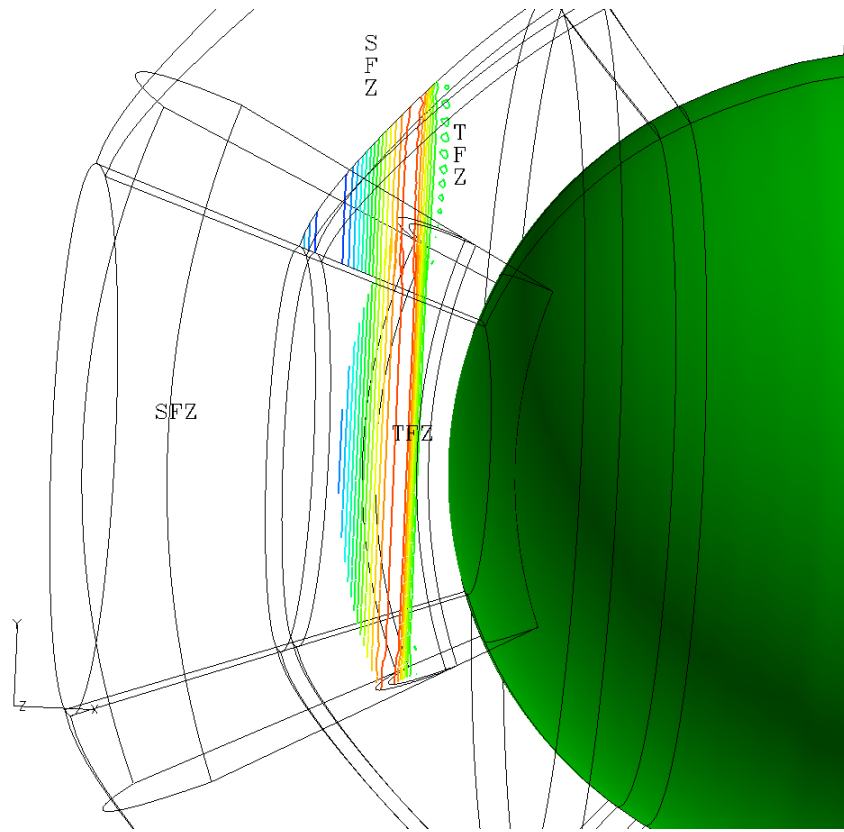


Figure 3.1: Incoming wave showing effect of scattered and total field zones.

Table 3.1: Coefficients for filter formula at interior points [1]. α_f is a free parameter in the range $0 < |\alpha_f| \leq 0.5$.

Scheme	a_0	a_1	a_2	a_3	a_4	a_5	OA
<i>F2</i>	$\frac{1}{2} + \alpha_f$	$\frac{1}{2} + \alpha_f$	0	0	0	0	2
<i>F4</i>	$\frac{5}{8} + \frac{3\alpha_f}{4}$	$\frac{1}{2} + \alpha_f$	$\frac{-1}{8} + \frac{\alpha_f}{4}$	0	0	0	4
<i>F6</i>	$\frac{11}{16} + \frac{5\alpha_f}{8}$	$\frac{15}{32} + \frac{17\alpha_f}{16}$	$\frac{-3}{16} + \frac{3\alpha_f}{8}$	$\frac{1}{32} - \frac{\alpha_f}{16}$	0	0	6
<i>F8</i>	$\frac{93+70\alpha_f}{128}$	$\frac{7+18\alpha_f}{16}$	$\frac{-7+14\alpha_f}{32}$	$\frac{1}{16} - \frac{\alpha_f}{8}$	$\frac{-1}{128} + \frac{\alpha_f}{64}$	0	8
<i>F10</i>	$\frac{193+126\alpha_f}{256}$	$\frac{105+302\alpha_f}{256}$	$\frac{15(-1+2\alpha_f)}{64}$	$\frac{45(1-2\alpha_f)}{512}$	$\frac{5(-1+2\alpha_f)}{256}$	$\frac{1-2\alpha_f}{512}$	10

For multi-dimensional problems, the filter is applied sequentially in each of the three directions. Equation 3.15 is based on templates proposed in Refs. [6] and [49] and with proper choice of coefficients, provides a $2N$ th-order formula on a $2N+1$ point stencil. The $N+1$ coefficients, a_0, a_1, \dots, a_N , are derived in terms of α_f with Taylor- and Fourier-series analyses and are listed in Table 3.1. On uniform meshes, the resulting filters are non-dispersive, do not amplify any waves, preserve constant functions and completely eliminate the odd-even mode. Since α_f is a free parameter, an explicit filter *i.e.*, not requiring the solution of a tridiagonal can be easily extracted by setting $\alpha_f = 0$. In this case, the formulas of Ref. [50] are identically recovered. The primary constraint on α_f is that it must satisfy the inequality $-0.5 < \alpha_f \leq 0.5$. In this range, higher values of α_f correspond to a less dissipative filter, and at $\alpha_f = 0.5$, there is no filtering effect. Detailed spectral responses of these filters may be found in Refs. [1] and [40]. For the results below, the solution is filtered once (in each spatial direction) after the final stage of the explicit *RK4* scheme. The interior filtering formula utilized is denoted by appending its designation to that of the scheme. For example, *C6F10* designates the sixth-order compact scheme combined with the tenth-order filter.

3.2.6 Near-boundary filter formulations

The relatively large stencil of high-order filters requires special formulations at several points near the boundaries. For instance, the 10th-order interior filter requires an 11 point stencil and thus cannot be applied at the “near-boundary” points $1, \dots, 5$ and correspondingly at $IL-4, \dots, IL$ where it protrudes the boundary. The values at points 1 and IL are specified explicitly through the boundary conditions and are not filtered. At the remaining near-boundary points, the approach followed in Ref. [11] was to reduce the stencil-size by applying lower-order centered (*LOC*) formulas. Thus, for example, at points 2 and $IL-1$, a 2nd-order filter is applied, at 3 and $IL-2$, a 4th-order filter is applied and so on. However, as the mesh is coarsened near the boundaries, the error induced by this low-order central or *LOC* technique may eventually become unacceptable and adversely affect the global solution accuracy. In such instances, the lower-order filter at points 2, 3, $IL-2$, $IL-1$ may be optimized by specifying the filter control parameter α_f to be as close as possible to 0.5 as stability allows. This optimized low-order central or *OLOC* approach was shown to be effective for the solution of viscous flows in Ref. [11] and clearly illustrates an advantage of the present implicit filters over standard explicit formulations which lack control of the filter spectral response.

A more general alternative to the *OLOC* approach, is the use of the higher-order one-sided filter formulas developed in Ref. [12]. At a near-boundary point, i , a filter formula is given by

$$\begin{aligned} \alpha_f \hat{\phi}_{i-1} + \hat{\phi}_i + \alpha_f \hat{\phi}_{i+1} &= \sum_{n=1}^{11} a_{n,i} \phi_n \\ i &\in \{2, \dots, 5\} \\ \alpha_f \hat{\phi}_{i-1} + \hat{\phi}_i + \alpha_f \hat{\phi}_{i+1} &= \sum_{n=0}^{10} a_{IL-n,i} \phi_{IL-n}, \\ i &\in \{IL-4, \dots, IL-1\} \end{aligned} \quad (3.16)$$

This choice retains the tridiagonal form of the filter, and α_f remains as the only free parameter.

Table 3.2: Coefficient for 6th-order boundary filter formula at point 3

OA	$a_{1,3}$	$a_{2,3}$	$a_{3,3}$	$a_{4,3}$	$a_{5,3}$	$a_{6,3}$	$a_{7,3}$
6	$-\frac{1}{64} + \frac{\alpha_f}{32}$	$\frac{3}{32} + \frac{13\alpha_f}{16}$	$\frac{49}{64} + \frac{15\alpha_f}{32}$	$\frac{5}{16} + \frac{3\alpha_f}{8}$	$-\frac{15}{64} + \frac{15\alpha_f}{32}$	$\frac{3}{32} - \frac{3\alpha_f}{16}$	$-\frac{1}{64} + \frac{\alpha_f}{32}$

Table 3.3: Coefficients for boundary filter formulas at point 2

OA	$a_{1,2}$	$a_{2,2}$	$a_{3,2}$	$a_{4,2}$	$a_{5,2}$	$a_{6,2}$	$a_{7,2}$
4	$\frac{1}{16} + \frac{7\alpha_f}{8}$	$\frac{3}{4} + \frac{\alpha_f}{2}$	$\frac{3}{8} + \frac{\alpha_f}{4}$	$-\frac{1}{4} + \frac{\alpha_f}{2}$	$\frac{1}{16} - \frac{\alpha_f}{8}$	0	0
6	$\frac{1}{64} + \frac{31\alpha_f}{32}$	$\frac{29}{32} + \frac{3\alpha_f}{16}$	$\frac{15}{64} + \frac{17\alpha_f}{32}$	$-\frac{5}{16} + \frac{5\alpha_f}{8}$	$\frac{15}{64} - \frac{15\alpha_f}{32}$	$-\frac{3}{32} + \frac{3\alpha_f}{16}$	$\frac{1}{64} - \frac{\alpha_f}{32}$

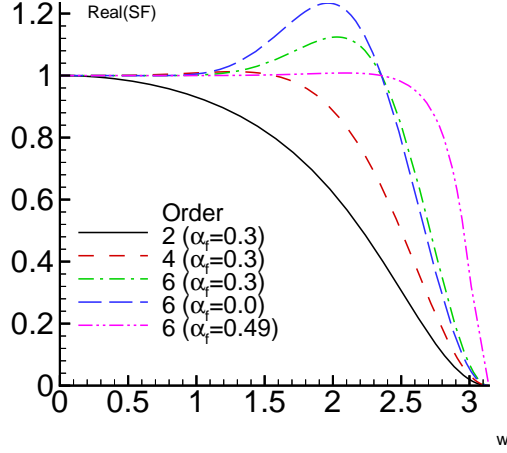


Figure 3.2: Spectral function of some near-boundary filter formulas at point 2

Tables 3.2 and 3.3 list coefficients for the fourth- and sixth-order left-boundary filter formulas employed in the present computations at points 2 and 3. The right-boundary formulas are obtained by noting $a_{IL-n,i} = a_{n+1,IL-i+1}$ for $i \in \{IL-4, \dots, IL-1\}$. An extensive listing of the boundary filter coefficients is provided in Refs. [12, 40]. The real component of the spectral function SF of some boundary formulations at point 2 are plotted in Fig. 3.2. The higher-order approaches are observed to be superior low-pass filters in the range of interest, $w < 1.2$ corresponding to roughly 5 or more points per wave. The 2nd-order filter is symmetric at point 2 and its real part is always less than one, *i.e.*, no wave is amplified. The asymmetric higher-order formulas do not satisfy this desirable $Real(SF) \leq 1$ constraint. The range of amplification increases with order of accuracy (one-sidedness of the formula) and for a given order of accuracy, the implicit ($\alpha_f \neq 0$) filter is seen to be better than the explicit variant ($\alpha_f = 0$) in this respect. The near-boundary filter spectral response may be optimized even further by increasing α_f thereby reducing the undesirable amplification behavior. This is demonstrated in Fig. 3.2 for the 6th-order filter with $\alpha_f = 0.49$. This advantage of the implicit filter will be illustrated in the scattering results presented below.

Chapter 4

COMPUTATIONAL AEROACOUSTICS

4.1 Introduction

The numerical procedures given in the previous chapter have been applied to the simulation of aeroacoustic phenomena. The equation set and boundary conditions are presented here followed by a number of test cases to validate the methodology.

4.2 Governing Equations

To accurately simulate nonlinear aeroacoustic applications, the full (non-linear) Euler equations are selected in general curvilinear coordinates. As mentioned in the previous chapter, the form of the equations may be written as:

$$\frac{\partial}{\partial t} \left(\frac{\vec{U}}{J} \right) + \frac{\partial \hat{F}}{\partial \xi} + \frac{\partial \hat{G}}{\partial \eta} + \frac{\partial \hat{H}}{\partial \zeta} = \frac{\vec{S}}{J} \quad (4.1)$$

Here $\vec{U} = \{\rho, \rho u, \rho v, \rho w, \rho E\}$ denotes the solution vector, J is the transformation Jacobian, and \hat{F}, \hat{G} and \hat{H} are the inviscid fluxes:

$$\hat{F} = \frac{1}{J} \begin{bmatrix} \rho U \\ \rho u U + \xi_x p \\ \rho v U + \xi_y p \\ \rho w U + \xi_z p \\ (\rho E + p) U \end{bmatrix} \quad (4.2)$$

$$\hat{G} = \frac{1}{J} \begin{bmatrix} \rho V \\ \rho u V + \eta_x p \\ \rho v V + \eta_y p \\ \rho w V + \eta_z p \\ (\rho E + p) V \end{bmatrix} \quad (4.3)$$

$$\hat{H} = \frac{1}{J} \begin{bmatrix} \rho W \\ \rho u W + \zeta_x p \\ \rho v W + \zeta_y p \\ \rho w W + \zeta_z p \\ (\rho E + p) W \end{bmatrix} \quad (4.4)$$

where

$$U = \xi_x u + \xi_y v + \xi_z w \quad (4.5)$$

$$V = \eta_x u + \eta_y v + \eta_z w \quad (4.6)$$

$$W = \zeta_x u + \zeta_y v + \zeta_z w \quad (4.7)$$

$$E = \frac{T}{(\gamma - 1)M_\infty^2} + \frac{1}{2}(u^2 + v^2 + w^2). \quad (4.8)$$

In the expressions above, u, v, w are the Cartesian velocity components, ρ the density, p the pressure, and T the temperature. The perfect gas relationship $p = \rho RT$ is also assumed.

The vector source term $\vec{S} = \{0, 0, 0, 0, S_5\}$ is included in order to account for acoustic sources which, for the present results, are prescribed to be of the form:

$$\begin{aligned} S_5(x, y, t) &= e^{-\ln 2 \frac{(x-x_c)^2 + (y-y_c)^2}{b^2}} \sin(\omega t) f(t) \\ f(t) &= \min \left(1.0, \left(\frac{t}{t_o} \right)^3 \right) \end{aligned} \quad (4.9)$$

where x_c and y_c denote the center of the source, ω is the frequency and $f(t)$ is the function used to ramp the onset of the source at the beginning of the computations. The parameters in Equation 4.9, including b and t_o , are specified below in the description of the results.

4.2.1 Boundary Conditions

In the present acoustic simulations, several types of boundaries occur where wall, symmetry or farfield (outflow) conditions need to be specified. At walls, standard inviscid conditions are employed, in which the normal component of velocity is set to zero and the pressure, density and tangential components of velocity are extrapolated. All Neumann-type conditions, including those required to enforce symmetry, are approximated to higher-order accuracy with one-sided third- or fourth-order formulas.

Although several sophisticated treatments are possible for absorbing or non-reflecting farfield conditions [9], the present work employs a simple yet robust technique developed by exploiting the characteristics of the low-pass filter. As discussed in more detail in Section 4.1.3, rapid stretching in regions outside the domain of interest, promotes damping of all perturbations via transfer of energy to reflected odd-even modes which are in turn annihilated by the baseline filter. Although the present approach is empirical in nature, it offers the potential of extension to non-linear and multi-dimensional situations where techniques derived through asymptotic or linear analyses may be ineffective.

4.2.2 Interface treatment in multi-domain calculations

A major issue in multi-domain computations is the accurate treatment of interfaces between domains. In the present work, communication between adjacent meshes is conducted through finite-size overlaps, as depicted in the schematic of Fig. 4.1 for a five-point vertical overlap. At every time-step, the solution is advanced independently in each domain with individual interior and boundary formulas in the same manner as in single-domain computations. Data is exchanged between adjacent domains at the end of each stage of $RK4$, as well as after each application of the filter. Each vertical line is denoted by its i -index. The values at points 1 and 2 of Mesh 2 are set to be identically equal to the corresponding updated values at points $IL - 4$ and $IL - 3$ of Mesh 1. Similarly, reciprocal information is transferred through points 4 and 5 of Mesh 2 which “donate” values to points $IL - 1$ and IL of Mesh 1. This exchange of information is shown with arrows at each point in the schematic. Larger and smaller overlap regions have been examined for fluid dynamic applications in Ref. [12].

4.3 Results

4.3.1 Impact of Filtering on Stretched Meshes

In practical scattering simulations, grid stretching is usually employed in order to reduce required computational resources as well as to permit the use of approximate farfield boundary conditions. Therefore, the performance of high-order schemes on general stretched meshes must be carefully examined for the methodology to be applicable to complex configurations.

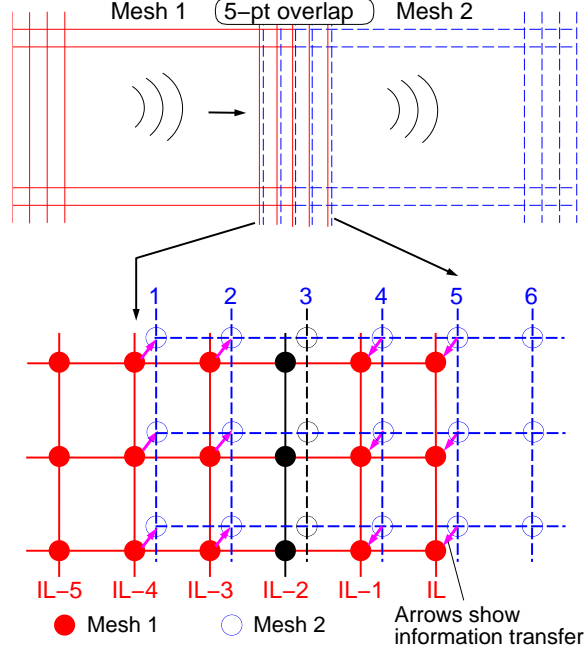


Figure 4.1: Schematic of vertical 5-point mesh overlap for multi-domain applications

One-Dimensional Pulse

An enlightening analysis of the behavior of a smooth solution as it passes through a sudden mesh coarsening has been presented by Vichnevetsky [51] for the 1-D advection equation semi-discretized with the standard second-order *E2* centered scheme. This analysis indicates that although total energy is preserved, at the grid coarsening interface a significant portion of the energy is deposited on a reflected solution composed primarily of odd-even modes and modulated by a smooth envelope. This reflected energy propagates upstream (i.e. with negative group velocity) and in most circumstances if left unchecked it has the potential of ultimately contaminating the genuine solution.

To highlight the effect of grid stretching, we solve the 1-D Euler equations for the propagation of a density disturbance through the sudden grid coarsening shown in Fig. 4.2. The initial conditions are given by

$$\begin{aligned} u &= 1, v = 0, p = p_\infty \\ \rho &= 1 + \epsilon e^{-\ln(2) \frac{x^2}{2}} \end{aligned} \quad (4.1)$$

where $\epsilon = 0.1$. It should be noted that no special one-sided treatments are invoked at the grid interface, but rather the grid jump is handled through the metrics in the general coordinate transformation. Results with the *E2* scheme are shown in Fig. 4.3. The figure indicates that in accordance with Ref. [51], when the pulse crosses the interface, a reflected solution emerges which is characterized by spurious high-frequency modes. Similar behavior was found for the *E4*, *C4* and *C6* schemes (not shown). At a given time instant, the upstream penetration of the reflected solution increased with stencil size and implicitness of the operator.

Since the reflections due to grid stretching are characterized by high-frequency modes, they can be easily removed from the solution by the high-order low-pass filter. This is shown in Fig. 4.4(a) for the *C6F8* scheme, where spurious reflections at the grid-coarsening interface are significantly diminished by the use of the 8th-order filter with $\alpha_f = 0.45$.

These results suggest that the combination of significant grid stretching with a discriminating low-pass filter may be used as an alternative procedure for outflow boundary treatment. This approach is investigated further in Section 4.1.3.

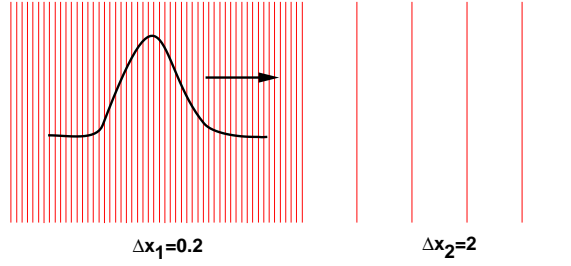


Figure 4.2: Mesh with abrupt change in spacing

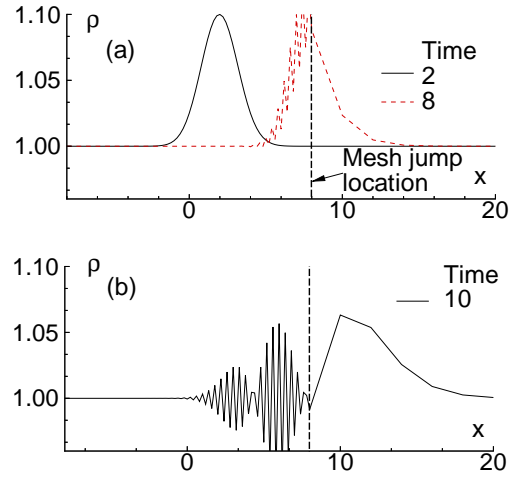


Figure 4.3: Propagation of 1-D pulse through sudden mesh coarsening with *E2* scheme and without filter.

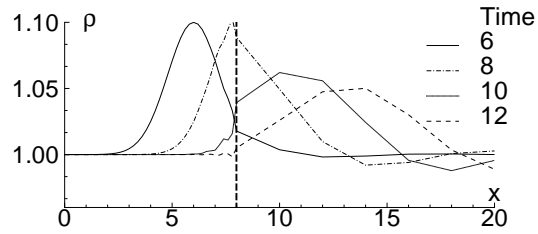


Figure 4.4: Propagation of 1-D pulse through sudden mesh coarsening with *C6F8* scheme.

Two-Dimensional Pulse

Next, we consider the propagation of a 2-D pressure pulse in the presence of grid stretching. The mesh, shown in Fig. 4.5(a), contains a section of uniform spacing ($\Delta x = \Delta y = 0.05$) which extends over the region $-3 \leq \{x, y\} \leq 3$. Beyond this zone, the mesh is stretched with an exponential function and maximum stretching factor of 1.13. For the purpose of comparison, a large uniform grid was also considered. The solutions were initialized at $t = 0$ by prescribing a pressure disturbance of the form

$$p = p_\infty + \epsilon e^{-\ln 2 \frac{(x-x_c)^2 + (y-y_c)^2}{b^2}} \quad (4.2)$$

where $\epsilon = 0.1$, $b = 0.2$ and $x_c = y_c = 0$. The propagation of this pressure pulse was computed with the *C6* scheme and $\Delta t = 0.005$ until $t = 4.5$. By this time, the pressure disturbance had moved into the stretched mesh region but was still sufficiently far from the computational farfield boundaries in order to diminish effects of boundary conditions. The pressure contours are displayed in Fig. 4.5(b) and (c) for both the unfiltered and filtered (*F10*, $\alpha_f = 0.49$) solutions. The results obtained without a filter show the appearance of high-frequency modes which are generated as the pulse moves into the stretched mesh region. As in the previous 1-D case, this spurious reflected energy propagates in a direction opposite to the travel of the physical disturbance, towards the center of the domain. When the high-order filter is employed, these unwanted reflections are completely eliminated, as seen in Fig. 4.5(c). The corresponding computed pressure along the center of the pulse ($y = 0$) is given in Fig. 4.6. In the region of interest, $-3 \leq x \leq 3$, the filtered results for the stretched grid are essentially identical to those obtained without a filter on a large domain with constant spacing ($\Delta x = \Delta y = 0.05$). By contrast, the unfiltered solution on the stretched grid clearly displays the existence of packets of reflected energy composed mostly of odd-even modes. These 2-D results clearly demonstrate the effectiveness of the high-order low-pass filter in controlling spurious reflections without degrading the fidelity of the solution in the region of interest. In the absence of a high-frequency cutoff mechanism (designed to completely annihilate odd-even modes), a large number of grid points would be required [15] if a constant mesh spacing had to be carried all the way to the far field boundaries.

Use of Mesh Stretching and Filtering as an Alternative Outflow Boundary Treatment

As shown earlier in Section 4.1.1, by employing a large rate of stretching, a significant amount of energy can be reflected at the grid coarsening interface. Provided this *reflected* energy is deposited into high-frequency modes (in the fine mesh region), it can then be subsequently eliminated by the baseline high-order low-pass filter without contaminating the genuine solution. Furthermore, since the mesh is stretched rapidly in the buffer zone, the *transmitted* energy is also quickly dissipated by the high-order filter (as the transmitted solution features are represented by a diminishing number of points per wave). This proposed method eliminates the need for more sophisticated (and perhaps more restrictive) boundary conditions at the expense of extending the computational domain. Although the proposed approach has a mathematical foundation (at least based on the 1-D analysis of Ref. [51]), its implementation is highly empirical, and therefore its utility must be evaluated in the context of practical applications.

As a severe test case, consider the propagation of acoustic waves in the grid of Fig. 4.7(a). This mesh is uniform ($\Delta x = \Delta y = 0.05$) in the center of the computational domain ($-3 \leq x, y \leq 3$). Outside of this resolved region, Δx and Δy are increased abruptly by a factor of 10. Both the case of an acoustic source and a transient pulse were computed with *C6F8* ($\alpha_f = 0.45$) in order to examine the robustness of the numerical approach. The source was specified by Equation 4.9 with $x_c = y_c = 0$, $\omega = 5\pi$, $b = 0.2$ and $t_o = 4$. A snapshot of the pressure is displayed in Fig. 4.7(b). It is apparent that the acoustic energy reflected at the grid-coarsening interface is almost completely annihilated by the high-order filter. The corresponding plot of the instantaneous pressure along the diagonal ($x = y$) is shown in Fig. 4.7(c) and indicates that the transmitted energy diffuses rapidly in the coarse mesh region. For this square grid, the circular waves cross the grid interface at a varying angle of incidence without apparent anisotropies being introduced.

For a more quantitative test, the case of a transient pulse given by Equation 4.2 (with $\epsilon = 0.02$, $b = 0.2$) was also considered. Figure 4.8(a) shows the history of non-dimensional pressure at the point $x = 2$, $y = 2$. The solution for the suddenly stretched mesh is observed to be in excellent agreement with results obtained on a large domain with uniform mesh spacing, as demonstrated by the small difference between the two solutions (Fig. 4.8(b)).

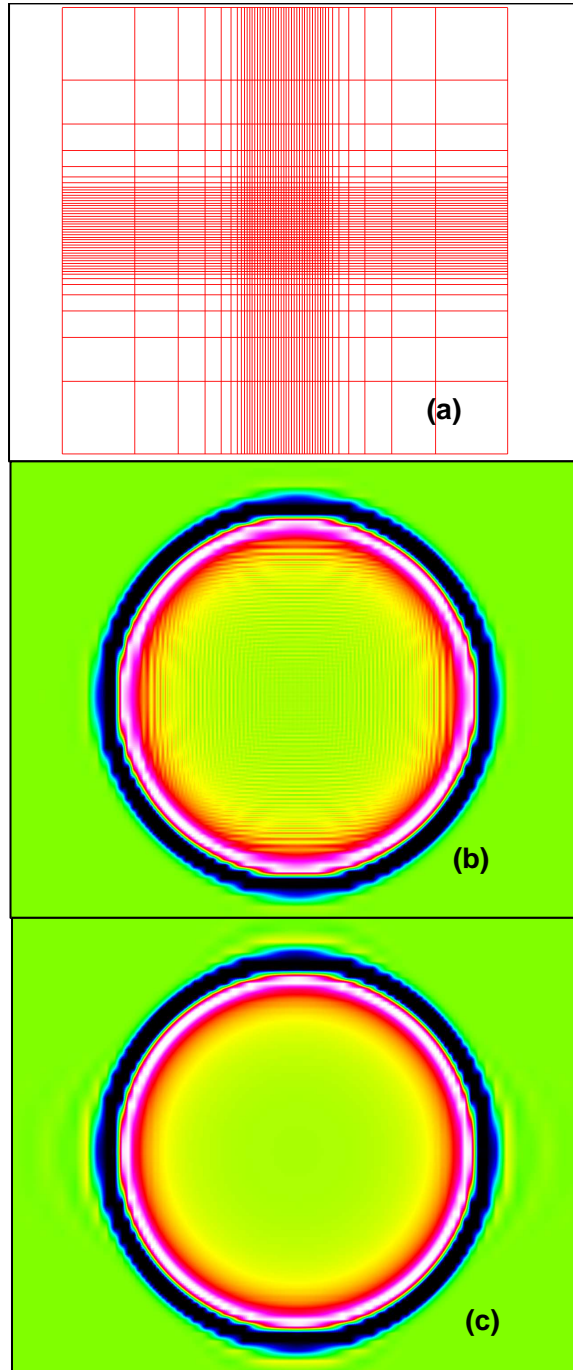


Figure 4.5: Propagation of 2-D pressure pulse on smoothly-stretched Cartesian mesh: (a) grid, (b) unfiltered $C6$ and (c) filtered $C6F10$ results

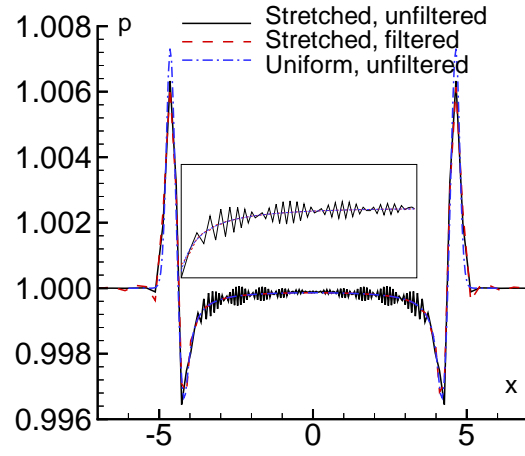


Figure 4.6: Effect of high-order filter on computed pressure along $y = 0$ at $t = 4.5$ for the 2-D acoustic pulse propagation of Fig. 4.5.

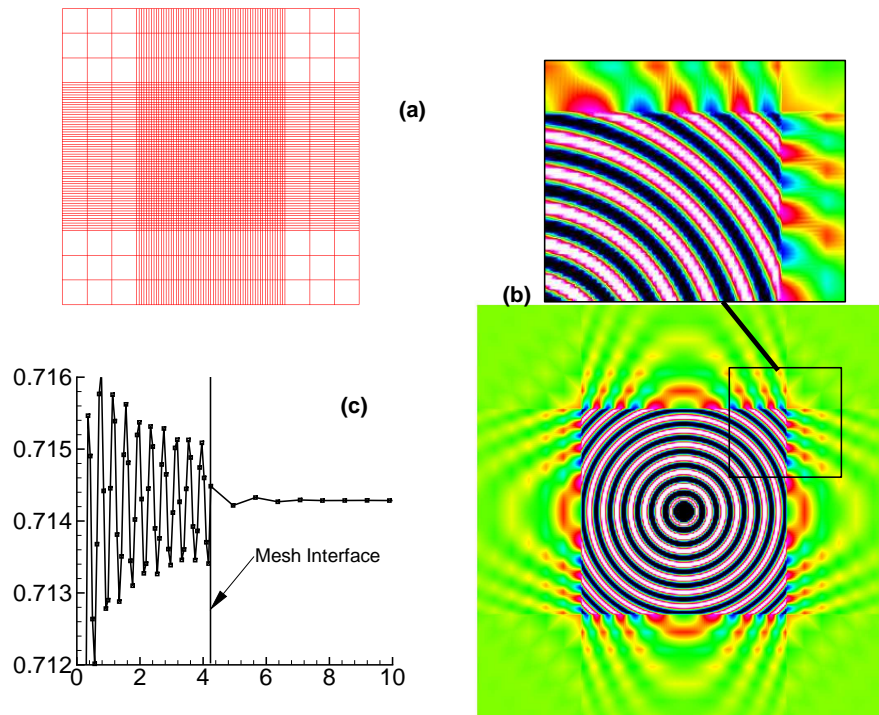


Figure 4.7: Computation of 2-D acoustic source on mesh with abrupt stretching. (a) Grid (b) Pressure contours (c) Pressure along diagonal

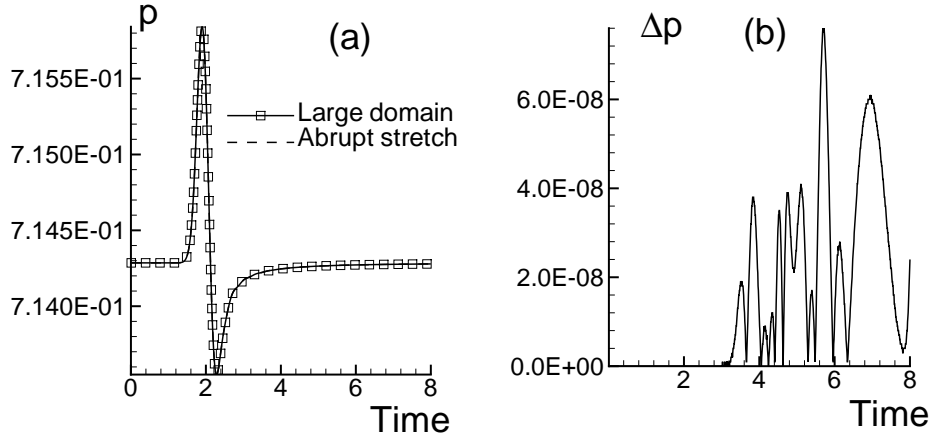


Figure 4.8: Pressure at $x = 2, y = 2$ for 2-D pulse propagation on mesh with abrupt stretching. a) Pressure history, b) discrepancy between stretched and uniform grid solutions

Grid	Dimensions	$\frac{\Delta r_{max}}{D}$	$\Delta\theta_{min}$	$\Delta\theta_{max}$
<i>G1</i>	156×175	0.04	0.5	1.25
<i>G2</i>	252×175	0.04	0.5	0.75

Table 4.1: Grid parameters for pulse scattering problem in region of interest ($r/D \leq 7$)

The effectiveness of the proposed outflow treatment was also evaluated for the convecting vortex case previously considered in Ref. [11]. The computational domain of interest ($-6 \leq x, y \leq 6$) is discretized using a uniform mesh spacing ($\Delta x = \Delta y = 0.2$), as shown in Fig. 4.9a. Outside of this region, the grid is expanded employing a constant stretching factor of 1.7. The vortex is convected along the diagonal of the mesh in order to provide a more general test of the outflow approach. Contours of the perturbation velocity magnitude at various instants are shown in Fig. 4.9b-d. The vortical disturbance is observed to pass without significant distortion through the corner of the grid-coarsening interface. A comparison of the computed and exact perturbation velocity magnitudes along the diagonal $x = y$ is displayed in Fig. 4.10 at $t = 2$ and 8. The excellent agreement between the computed and exact solution is clearly retained as the vortex crosses the interface.

4.3.2 Scattering of Acoustic Pulse From Cylinder

In order to validate the present approach for curvilinear geometries, we select as a test case the benchmark problem denoted as Category I, Problem 2 in the 2nd CAA Workshop of Ref. [52]. This configuration (Fig. 4.11) describes the scattering off a circular cylinder of a prescribed initial pressure pulse. The pulse is given by Equation 4.2 with $x_c = 4, y_c = 0, \epsilon = 0.01, b = 0.2$.

Along the cylinder surface, the simple wall boundary conditions noted in Section 3.6 are employed. Since the configuration is symmetric, only the upper half of the domain is considered, and symmetry conditions are invoked along $\theta = 0^\circ, 180^\circ$. As indicated in Fig. 4.11, the grid is stretched for $r/D > 7$ using a constant stretching factor of 1.1. Since in this coarse-mesh region the outgoing pulse is dissipated by the baseline filter, a simple extrapolation condition is suitable along the farfield boundary. Two levels of spatial resolution were used, and details of the computational grids are provided in Table 4.1. All cases were advanced in time with a non-dimensional Δt of 0.004.

Pressure contours depicting pulse propagation and reflection off the cylinder surface are shown in Fig. 4.11 at several instants in time for the *C6F10* scheme on the finest mesh (*G2*). The history of pressure at selected points and for several computations is presented in Figs. 4.12 through 4.14. The points denoted as ‘A’ and

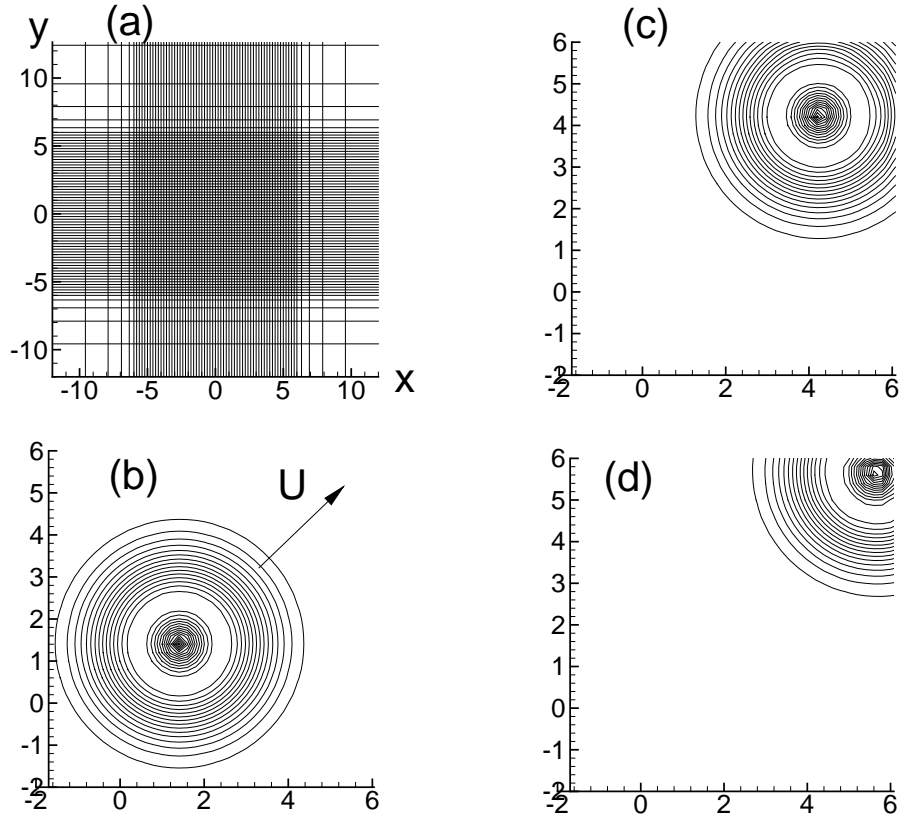


Figure 4.9: Propagation of a vortical disturbance at 45° to the horizontal. a) Grid. Contours of perturbation velocity magnitude at b) $t=2$, c) $t=6$ and d) $t=8$

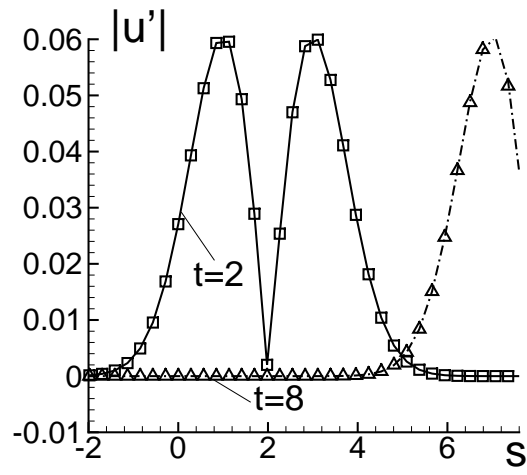


Figure 4.10: Perturbation velocity magnitude along diagonal for convecting vortical disturbance. Symbols and lines denote computed and exact solutions respectively

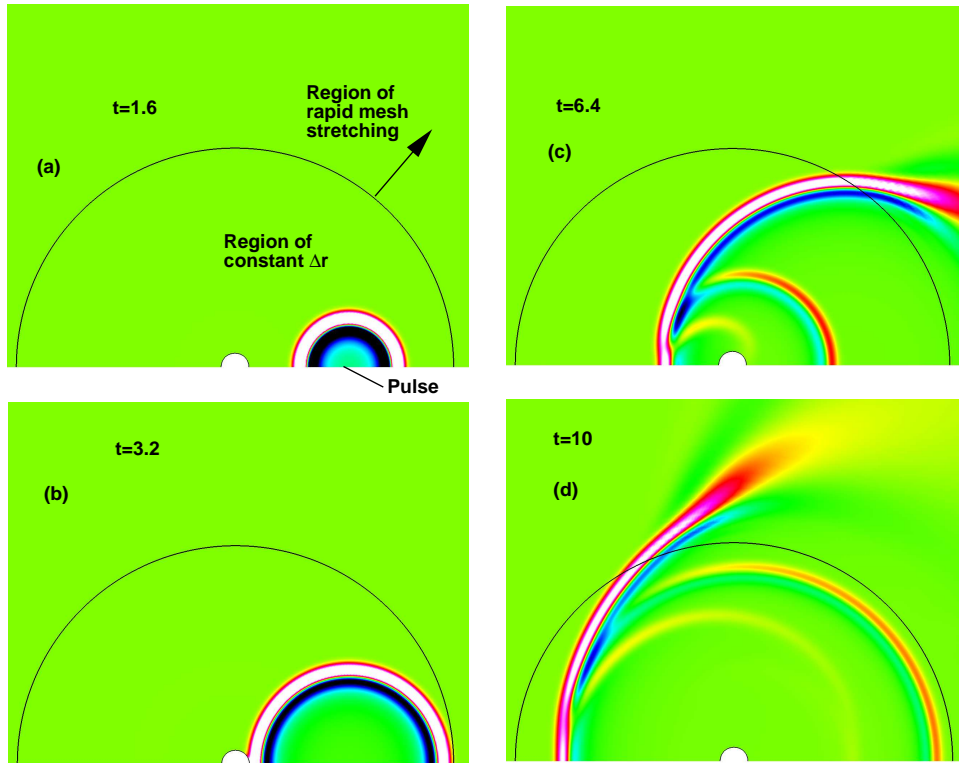


Figure 4.11: Pressure contours at various instants for acoustic pulse scattered by a circular cylinder

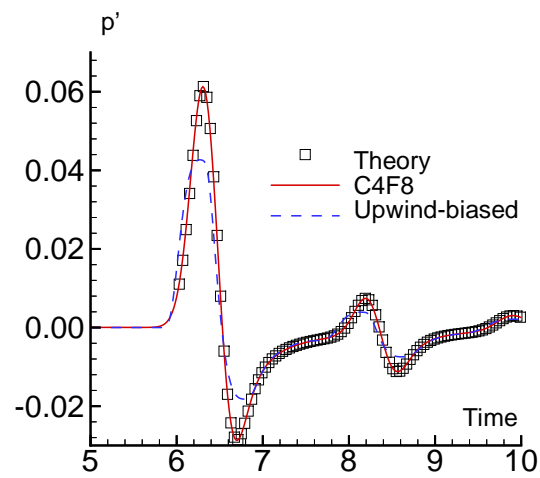


Figure 4.12: History of pressure at point 'A' on Grid $G2$ for scattered pulse

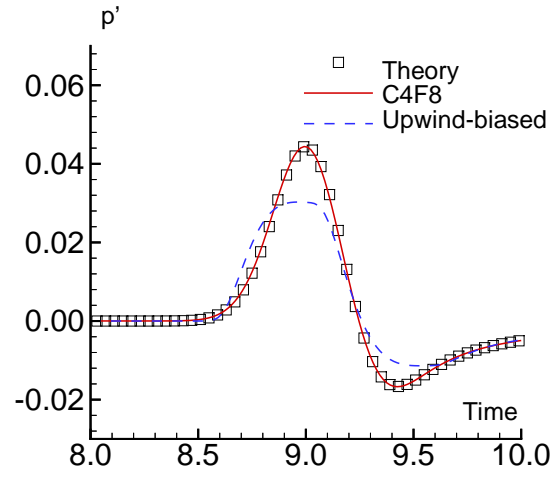


Figure 4.13: History of pressure at point 'C' on Grid $G2$ for scattered pulse

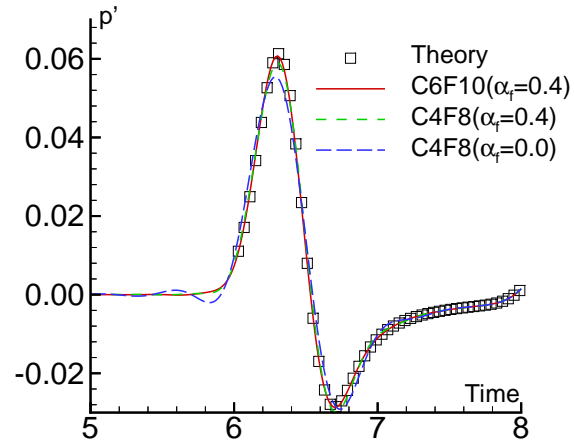


Figure 4.14: History of pressure at point 'A' on Grid $G1$ for scattered pulse

Grid	Dimensions	$\frac{\lambda}{\Delta r_{max}}$	$\frac{\lambda}{(r\Delta\theta_{max})}$	$\Delta\theta_{max}$
$G1$	252×175	6.25	3.82	0.75
$G2$	361×321	8.00	5.73	0.50
$G3$	481×491	12.5	7.64	0.375

Table 4.2: Grid parameters for source scattering problem, λ = spatial wavelength

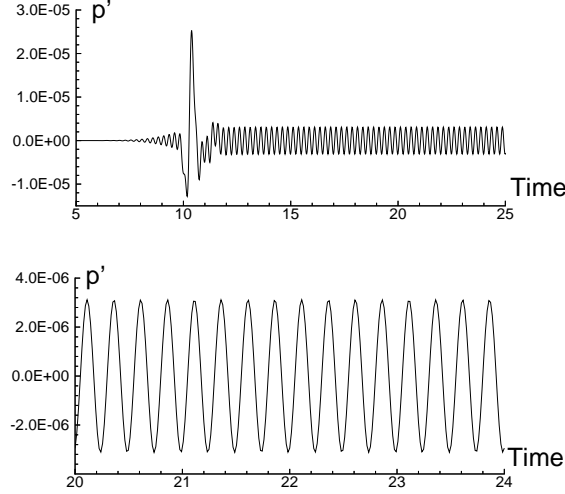


Figure 4.15: Pressure history at a point for periodic acoustic source problem

‘C’ are located at $(r/D = 5, \theta = 90^\circ)$ and $(r/D = 5, \theta = 180^\circ)$ respectively. Results on Grid $G2$ with $C4F8$ ($\alpha_f = 0.4$) are observed to be in excellent agreement with the exact solution [52]. This is also the case for the $C6F10$ algorithm (not shown). For the purpose of comparison, computations were also performed with a standard third-order accurate upwind-biased scheme. As Figs. 4.12 and 4.13 indicate, the upwind results exhibit excessive dissipation even on this finer mesh. On the coarser mesh $G1$, (Fig. 4.14), the $C6F10$ and $C4F8$ with implicit filter ($\alpha_f = 0.4$) are also observed to be in good agreement with the exact solution. However, on this mesh, the $C4$ scheme combined with an 8th-order *explicit* filter (i.e. $\alpha_f = 0.0$) displays appreciable error. This highlights the improved accuracy of the implicit filter formulation.

4.3.3 Scattering of Periodic Acoustic Source

This case which corresponds to Category I, Problem 1 in Ref. [52], considers the scattering from a circular cylinder of a periodic acoustic source. An acoustic source with finite spatial support is given by Equation 4.9 with $x_c = 4$, $y_c = 0$, $\omega = 8\pi$, $b = 0.2$, $t_0 = 4$. This case constitutes a more stringent test of the algorithm and boundary conditions since an asymptotic periodic solution must be attained, and long-term numerical stability demonstrated. The boundary conditions were of the same type as those noted in the previous section. Three computational grids were employed and their details are summarized in Table 4.2. For all grids, the radial spacing is stretched over the range $10 \leq r/D \leq 20$ using a constant stretching factor of approximately 1.2. A time step $\Delta t = 0.004$ was specified for all cases, and the solutions were typically run for approximately 20 – 30 characteristic times to guarantee a periodic state and to ensure long term numerical stability.

A sample convergence history of the pressure at $r = 3, \theta = 135^\circ$ is shown in Fig. 4.15. After the initial transient generated by the source onset leaves the domain, a periodic solution is clearly obtained. This suggests that acoustic energy is not trapped by the grid stretching or the approximate outflow boundary treatment. A representative instantaneous interference pattern generated by the incident and scattered waves is shown in Fig. 4.16. It is observed that in the far field, the rapid mesh stretching combined with

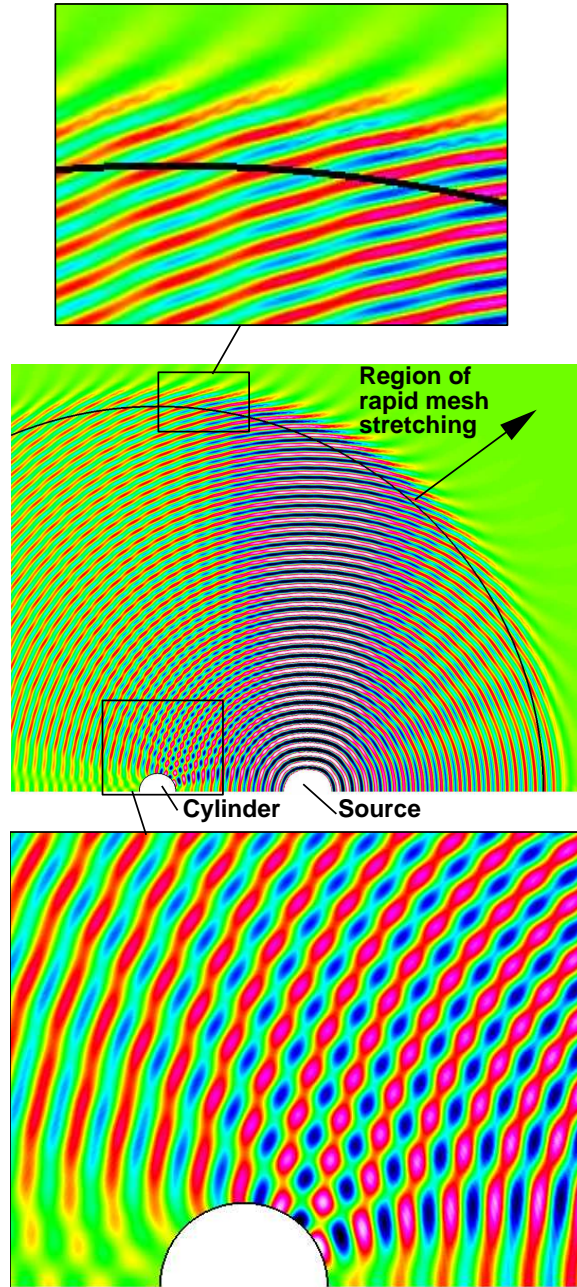


Figure 4.16: Interference pattern due to scattering by a cylinder of periodic acoustic source

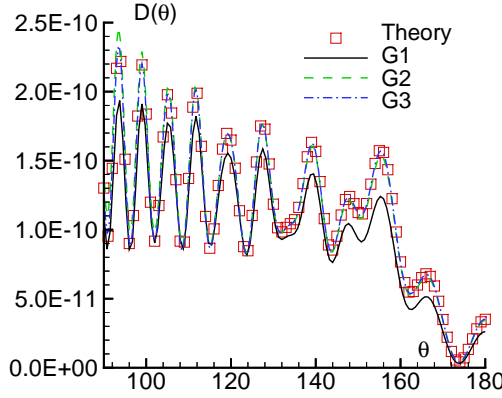


Figure 4.17: Computed directivity of radiated sound at $r/D = 5$ with *C6F10*

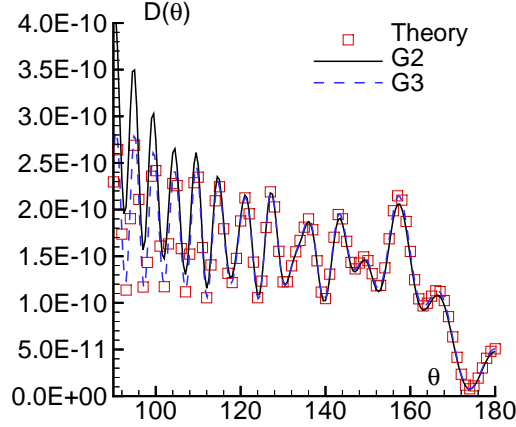


Figure 4.18: Computed directivity of radiated sound at $r/D = 10$ with *C6F10*

the high-order filter provide an effective mechanism to absorb the outgoing acoustic radiation with minimal reflection. Figures. 4.17 and 4.18 display the computed directivity of the radiated sound $D(\theta) = r \langle p'^2 \rangle$ at $r/D = 5$ and $r/D = 10$ respectively. The directivity computed with *C6F10* on the finest mesh (Grid *G3*) is in excellent agreement with the exact solution at both radial locations considered. The results on the medium mesh (Grid *G2*) are reasonable at $r/D = 5$ but begin to exhibit errors at $r/D = 10$, particularly for $\theta < 100^\circ$. On the coarsest mesh (Grid *G1*), the computed $D(\theta)$ shows already significant departure at $r/D = 5$. It should be noted that the radial spacing in Grids *G1*, *G2* and *G3* (see Table 4.2) correspond to only 6.25, 8 and 12.5 points per wave (*PPW*) respectively. However, in terms of the azimuthal spacing, at $r/D = 5$ the corresponding densities are only approximately 4, 6 and 8 *PPW*. It then appears that in order to maintain an accurate solution the minimum spatial resolution requirement lies in the range of 4 to 6 *PPW*. For subsequent comparisons, and in order to limit use of computational resources, we focus on Grid *G2* and on the directivity at $r/D = 5$ where the *C6F10* method provides good results.

A comparison of various schemes is presented in Fig. 4.19 in terms of the computed directivity. Limited degradation in accuracy is encountered when going from the baseline *C6F10* to the *C4F8* scheme. By contrast, the explicit fourth-order method combined with an explicit eighth-order filter (*E4F8*) provides rather poor results for the sound pressure level at this location. Therefore, a significant improvement is achieved when

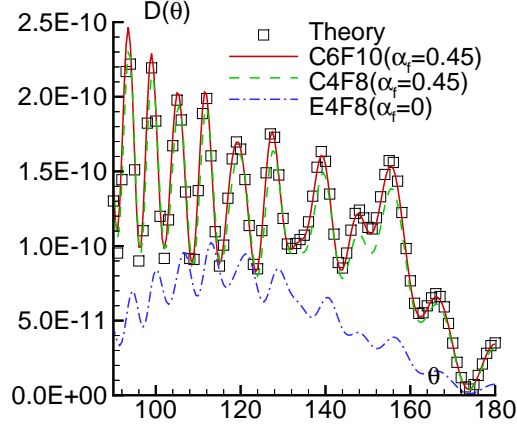


Figure 4.19: Effect of scheme on computed directivity at $r/D = 5$

proceeding from the explicit to the implicit (compact) spatial discretization and filtering techniques while simultaneously reducing the scheme stencil size.

The effect of the filter formulation near the scatterer on the solution accuracy for the *C6F10* procedure is examined next. Figure 4.20 shows the computed sound directivity at $r/D = 5$ for three different boundary filter approaches. The high-order boundary filter strategy (denoted as HO) with filter orders ‘6,6,6,8’ at points ‘2,3,4,5’ respectively is in good agreement with the exact solution. With this technique, the filter control parameter $\alpha_f = 0.45$ remains unchanged throughout the domain. For the low-order-centered method (LOC), $\alpha_f = 0.45$ is again fixed, but the filter order is degraded to ‘2,4,6,8’ at points ‘2,3,4,5’. For the relatively coarse mesh employed (Grid *G2*), the LOC boundary method incurs significant errors (Fig. 4.20). This situation is exacerbated since the source center lies on one of the boundaries and part of the acoustic energy is dissipated before propagation. The problem with the LOC approach is overcome through optimization of the filter coefficient near the boundary. As Fig. 4.20 indicates, the higher-order results are essentially recovered by the optimized LOC (or OLOC) method when α_f is set to 0.49 for the second- and fourth-order filter operators (points ‘2’ and ‘3’). These results reiterate the superior performance of compact-based filters over standard explicit filters since the latter contain no mechanism for control of the spectral response. This issue is of considerable importance not only for accuracy as already shown, but also for robustness (stability) of the overall high-order approach. As noted in reference to Fig. 3.2, the spectral response of the high-order boundary filters exhibit, due to the lack of symmetry, undesirable amplification over a small portion of the modified wave number range. For a fixed order of accuracy, this behavior is more pronounced for the standard explicit filters, but can be lessened for the compact filter through an increase in α_f . A practical example where this control is beneficial is illustrated in Fig. 4.21 for the scattering cylinder configuration, in which results with the *C6F10* scheme and with a minimum 6th-order boundary filter are shown near the cylinder surface. The computation in Fig. 4.21(a) employed $\alpha_f = 0.45$ and provided a stable solution. However, when an explicit filter is used (i.e. $\alpha_f = 0$), spurious oscillations appear near the surface and ultimately cause numerical instability. By increasing α_f to 0.45 at the near-boundary points only, these unwanted oscillations were avoided. This suggests that the observed difficulties are due to the asymmetric near-boundary high-order explicit filter.

4.3.4 Scattering Multi-Domain Application

In order to demonstrate the capability of the present numerical approach to handle multiple-domain applications, the previous scattering case was simulated using the two-zone overlap configuration shown schematically in Fig. 4.22. The original single grid (*G2*, Table 4.2) was split along $\theta = 90^\circ$, and extra ξ -lines were added to form a five-point overlap (see Fig. 4.1). The solutions were advanced separately on each domain,

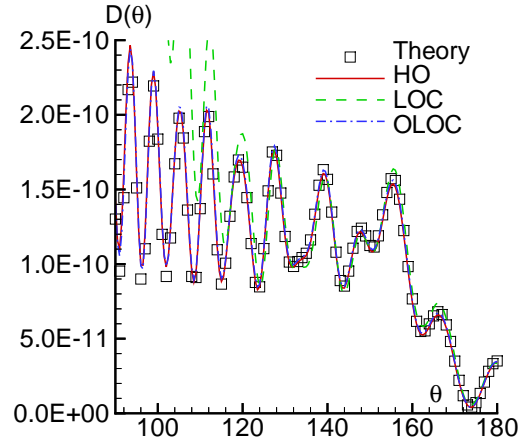


Figure 4.20: Effect of filter boundary treatment on directivity at $r/D = 5$. HO=Higher order boundary formulas, LOC=Lower-order centered, OLOC=Optimized lower-order centered

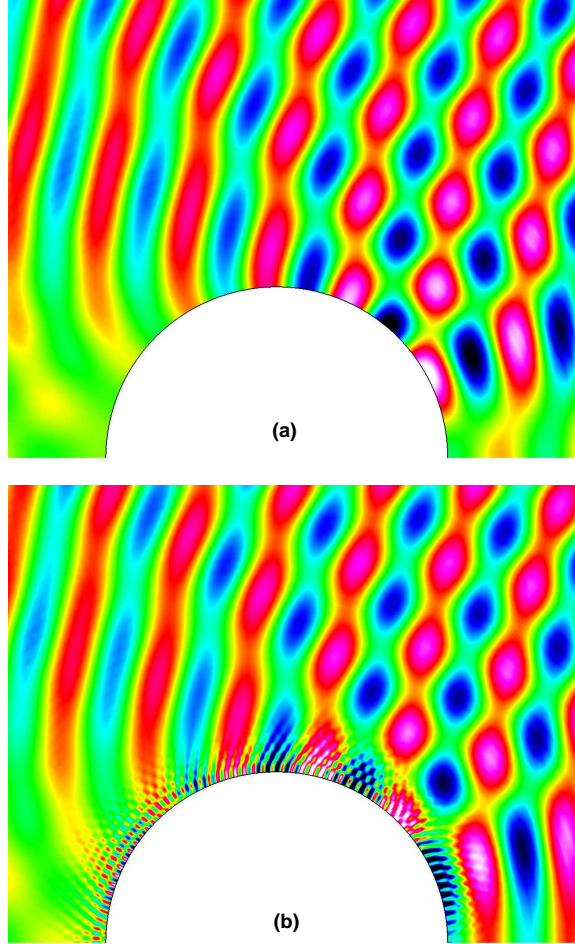


Figure 4.21: Comparison of (a) implicit and (b) explicit near-boundary high-order filters

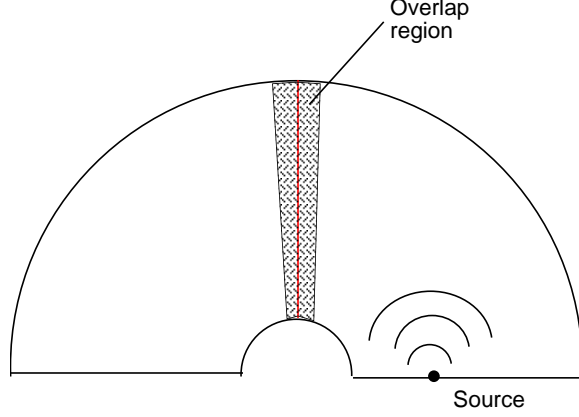


Figure 4.22: Schematic of mesh overlap for multi-domain cylinder scattering problem

and information was exchanged at the overlap points in the manner previously discussed in Section 3.7. Solutions were obtained using the sixth-order compact scheme for interior points along with fourth- and fifth-order compact operators at the boundary and next-to-boundary points respectively. In the interior of each domain, a 10th-order filter was employed. Near the boundary, two different choices were made, the first with a minimum sixth-order and the second with a minimum eighth-order formula. For all filter operators, the coefficient $\alpha_f = 0.45$ was specified.

Figure 4.23 displays instantaneous pressure contours in the vicinity of the vertical overlap. It is apparent that the pressure waves cross the grid interface without producing any noticeable disruptions of the interference pattern. It should be noted that pressure waves generated by the source propagate through the overlap region in an oblique direction to the zonal interface. A quantitative comparison between the single- and multiple-domain solutions is given in Fig. 4.24 in terms of the directivity of the radiated sound at $r/D = 5$. The directivity obtained with either 6th- or 8th-order near-boundary filter formulas in the overlap region is essentially the same as the corresponding single-domain baseline solution. These results highlight the potential of the present high-order methodology for domain-decomposition applications on parallel computers.

4.3.5 Spherical Pulse on a 3-D Curvilinear Mesh

The final validation case considers the propagation of a 3-D spherical pulse [53] in a curvilinear mesh. An initial pressure pulse is prescribed by

$$p = p_\infty + \epsilon e^{-\ln 2 \frac{(x^2 + y^2 + z^2)}{9}} \quad (4.3)$$

where $\epsilon = 0.01$. In order to examine metric cancellation errors, a three-dimensinal curvilinear mesh is generated using the following equations:

$$\begin{aligned} x_{i,j,k} &= x_{min} + \Delta x_o \left[(i-1) + \frac{A_x \sin \frac{n_{xy} \pi (j-1) \Delta y_o}{L_y} \sin \frac{n_{xz} \pi (k-1) \Delta z_o}{L_z}}{L_x} \right] \\ y_{i,j,k} &= y_{min} + \Delta y_o \left[(j-1) + \frac{A_y \sin \frac{n_{yx} \pi (i-1) \Delta x_o}{L_x} \sin \frac{n_{yz} \pi (k-1) \Delta z_o}{L_z}}{L_y} \right] \\ z_{i,j,k} &= z_{min} + \Delta z_o \left[(k-1) + \frac{A_z \sin \frac{n_{zx} \pi (i-1) \Delta x_o}{L_x} \sin \frac{n_{zy} \pi (j-1) \Delta y_o}{L_y}}{L_z} \right] \end{aligned} \quad (4.4)$$

$$i = 1 \dots IL; j = 1 \dots JL; k = 1 \dots KL$$

$$\Delta x_o = \frac{L_x}{IL-1}; \Delta y_o = \frac{L_y}{JL-1}; \Delta z_o = \frac{L_z}{KL-1}$$

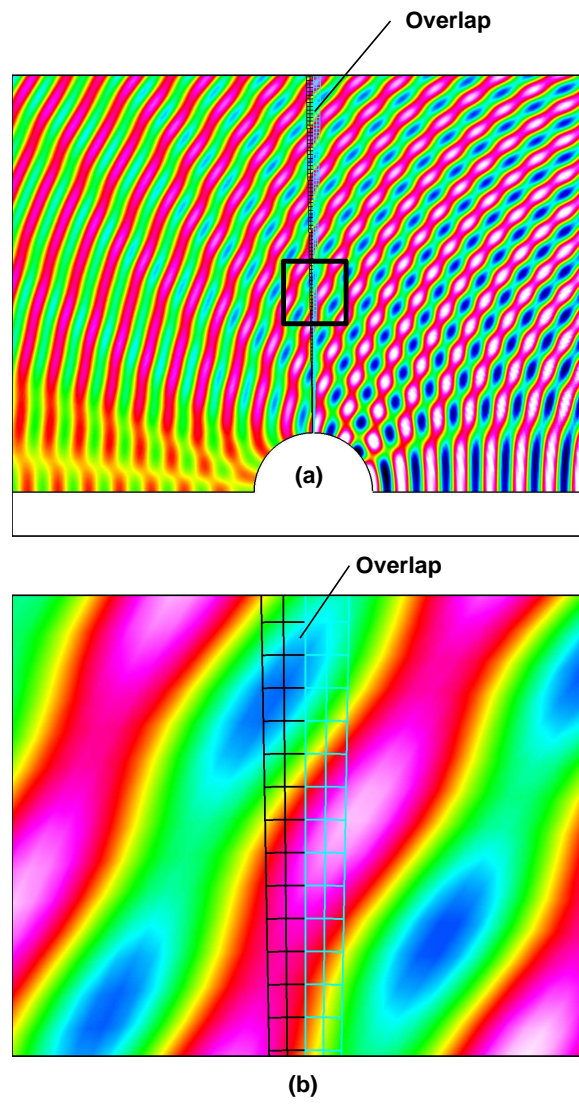


Figure 4.23: Pressure contours for multi-domain scattering simulation in vicinity of mesh overlap region

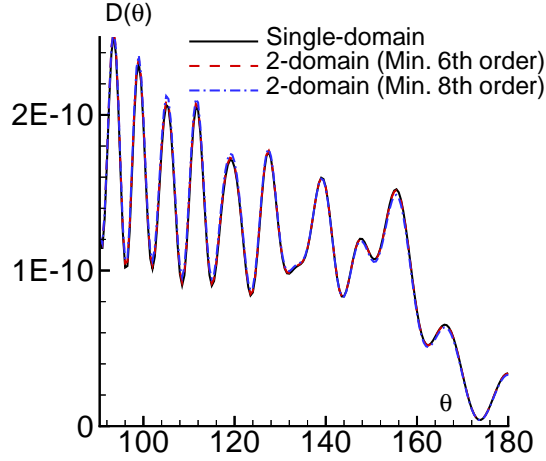


Figure 4.24: Comparison of directivity at $r/D = 5$ for multi-domain and single-domain calculations

with the specified parameters $IL = JL = KL = 61$, $A_x = A_y = A_z = 1$, $L_x = L_y = L_z = 60$ and $n_{xy} = n_{yz} = \dots = 8$. These parameters yield a mesh in which the metric identities (e.g. Eqn. 3.4) are not trivially satisfied. A constant ζ plane of the mesh at the location of maximum deformation is shown in Fig. 4.25(a). The imposed grid undulations are resolved with approximately 15 *PPW*.

The pulse propagation problem is computed with a $\Delta t = 0.004$ using the *C4F10* algorithm with $\alpha_f = 0.49$. Figure 4.25(b) displays the calculated pressure contours on a plane through the center of the spherical pulse at $t = 10$ for the case when the metrics are evaluated in the standard fashion of Equation 3.3. It is apparent that significant distortion of the wave front occurs due to the lack of freestream preservation (i.e. metric cancellation errors). The perturbation pressure along the grid line $i = j = 31$, (Fig. 4.26) indicates unacceptable departure from the theoretical solution. The results obtained with the new metric evaluation procedure of Equation 3.5 exhibit no distortions of the spherical front (Fig. 4.25(c)) and are in excellent agreement with the exact solution (Fig. 4.26).

Calculations with *C6F10* (not shown) displayed reduced sensitivity to the choice of metric evaluation procedure. This is in agreement with the results of Ref. [12], where metric cancellation errors were shown to decrease with increasing order of accuracy. Nonetheless, without the incorporation of Equation 3.5 in the calculation of the metric relations, all solutions on this highly distorted mesh were found to be of poor quality. Even for relatively benign 3-D curvilinear grids, freestream preservation errors may swamp acoustic pressure levels unless proper metric evaluation procedures are employed. It should be noted that analytic metric evaluation (even if available) does not remedy the situation [11, 1]. The present results clearly demonstrate that the superior performance of the high-order method can be extended to the realm of general curvilinear grids making the approach suitable for complex configurations including moving/deforming meshes for which good grid quality cannot usually be maintained.

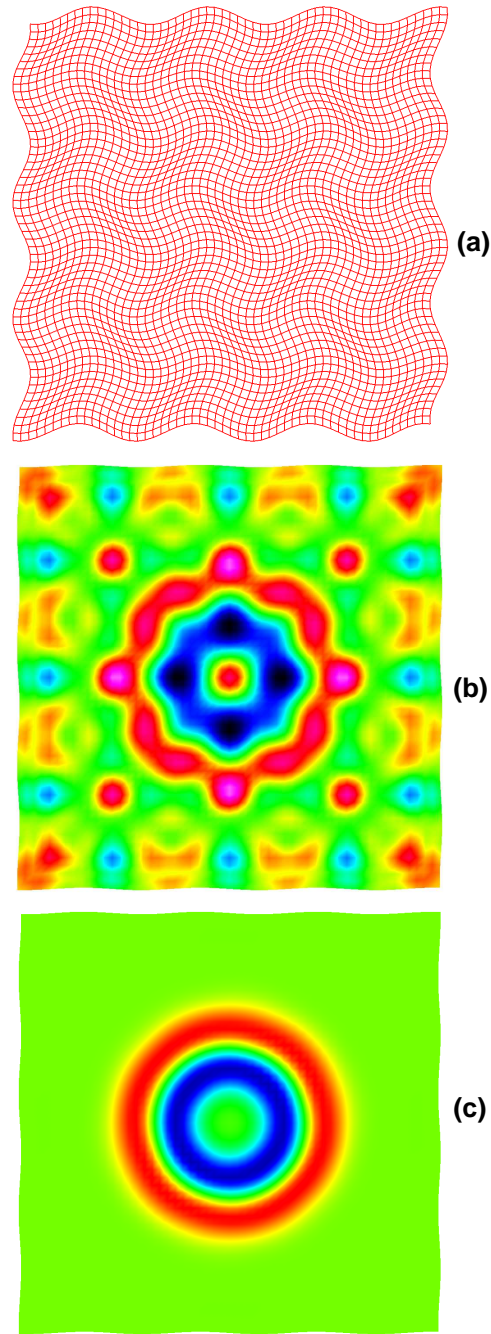


Figure 4.25: Three-dimensional spherical pulse. (a) Mesh, (b) and (c) Pressure contours with standard and new metrics respectively

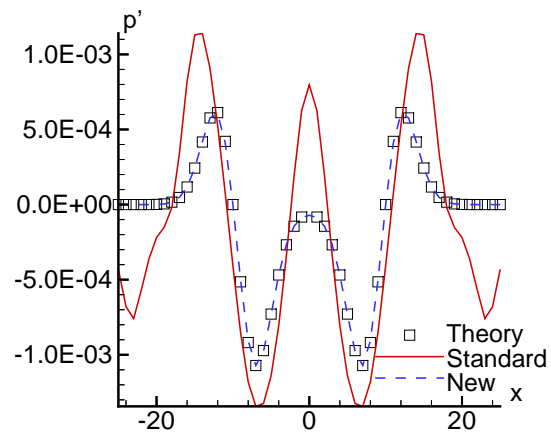


Figure 4.26: Effect of metric evaluation on computed pressure along line through spherical pulse at $t = 10$.

Chapter 5

PREPROCESSING TOOLS FOR HIGH-ORDER OVERSET-GRIDS

5.1 Introduction

A new family of preprocessing tools have been developed for use with the high-order overset-grid (HO-OG) algorithm. Some of these tools are general in nature and have been implemented to improve the flexibility of the algorithm as currently implemented, while others are specifically needed due to the requirements of the high-order method. The function of these tools is to quickly, accurately and robustly take overset-grid systems and develop the necessary input for use with the high-order, parallel research code *FDL3DI* [40]. The approach utilized here is conceptually similar to that employed by the *BREAKUP* code [54], which some important modifications to address unique features of the high-order algorithm. Section 5.2 addresses the specific preprocessing elements that have been developed. Section 5.3 details the flow solver and specific modifications that have been made to it to accept the input from the preprocessing stage as well as to improve its overall flexibility. Finally, two examples of the use of the HO-OG algorithm, completed with the newly developed preprocessing tools, are presented in Section 5.4. These include a two-dimensional aeroacoustic application involving scattering from three circular cylinders and a three-dimensional electromagnetics problem involving scattering from a single sphere.

5.2 Preprocessing Elements

The approach used here for performing HO-OG simulations is shown in the flowchart in Figure 5.1. This section will focus on the preprocessing requirements, while the following section will address issues associated with the flow solver itself. Postprocessing will not be specifically addressed in this work.

For the purposes of the discussion here, it is assumed that an appropriate overset-grid system [55] has been previously generated for the geometry of interest. To perform a computational simulation using the overset-grid method, the connectivity between overlapping grids must first be established. There are a variety of ways to do this [55], but here this task is performed using the *PEGASUS* Version 5 software package. [56] In addition to the grids themselves and the input necessary to guide the operation of the code, *PEGASUS* requires specification of the boundary conditions that will be enforced in the solution domain by the flow solver. Typically, it is assumed that any grid boundaries that do not have boundary conditions specified by the input data will require interpolation. The task of determining the appropriate connectivity between donor and receiver grids at these non-specified boundaries is handled by *PEGASUS*.

Upon execution of *PEGASUS*, a file is generated that contains the connectivity data for the overset grid-level topology. This data is contained in the “XINTOUT” file and includes all receiver points and their corresponding donor points and offsets (the distance between the base point of the donor stencil and receiver point in the computational space of the donor grid). The interpolation offsets are calculated using an inverse isoparametric mapping that is spatially second-order accurate [57]. The donor point is actually the base point identifying the computational cell containing the receiver point. The eight points of the donor cell containing

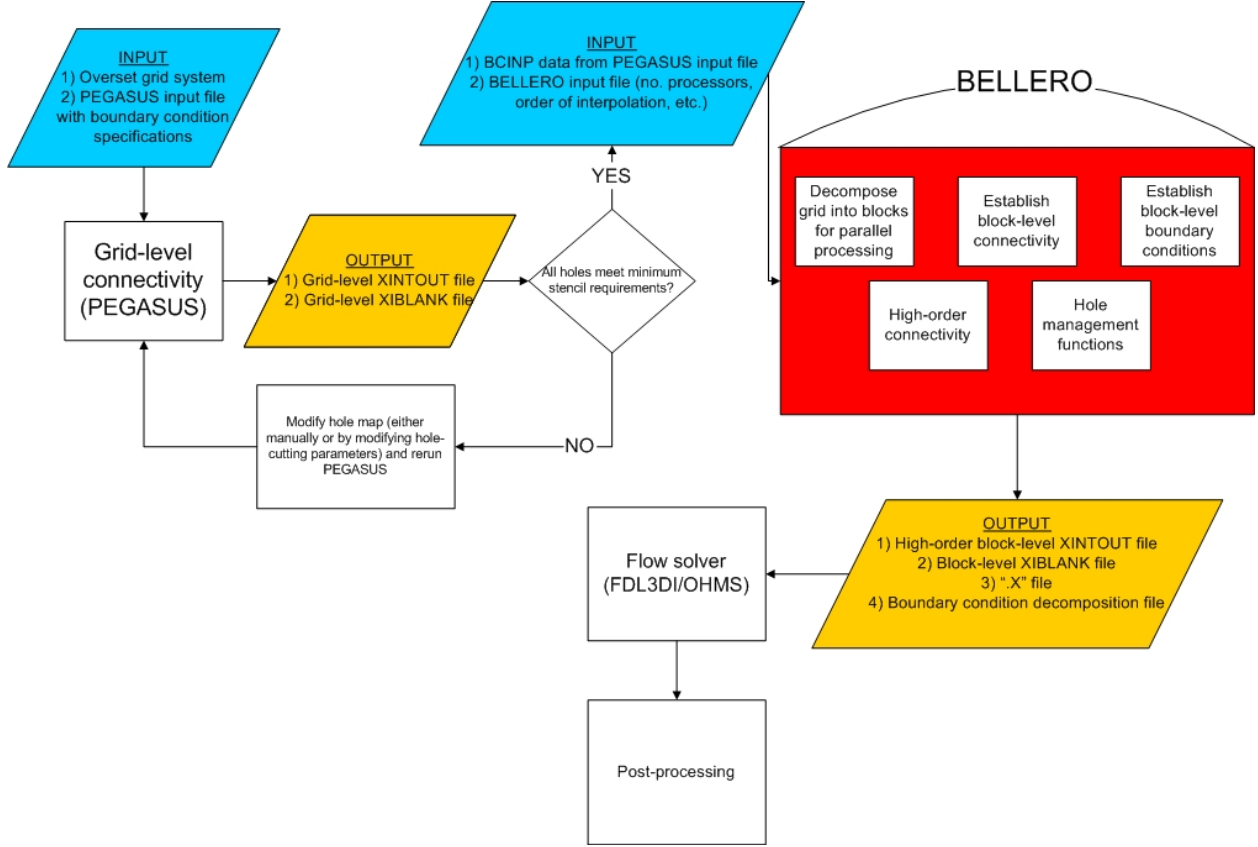


Figure 5.1: Workflow diagram for the high-order overset-grid process.

the receiver point provide enough data to perform the second-order accurate trilinear interpolation that is typically used in overset methods. [58] A second required file, created by running the *PEGASUS* utility *pegplot*, will be referred to as the “XIBLANK” file. This file is a multi-block, iblanked, *PLOT3D* grid file where the iblank value for each receiver point is equal to the negative value of the corresponding donor grid.

In order to facilitate the application of the overset-grid approach to high-order computational simulations, several additional preprocessing steps are necessary once *PEGASUS* has been executed and the *XINTOUT* and *XIBLANK* files generated. At this point in the development of the HO-OG approach, some of these steps require significant user intervention, while others are completely automated. The main preprocessing code that has been developed to perform many of the automated tasks in the HO-OG process is referred to as *BELLERO* (Bellerophon was the mythological Greek hero who tamed the winged horse *PEGASUS*, upon whom he rode to slay the multi-component monster Chimera). The various tasks in the preprocessing phase of the HO-OG approach will now be discussed.

5.2.1 Hole Modification

For problems requiring *PEGASUS* to blank out points in one or more grid components, the first step is to ensure the compatibility of the resulting holes with the high-order algorithm. The high-order spatial algorithm, and in particular the filtering operation, need larger stencils than are typically required for lower-order simulations. For example, a $2N$ -order interior filter of the type employed in the algorithm require a $2N + 1$ -point stencil [23]. Thus a 10^{th} -order filter requires a minimum of eleven contiguous, unblanked points along a coordinate direction to correctly operate.

The requirement to maintain adequate stencil sizes for the high-order differencing and filtering operators places some restrictions on the nature of the holes that can be handled with the HO-OG approach. The

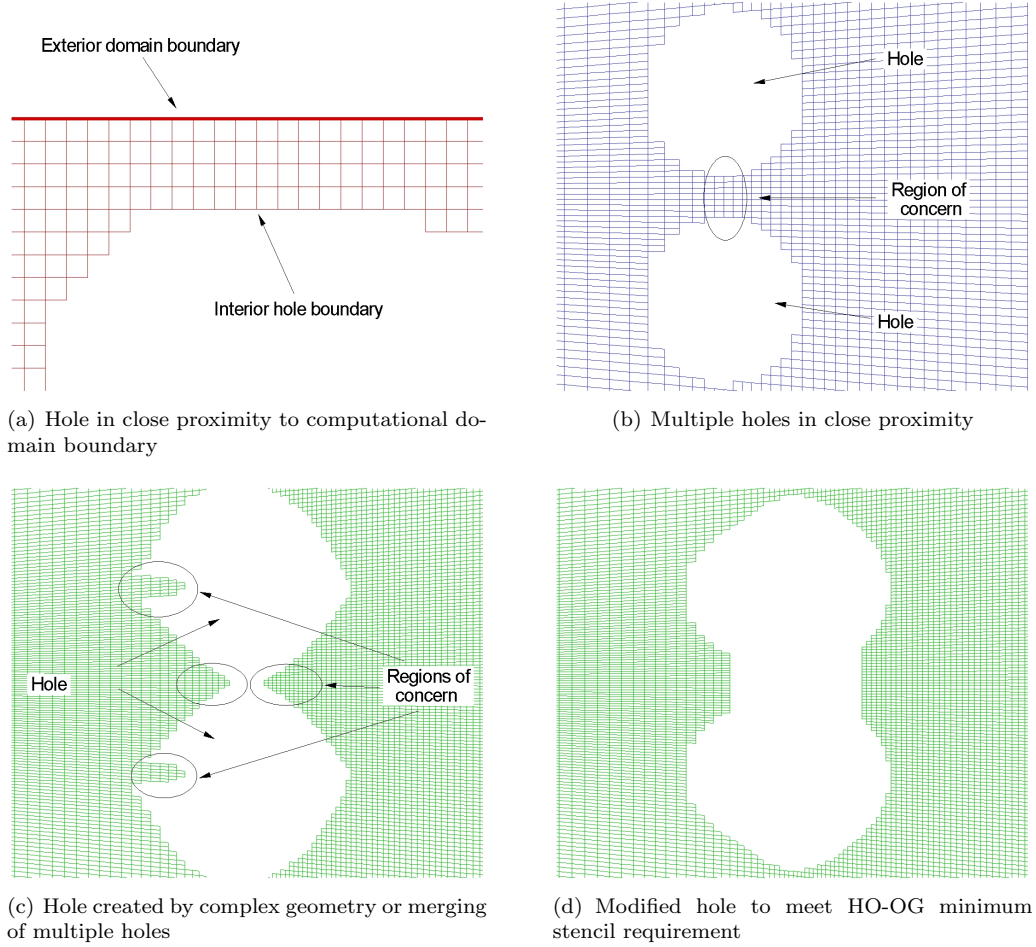


Figure 5.2: Situations showing linkage between holes and minimum stencil sizes

obvious one is that any holes generated must not result in stencils with fewer than some minimum number of points in any of the three coordinate directions. This minimum value is dictated by the order-of-accuracy of the differencing and/or filtering operator to be used by the solver. Stencils containing points below the minimum prescribed value may arise due to the proximity of the hole to a exterior domain boundary (e.g., Figure 5.2(a)), due to two distinct holes in close proximity to each other (Figure 5.2(b)), or due to the presence of unblanked points protruding into a blanked region (Figure 5.2(c)). This later situation can arise due to the merging of holes generated by two or more distinct bodies in close proximity, as is the case in Figure 5.2(c), or due to a sufficiently complex grid geometry that is used to cut the hole.

A second point that should be considered when working with holes at the grid-topology level is how the holes will impact the partitioning phase. As discussed in the following section, the minimum stencil requirement poses a constraint on how the partitioning may be accomplished. Thus, the hole structure at the grid-topology level plays an important role in the quality of the decomposition at the block-topology level. Here it will suffice to make the general statement that the more regular the hole boundaries are (that is, lacking in the “stair-step” behavior where the hole boundary moves in multiple coordinate directions at a time), the more flexibility will exist when decomposing the grids.

The situation depicted in Figure 5.2(c) arose during the simulation of low-Reynolds number flow over two circular cylinders in close proximity. [30] Using the Level-2 interpolation capability [56] of *PEGASUS*, this hole pattern was cut by the body-fitted grids surrounding the two cylinders into the background grid. Identified in Figure 5.2(c) are some of the regions where limited stencil support existed. The HO-OG method would not be able to support this hole structure, and thus modifications were required prior to performing

the simulation. The modified hole structure is shown in Figure 5.2(d), where the iblank value of several points has been modified in order to maintain some minimum stencil size (fifteen in this case).

Currently, the modification of the hole points must be done in manual and iterative fashion. First, a utility code is run to identify and report the locations where the number of contiguous, unblanked points along each coordinate direction fall below some user-specified value. A second utility code is then run that allows the user to flip the values of the iblank array in the `XIBLANK` file at specified points, thus potentially changing the shape of any holes. The *PEGASUS* utility program `p3d2peg` is then used to enforce the new hole map in *PEGASUS*, which is run again to establish the connectivity for this modified situation. This manual approach of check stencils / modify iblanks / rerun *PEGASUS* is repeated as often as necessary in order to obtain a grid whose connectivity is well-defined (i.e., no orphan points generated) and whose stencils are all equal to or larger than the minimum specified size. The hole-cutting parameters in *PEGASUS* may also be modified in order to assist in generating an overset-grid system compatible with the HO-OG minimum stencil requirement.

Future development may include the investigation of automated methods to perform the necessary hole modifications with minimal user input. Such an approach could be based on a comparison of the grid points *PEGASUS* would prefer to blank out through Level 2 interpolation so as to minimize the differences in cell size and orientation, and the grid points that *PEGASUS* must blank out due to their location inside a solid surface boundary. Such a comparison would identify points that could potentially be unblanked in order to meet HO-OG minimum stencil requirements. However, this approach will require additional research to determine its feasibility and practicality for realistic geometries.

5.2.2 Automatic Block Partitioning

The parallelization of the *FDL3DI* code was performed using an overset-grid paradigm, where the computational grids are decomposed into overlapping blocks and then assigned to an individual processing element [59]. While the decomposition of the grids into blocks is relatively straightforward on single-grid topologies, there are load-balancing issues associated with domain decomposition approaches on general overset-grid systems [60]. Also, in addition to being satisfied on the grid-level topology, the minimum stencil requirements must also be satisfied at the block level. As mentioned in the previous section, the presence of holes in a computational domain thus introduces additional constraints on how the domain may be partitioned. A decomposition that is both load-balanced and meets minimum stencil requirements becomes difficult to obtain manually as the number of grids and the complexity of the holes increases. Thus, automated methods to perform the decomposition under the minimum stencil requirement constraint were investigated. An approach was developed in-house to perform this task, which is discussed in this section.

There are four main steps to the automatic partitioning capability developed here. The first step is to determine the number of blocks into which each grid should be decomposed. An initial estimate of the number of blocks per grid is performed and adjusted until the total number of blocks matches the specified number of processors. Next, various combinations of cuts that will result in the calculated number of blocks on each grid are evaluated to determine which combination produces the minimum surface-to-volume ratio in order to minimize communication overhead. This is done through a simple iterative approach. The third step is to then apply these “optimal” cuts to each individual grid to decompose it.

The final step in the automated decomposition process is to account for iblanking and enforce minimum stencil requirements. This is done by first flagging every point in the grid that would not satisfy the minimum stencil if a cut were to be made through it in a given direction (thus each point will have three flag values, one for each of the three coordinate directions). Thus, the shape of any holes will have an impact on how the grid may be partitioned, with more uniform hole boundaries resulting in more flexibility when decomposing the grids. Once all grid points have been flagged and the individual grids have been cut, a check is performed to find all cuts which cross points which have been flagged for the given direction. When a cut is found to cross a point which violates the minimum stencil requirement, the cut plane is moved to the closest valid plane. After all of the necessary cut planes have been moved, the remaining planes are adjusted in order to even out the block sizes as much as possible.

An alternate way to account for iblanking is to create sub-grids. When creating sub-grids from planes that have moved, the partitioning process is identical up to the point where cut planes were moved in order to account for iblanking. At this stage, an additional step is added to create sub-grids which satisfy the

minimum stencil. These sub-grids are then partitioned as if they were an additional grid associated with the original system of grids. This allows for highly irregular blocks to be created, which otherwise is not possible by simply making cuts which extend the entire plane of a grid. All of the cut planes forced to move are evaluated as potential planes to create sub-grids. At the end of either sub-grid generation, an attempt is made to even out the size of the sub-grids where possible. This is done by shifting cut planes where the sub-grids were generated on the sub-grid which contains the block with the largest volumes.

The above process is still in the developmental phase. It has been successfully demonstrated for a variety of straightforward geometries involving holes (see Sec. 5.4), but needs to be proven for more complex configurations. Additional flexibility in allowing the user to specify a range of processors to consider for obtaining the best load-balanced decomposition, as well as utilizing other established domain decomposition approaches that could be modified to account for iblanking, are concepts under consideration for future development.

5.2.3 Block Connectivity and Periodic Boundary Conditions

Once the partitioning for the grid topology has been specified, the block-level connectivity must be determined. There are three components to this step; (1) decomposing the grid-level connectivity data provided by *PEGASUS* and assigning it to the proper blocks, (2) establishing the point-to-point intragrid connectivity requirements such that the blocks decomposed from a single grid can communicate with each other, and (3) establishing the point-to-point connectivity necessary for the application of any periodic boundary conditions. Previously, the first two of these steps were handled by running *PEGASUS* on the decomposed grid to establish the necessary block-level connectivity. However, this approach had several drawbacks. First, it was discovered that the presence of block boundaries throughout the computational domain seemed to hamper the ability of *PEGASUS* to create high-quality holes using its automated hole-cutting process. The work-around developed to deal with this issue was to run *PEGASUS* to perform the hole-cutting on the grid-level topology, and then rerun it using the resulting hole-map to establish the block-level connectivity. For larger grids with many blocks, the time required to rerun *PEGASUS* could be substantial as the connectivity of all direct-injection interpolation points had to be established using the same algorithm used for the donor/receiver points in general overlapping regions of the grids (in addition to the reestablishing the connectivity of the already calculated overlaps on the correct block). Also, to correctly specify the block-level boundary condition input data required by *PEGASUS* for cases with increasingly larger number of processors required significant user involvement and hence was time-consuming and prone to error. The assignment of periodic boundary conditions also required considerable user input, with the necessary message-passing constructs hardwired by the user based on the specifics of the problem and the particular decomposition employed. Finally, the resulting connectivity data generated through this process was valid only for a particular decomposition; any changes (including the number of processors to run the case on) required a significant effort on the part of the user in recreating the *PEGASUS* boundary condition data, rerunning *PEGASUS* on the new block topology, and modifying the code to correctly handle any periodic boundary conditions.

Part of the development of *BELLERO* was thus geared towards finding alternative ways to determine block-level connectivity. This issue was addressed in order to streamline application of the high-order algorithm to new configurations of interest while enhancing the flexibility of the algorithm by relieving the user of much of the burden associated with establishing the block-level connectivity for a particular decomposition. One of the key features of *BELLERO* is its ability to establish the block-level connectivity information for a specific overset-grid system given the grid-level connectivity data (obtained from *PEGASUS*) and an arbitrary grid partition (either user-supplied or determined by the autopartitioning capability described in the previous section). The point-to-point connectivity for intragrid boundaries as well as the periodic face boundaries are handled in a similar manner. First, the linkages between periodic faces are determined using data from the BCINP namelist in the *PEGASUS* input file. Both the O-type overlap as well as the more general case where the periodic faces are physically separated are handled by *BELLERO*. In both cases, a boundary condition type (variable IBTYP from *PEGASUS*) that is not utilized by *PEGASUS* is selected to flag each type of periodic condition. For O-grid periodicity, each pair of periodic faces is flagged using IBTYP=20 in the BCINP namelist input. For each pair of non-O-type periodic faces, a unique value of IBTYP ≥ 200 is selected for both faces to provide the linkage needed to establish the correct donor/receiver pairs.


```

!          DEFINE GRIDS
!
!  GRID-001 = Body-fitted cylindrical grid near cylinder
!  GRID-002 = Cylindrical near-background grid
!  GRID-003 = Wake grid
!  GRID-004 = Background cartesian grid
!
!

```

```

$BCINP
  ISPARTOF = 'GRID-001',
  IBTYP = 20, 20, 1, 201, 201,
  IBDIR = 1, -1, 2, 3, -3,
  JBCE = 1, -1, 1, 1, 1,
  JBCE = 1, -1, -1, -1, -1,
  KBCE = 1, 1, 1, 1, 1,
  KBCE = -1, -1, 1, -1, -1,
  LBCE = 1, 1, 1, 1, -1,
  LBCE = -1, -1, -1, 1, -1,
$END

```

```

$BCINP
  ISPARTOF = 'GRID-002',
  IBTYP = 202, 202,
  IBDIR = 3, -3,
  JBCE = 1, 1,
  JBCE = -1, -1,
  KBCE = 1, 1,
  KBCE = -1, -1,
  LBCE = 1, -1,
  LBCE = 1, -1,
$END

```

```

$BCINP
  ISPARTOF = 'GRID-003',
  IBTYP = 203, 203,
  IBDIR = 3, -3,
  JBCE = 1, 1,
  JBCE = -1, -1,
  KBCE = 1, 1,
  KBCE = -1, -1,
  LBCE = 1, -1,
  LBCE = 1, -1,
$END

```

```

$BCINP
  ISPARTOF = 'GRID-004',
  IBTYP = 32, 32, 32, 32, 204, 204,
  IBDIR = 1, -1, 2, -2, 3, -3,
  JBCE = 1, -1, 1, 1, 1, 1,
  JBCE = 1, -1, -1, -1, -1, -1,
  KBCE = 1, 1, 1, -1, 1, 1,
  KBCE = -1, -1, 1, -1, -1, -1,
  LBCE = 1, 1, 1, 1, 1, -1,
  LBCE = -1, -1, -1, -1, 1, -1,
$END

```

(a) Example BCINP data input for *PEGASUS* with periodic boundary conditions specified

1	1	2	1	53	1	1	1	27
2	1	2	1	53	1	1	1	27
3	1	2	1	54	1	1	1	27
4	1	2	1	54	1	1	1	27
5	1	2	1	54	1	1	1	27
6	1	2	1	54	1	1	1	27
7	1	2	1	53	1	1	1	27
8	1	2	1	53	1	1	1	27
37	32	1	1	1	1	48	1	27
37	32	2	1	48	1	1	1	27
38	32	1	1	1	1	48	1	27
38	32	2	1	48	1	1	1	27
39	32	-1	48	48	1	48	1	27
39	32	2	1	48	1	1	1	27
40	32	-1	48	48	1	48	1	27
40	32	2	1	48	1	1	1	27
41	32	1	1	1	1	48	1	27
41	32	-2	1	48	48	48	1	27
42	32	1	1	1	1	48	1	27
42	32	-2	1	48	48	48	1	27
43	32	-1	48	48	1	48	1	27
43	32	-2	1	48	48	48	1	27
44	32	-1	48	48	1	48	1	27
44	32	-2	1	48	48	48	1	27

(b) Boundary condition output generated automatically by *BELLERO* for a forty-four block decomposition corresponding to Figure 5.3(a)

Figure 5.3: Sample boundary condition input (to *PEGASUS*) and output (from *BELLERO*)

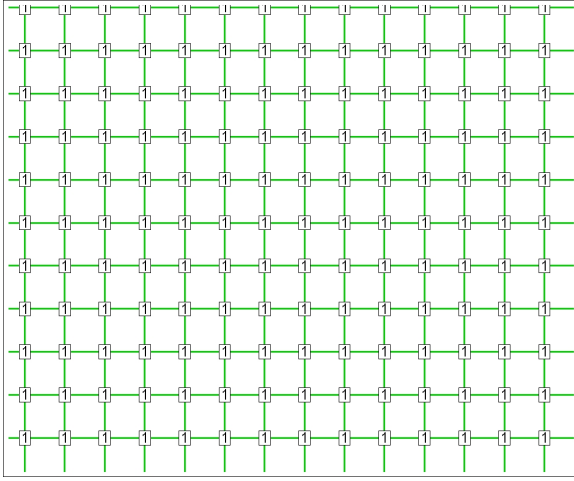
For both cases, the actual regions corresponding to the periodic overlaps must be provided by the user. An example of BCINP input data that involves the use of both types of periodic boundary conditions is given in Figure 5.3(a). This data corresponds to a overset-grid system used to examine the transitional flow over a circular cylinder at $Re_D = 3900$ [31]. The grid system consisted of four grids; a body-fitted cylindrical grid, a mid-field intermediary grid, a refined wake grid and a background cartesian grid. The cylindrical grid utilized an O-grid periodic face on the J_{min} and J_{max} faces (IBDIR ± 1), as indicated by the IBTYP value of 20 on each of these faces. In the L -direction (spanwise), periodic boundary conditions were employed, with the linkages between faces indicated by the various IBTYP values greater than or equal to 200. While in this case, all of the spanwise periodic linkages connect faces on the same grid, the IBTYP=20x can be used to link together faces from different grids as required by the topology of the problem. Conversely, the IBTYP=20 (if used) must be specified for one and only one pair of faces per grid. Also, more than two faces per grid can be specified as periodic using the IBTYP=20x flag as long as the constraint that each face matches point-to-point with one and only one other face is met. In the case where two or more adjacent faces on a grid are periodic, the algorithm will enforce all periodic conditions simultaneously. Thus, in the situation on a computational cube where each face is periodic with its opposite face (top-bottom, left-right, front-back), receiver points in the corners of the cube that are periodic in multiple directions will be directly paired up with their appropriate donors (top/right/front with bottom/left/rear, etc.).

Once the periodic linkages are established, the algorithm will examine all of the block faces resulting from the partitioning of the grid-level topology. If a block face is either an intragrid boundary created by the partitioning process, or if its an exterior grid boundary requiring periodic boundary conditions, then all points on the planes that are to receive data are flagged and the appropriate donor points are found. For these two situations, all interpolation is direct-injection, and thus the offsets are set identically equal to zero. An example of this process for an intragrid boundary is shown in Figure 5.4, which shows the values in the iblack array on an original grid entity (Figure 5.4(a)) and then the iblack values on one of the block entities (Block 20) arising from the decomposition of the grid (Figure 5.4(b)). On the original grid, the iblack values in the region shown are all unity indicating that these points are field points as determined by PEGASUS. After finding the direct-injection connectivity between blocks, the iblack array on Block 20 has been modified to show which blocks now provide the donor information along the block boundaries, indicated by a negative iblack value. Thus, on the portion of the receiver block shown in Figure 5.4(b), blocks 21, 24 and 27 provide the necessary donor points. As shown here, a five-point overlap region with a two-point fringe was employed between blocks, and thus a set of non-communicating overlap points [23] exists in each overlap region. In determining whether a point is a valid donor, the intragrid connectivity algorithm determines whether it is also a receiver point, and if so, eliminates it from consideration as a potential donor. Through this process, receiver points that lie in regions overlapped by more than two blocks (such as the central grey region in Figure 5.4(b)) will receive a valid donor point from the correct neighboring block. For points where two valid direct-injection donor points exist, as will occur along edges and corners of blocks at NCO points, the algorithm will simply select the point on the lowest-numbered block. An example of the connectivity between periodic O-grid faces is also shown in Figs. 5.5, which demonstrates the connectivity between two blocks (Blocks 4 and 8) across the common periodic face.

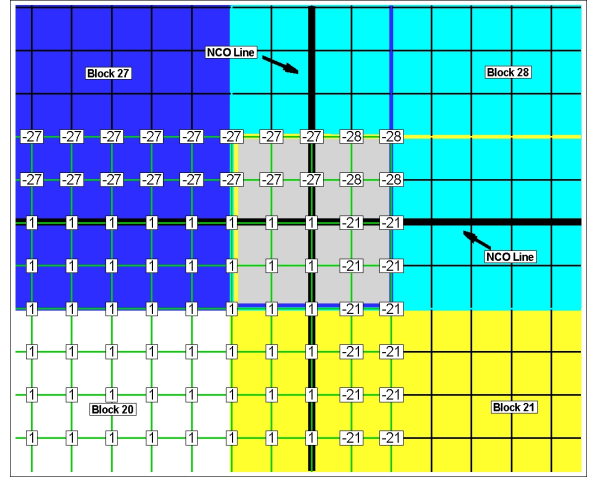
The third part of establishing the block-level connectivity involves the decomposition of the grid-level connectivity provided by PEGASUS. This is accomplished by finding all receiver points identified by PEGASUS that reside on each block, and then determining the associated donor points using the data in the IBC array from PEGASUS. Every block that each donor point could reside on is then identified, and the valid donor point that results in the largest quality factor [61] is selected. An example of the decomposition of grid-level connectivity is given in Figs. 5.6(a) and 5.6(b). The original values in the iblack array associated with the receiver grid indicate the donor grid providing the data. After decomposition, the appropriate block-level iblack values have been assigned. The donor/receiver point pairs are also recast into the block-level indexing system for consistency in the new decomposed topology.

5.2.4 Boundary Condition Decomposition

The previous approach for assigning boundary conditions in the high-order algorithm also required considerable user input. Boundary conditions were assigned on the block-level topology utilizing logical constructs hardwired directly into the code to assign each boundary condition to the appropriate block. While satisfac-

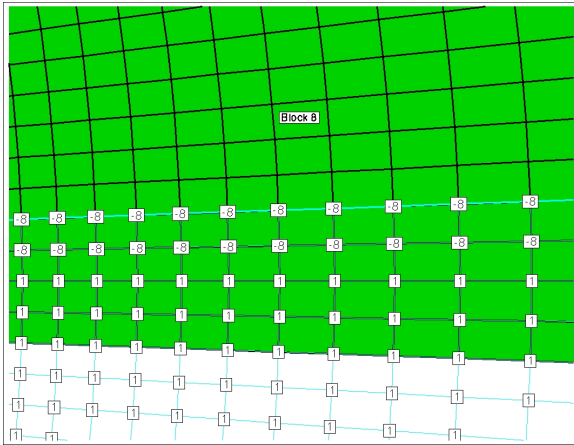


(a) Iblank values of grid prior to decomposition

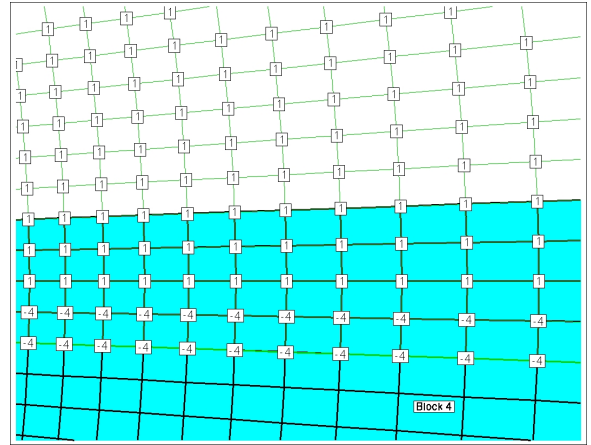


(b) Iblank values on block 20 after decomposition showing the donor blocks providing data at the block boundaries

Figure 5.4: Example of intragrid boundary connectivity



(a) Iblank values of block 4 along O-grid periodic boundary (shared with block 8)



(b) Iblank values of block 8 along O-grid periodic boundary (shared with block 4)

Figure 5.5: Example of periodic O-grid boundary connectivity

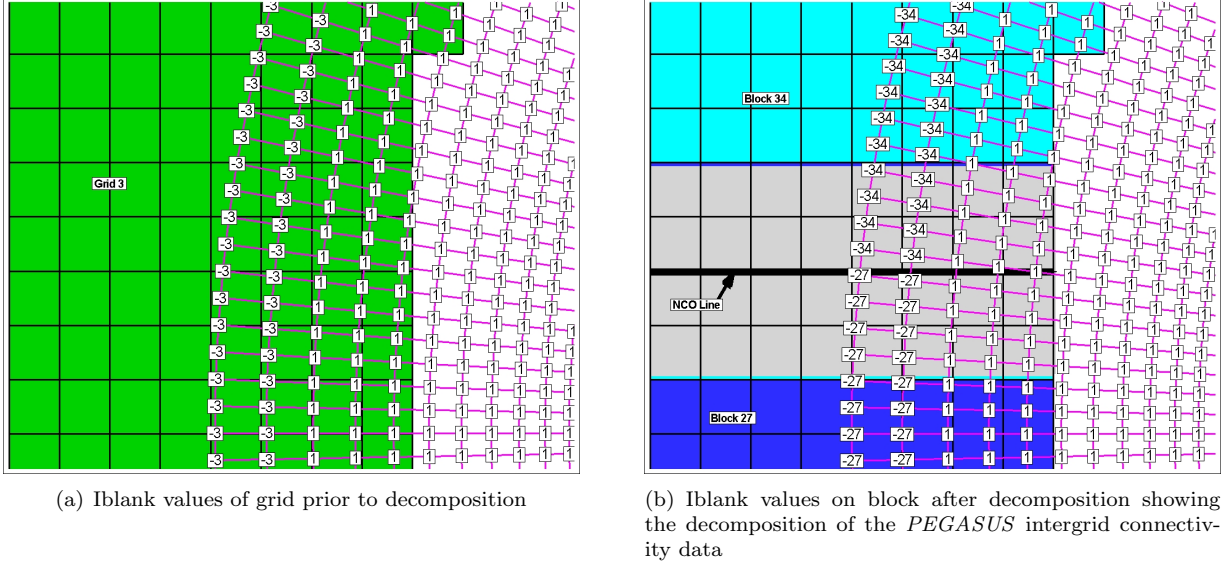


Figure 5.6: Example of intergrid boundary connectivity

tory for basic geometries and/or small number of processors, this approach was clearly self-limiting as more complex configurations were considered and larger numbers of processors were brought to bear on problems. Like the previous approach for dealing with block-level connectivity, this method for handling boundary conditions was also inflexible in the sense that any changes in the partitioning of the grids would require direct modifications to the code.

To increase the flexibility of the algorithm and to simplify its application to problems involving complex geometries and/or large numbers of processors, an effort was made to relieve the user of the burden of manually specifying block-level boundary conditions. As *PEGASUS* is used to provide grid-connectivity, and since *PEGASUS* requires boundary condition input in order to determine which grid boundaries will receive interpolated data, it was decided to utilize the grid-level boundary condition data in the *BCINP* namelist from the *PEGASUS* input file as the starting point for this effort. Consider the example *PEGASUS* *BCINP* namelist input as given in Figure 5.3(a) for the case of transitional flow over a circular cylinder. In addition to the linkages for the periodic boundary conditions, all other grid-level boundaries that require boundary conditions applied in the flow solver are specified in this file. The new boundary condition preprocessor that is part of *BELLERO* now takes this grid-level boundary condition data directly from the *PEGASUS* input file and determines how it is to be applied at the block-level. An example of the output generated by the preprocessor is given in Figure 5.3(b) for a forty-four processor decomposition. This data is then used by the flow solver to determine how to apply the specified boundary conditions to the particular block-topology being employed. Note that the boundary conditions associated with periodic boundaries in Figure 5.3(b) are not represented in the boundary condition decomposition file as they are handled through the domain connectivity function.

5.2.5 High-Order Connectivity

Once it has determined how to decompose the overset-grid system and the block-level connectivity and boundary condition assignments have been generated, *BELLERO* then begins the process of establishing high-order connectivity for the overset grids is covered. It has been previously shown [62, 63] that the use of low-order interpolation is not sufficient to maintain the overall accuracy of a high-order method. Thus, extending the low-order interpolation data provided by *PEGASUS* to higher orders is an important part of the overall HO-OG algorithm. Previous work [30] determined that an explicit interpolation procedure based on successive one-dimensional applications of Lagrangian interpolation formulae was well-suited to maintain overall high-order accuracy within the HO-OG framework, and that is the only interpolation

method currently employed in the HO-OG algorithm.

The establishment of high-order connectivity by *BELLERO* is a three-step process. In the first step, the second-order stencils generated by *PEGASUS* are expanded such that the dimension of the stencil in each coordinate direction equals the specified order of the interpolation. The expansion is accomplished such that the receiving point will be as centered as possible within the resulting high-order stencil. The second step involves the calculation of the high-order interpolation offsets (the mapping of the physical location of the receiver point in the computational space of the associated donor grid) using the newly created high-order stencils. The offsets in each of the three coordinate directions are found by solving three isoparametric mapping equations, utilizing the second-order offsets found by *PEGASUS* as a starting point for the iterative Newton’s method used to solve the equations. The final step is the calculation of the Lagrangian interpolation coefficients associated with each receiver point using the high-order offsets. A total of $3N$ coefficients are required to fully specify a three-dimensional, N^{th} -order interpolation process for each receiver point. More detail on the determination of the high-order connectivity can be found in Ref. [30].

5.2.6 Hole Management

The final issue addressed by *BELLERO* is that of hole management. The concept of holes, i.e., points that are excluded from consideration by the flow solver due to their location inside of a solid surface or in an overlapping region that is better resolved by another grid, is a powerful technique in overset-grid methods. Its utilization greatly enhances the overall flexibility of the approach and has the potential to simplify the generation of overset grid systems. Hole management in *BELLERO* consists of three elements; the identification of hole boundary points in each of the three coordinate directions, the insertion of the appropriate one-sided boundary formulations for the differencing and filtering operations at all points impacted by the hole boundary, and the insertion of the hole decoupling coefficients at all points within the hole boundary. Each of these three elements are also discussed in detail in Ref. [30].

5.2.7 *BELLERO* Input and Output

To summarize, *BELLERO* requires as input four files. These are the grid-level *XIBLANK* and *XINTOUT* files that are generated by *PEGASUS* or its *pegplot* utility, a *PEGASUS*-style input file containing the *BCINP* data in order to process periodic boundary conditions and decompose other boundary conditions for the block-level topology, and an input file containing input data to manage how *BELLERO* executes. Upon completion of *BELLERO*, four primary files are generated that are used either used for diagnostic purposes or employed directly into the flow solver. The first one is the high-order, block-level *XINTOUT* file. This file is structurally consistent with the second-order, grid-level *XINTOUT* file generated by *PEGASUS*. However, it is based on the block-level topology and thus includes all of the necessary point-to-point communication between blocks as well as any periodic boundary conditions. Also, the general connectivity data, namely the base donor points and interpolation offsets, have been upgraded to allow for high-order interpolation. The second file is referred to as the “.X” file and contains some additional data required for application of the high-order interpolation process, such as the size of the stencil and the Lagrangian interpolation coefficients associated with each donor point, as well as data that marks the start and finish of any holes along each constant coordinate line in all three coordinate directions. The third file is the boundary condition decomposition file, an example of which was shown in Figure 5.3(b). This file allows the grid-level boundary conditions specified in the *PEGASUS* input file to be applied on the block-level topology without user intervention. Finally, the fourth file is the decomposed *XIBLANK* file containing the decomposed grid and *iblack* array in *PLOT3D* format. This file is very useful for plotting and diagnostic purposes.

5.3 Flow Solver

The baseline flow solver for use with *BELLERO* is *FDL3DI* [40], an in-house research code developed in the Computational Sciences Center of Excellence of the Air Force Research Laboratory for simulating the Navier-Stokes and Euler equations. The main spatial algorithm is based on fourth- and sixth-order compact finite differences with up to tenth-order spatial filters to maintain stability and accuracy by remove

spurious oscillations. Available time integration methods include both an explicit Runge-Kutta fourth-order temporally accurate scheme as well as an implicit, approximately factored Beam-Warming scheme of up-to-third-order temporal accuracy that employs diagonalization and Newton subiterations to maintain efficiency and accuracy, respectively. The code has been equipped with a general overset-grid capability using Message Passing Interface (MPI) calls, which also serves as a domain decomposition paradigm for utilization on parallel, distributed memory platforms [59]. Additional subroutines have been incorporated to perform the high-order interpolation using the coefficients and donor stencils calculated by *BELLERO*. Also, hole management subroutines have been included to read in *BELLERO* generated hole data and insert the appropriate one-sided differencing and filtering formulas at hole boundaries as well as decouple the points interior of the hole. Two routines were added to process the new boundary condition data generated by *BELLERO*; one to read and store the information and one to implement the boundary conditions in a general fashion. Finally, the I/O routines were modified so that restart data could be read in using the block-level topology, or it could be read in on the grid-level topology and decomposed internally and assigned to the appropriate blocks.

In addition to this code, a derivative code based on *FDL3DI* was developed to further enhance the flexibility of the high-order algorithm. Titled *OHMS* (for *Overset High-order Maxwell Solver*), this code employs several Fortran 90 features such as allocatable arrays and modular code structure to further streamline problem set-up. All subroutines dependent upon the equation set being simulated are grouped together in modules, which enables the rapid application of the algorithm to a variety of situations. Three equation sets are currently using this approach; the Euler equations and the Maxwell equations (examples of which are given in the following section), and the Maxwell equations with an added model for simulating electromagnetic propagation through plasmas [64]. Future plans include incorporating the Navier-Stokes equations into the *OHMS* framework as well as adding the Beam-Warming time-integration scheme (Runge-Kutta is the only time integration scheme implemented in the *OHMS* version of *FDL3DI*).

5.4 Examples

Two validation cases are examined here to demonstrate the use of the newly developed preprocessing capability of *BELLERO* coupled with the *OHMS*-based version of *FDL3DI*. Additional validation cases may be found in Ref. [64].

5.4.1 Acoustic Scattering from Three Cylinders

This case simulates the scattering of acoustic waves generated by a spatially distributed source from three circular cylinders. It was one of the benchmark problems in the Fourth Computational Aeroacoustic Workshop [65], and serves as a good validation case due to the presence of an analytic solution [66] for comparison. This particular configuration has been investigated [32] using the previous approach of manually decomposing the grids and boundary conditions down to the block-level as well as rerunning *PEGASUS* after the hole-cutting phase to generate all block-level connectivity. Now, *PEGASUS* is employed to cut the holes and generate the grid-level connectivity only, and the decomposition of the grids and boundary conditions and the generation of the block-level connectivity is handled by *BELLERO*.

The cylinder configuration shown in Figure 5.7(a) is gridded using three meshes; body-fitted grids about each cylinder embedded in a background Cartesian mesh. Additional details about the grid system employed as well as the parameters of the acoustic source may be found in Ref. [32]. Three decompositions were automatically generated using *BELLERO*, including sixteen, thirty-two, and sixty-four block configurations. Pertinent data for these automatically generated partitions, as well as data from the manually generated, twenty-eight block partition used in Ref. [32], is shown in Table 5.1. The *OHMS* code with the Euler equation module was employed, using sixth-order interior differencing, tenth-order spatial filtering, and the Runge-Kutta time integration algorithm with $\Delta t = 0.002$, to advance the solution for 20,000 time steps. The RMS fluctuating pressure profiles on the surface of the left and top cylinders were collected over the last 2,000 time steps of the run to use for comparison purposes. The results from the *BELLERO/OHMS* cases are given in Figure 5.7(b) and show a good agreement between the various cases, the previous results, and the analytic solution. Note that generating the various solutions shown here only required that the parameter controlling the number of blocks to decompose the problem into be modified and that *BELLERO* be rerun.

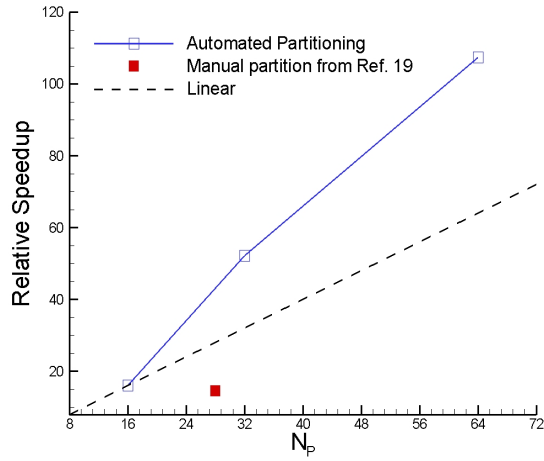
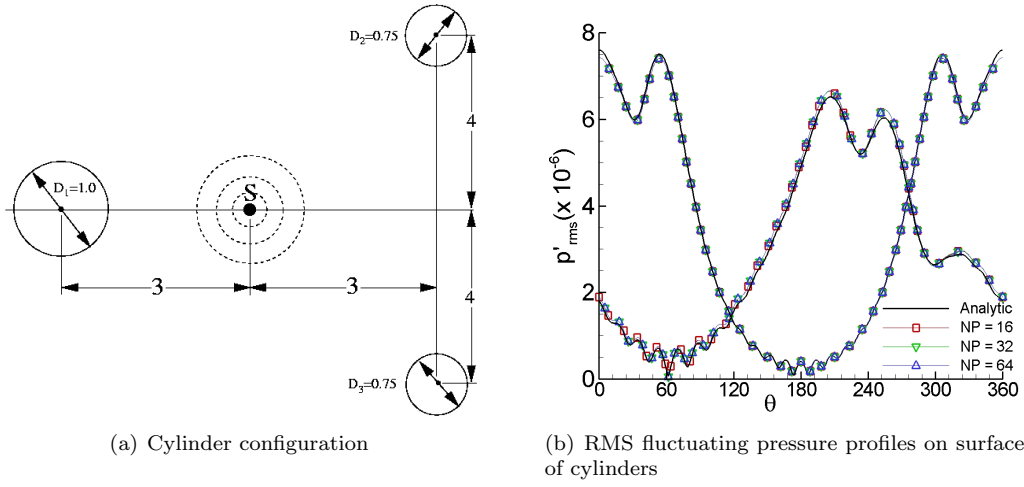


Figure 5.7: Results from acoustic scattering validation problem

NP	MBV	LBC	SVR	MMR
16	65,510	0.864	0.698	0.66
32	32,190	0.875	0.709	0.67
64	14,976	0.989	0.727	0.90
28	33,660	0.967	0.713	0.64

Table 5.1: Block decomposition data for acoustic scattering case (NP = number of processors, MBV = maximum block volume, SVR = average surface-to-volume ratio, MMR = minimum volume to maximum volume ratio)

NP	MBV	LBC	SVR	MMR	Wall-clock time (sec.)
12	195,112	0.859	0.107	0.28	9,700.3
16	171,820	0.799	0.082	0.31	13,381.8
32	86,469	0.849	0.118	0.62	8,015.3

Table 5.2: Block decomposition data for electromagnetic scattering case (see Table 5.1 for column headings)

Conversely, the previous methodology would have required generating the grid indices manually, generating the block-level *PEGASUS* boundary condition input, rerunning *PEGASUS* to regenerate the connectivity, modifying the code parameters to correctly dimension the arrays and the block-level logic in the boundary condition subroutine and recompiling the code, and generating a new restart file for the block configuration. This process would have to be repeated for each block topology to be examined.

While no formal scalability study was performed at this time, the relative speed-up referenced to the sixteen processor case on ASC/MSRC Compaq ES45 platform is plotted in Figure 5.7(c). When the partitioning is done automatically, superlinear speed-ups are obtained through this range of processors. Note the poor performance of the manually generated partition used in Ref. [32] compared to those automatically by *BELLERO*. It is believed that this is due to the large variation of the grid dimensions in the individual coordinate directions from one block to another in the manual partition, which could be causing some cache management problems. This issue is currently being investigated.

5.4.2 Electromagnetic Scattering from Single Sphere

The second case examined here is the scattering of electromagnetic plane waves at $ka = 4\pi$ from a single sphere. This case also is useful as a validation problem due to the existence of an analytic solution. [67] The sphere was gridded using the overset system as shown in Figure 5.4.2, which included a body-fitted polar grid with the poles removed around the sphere, two patch grids replacing the poles, and a background Cartesian grid. *BELLERO* was used to handle all necessary preprocessing requirements for a twelve, sixteen and thirty-two block configurations whose grid parameters are given in Table 5.2. The *FDL3DI*-derived *OHMS* code was used as the flow solver, this time employing the Maxwell equation module. The same solver configuration was employed as was used in the previous aeroacoustic case, with the solution being advanced 2000 time steps using a $\Delta t = 0.005$. The RMS electric field on the surface of the sphere was calculated over the last 1000 time steps for each decomposition, and the results are shown in Figure 5.9 compared to the analytic solution. Again, all decompositions match the analytic solution very well. The wall-clock times for this problem are also included in Table 5.2. For this case, the speed-ups obtained were considerably less than the previous aeroacoustic case, and in fact it took longer to run this case on sixteen processors than it did on twelve processors. These results are attributed to two factors. First, the irregular hole as shown in Figure 5.8(c) limits the flexibility of the decomposition process to obtain balanced blocks as indicated by the parameters in Table 5.2. Also, the sub-grid approach as previously discussed for automatically decomposing the grids was employed for the sixteen and thirty-two processor cases. This resulted in blocks whose indices varied considerably from block to block in the three coordinate directions (three sample block sizes from the thirty-two block case include $71 \times 25 \times 44$, $19 \times 83 \times 44$ and $41 \times 19 \times 83$). Thus, cache management issues could again be coming into play in these cases.

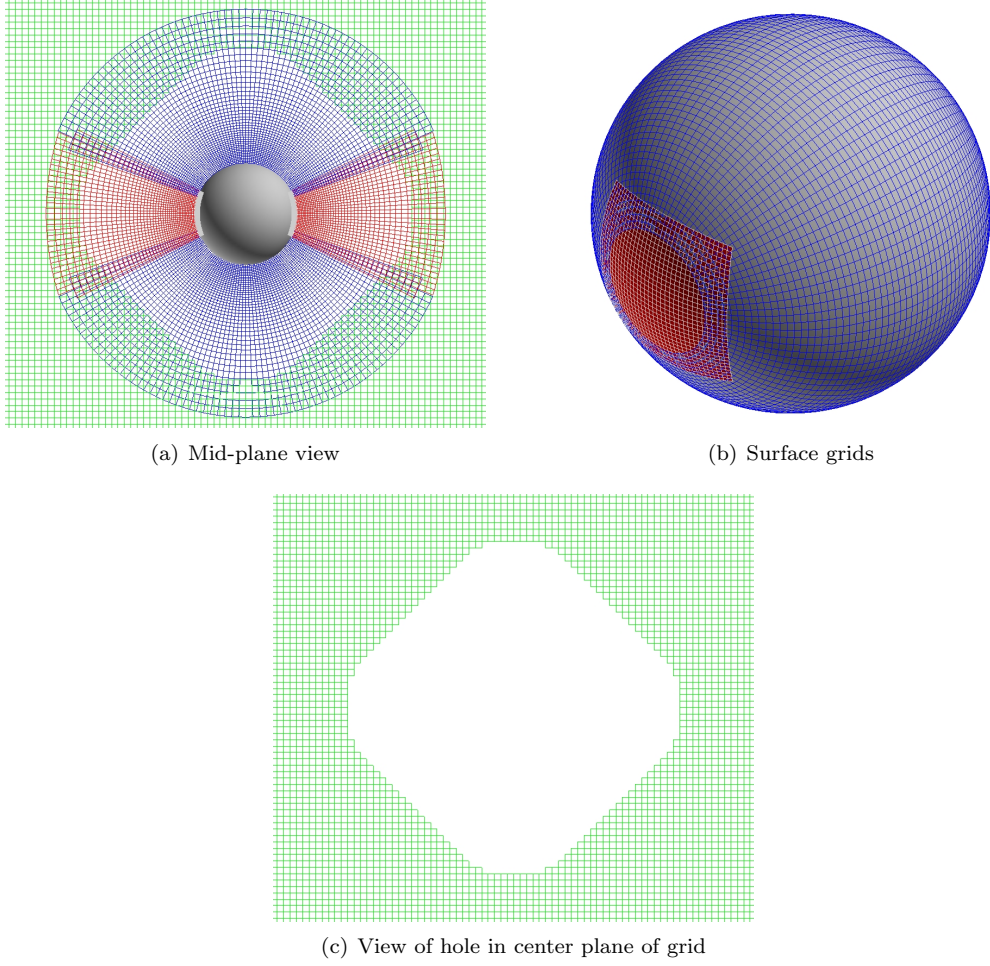


Figure 5.8: Overset grid system used for scattering from sphere

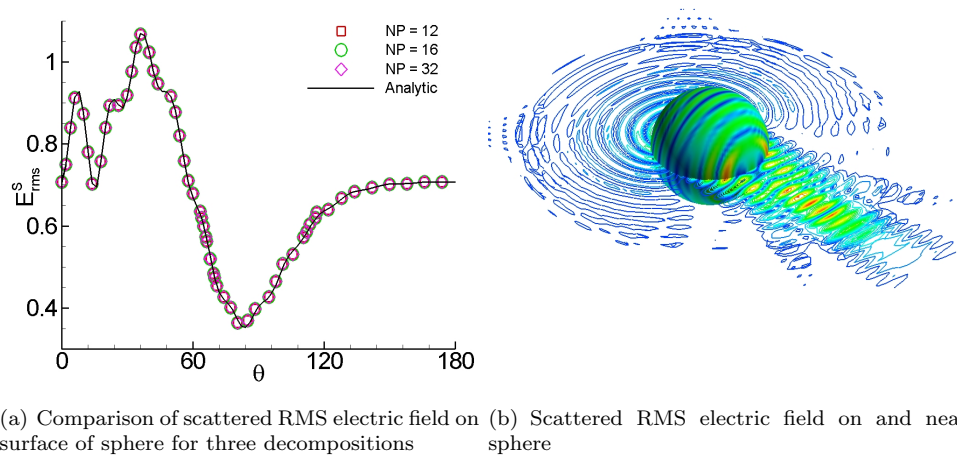


Figure 5.9: Results for EM scattering from sphere

Chapter 6

COMMUNICATION THROUGH PLASMA

6.1 Introduction

The present work decouples the solution of the non-equilibrium re-entry flow from the problem of wave propagation. A second-order Roe solver[36] is utilized to obtain the overall flow conditions and then the total and electron number densities and electron temperature are used to solve for the wave propagation. Equations for conservation of electron number density and momentum have been added to *OHMS* (Overset High-Order Maxwell Solver) developed at the Air Force Research Laboratory.[64]

6.2 Non-Dimensionalization of Governing Equations

The equations for wave propagation through an ionized medium is given by Maxwell's Equations (in the Rationalized MKSA system[68]):

$$\epsilon_0 \partial_t \mathbf{E} + \mathbf{J} - \nabla \times (\mathbf{B}/\mu_0) + \nabla \times \mathbf{M} = 0 \quad (6.1)$$

$$\partial_t \mathbf{B} + \nabla \times \mathbf{E} = 0 \quad (6.2)$$

$$\mathbf{M} = 0 \quad (6.3)$$

where the current is given by:

$$\mathbf{J} = \sum_s q_s n_s \mathbf{v}_s = \mathbf{J}_i + \mathbf{J}_e \quad (6.4)$$

with $\mathbf{J}_i = q_i n_i \mathbf{v}_i$ and $\mathbf{J}_e = -e n_e \mathbf{v}_e$. The number density equations for the electrons, ions and neutrals are[36, 69]:

$$\partial_t (n_e) + \nabla \cdot (n_e \mathbf{v}_e) = \sum_j (\dot{w}_{ej}^p + \dot{w}_{ej}^d) \quad (6.5)$$

$$\partial_t (n_i) + \nabla \cdot (n_i \mathbf{v}_i) = \sum_j (\dot{w}_{ij}^p + \dot{w}_{ij}^d) \quad (6.6)$$

$$\partial_t (n_n) + \nabla \cdot (n_n \mathbf{v}_n) = \sum_j (\dot{w}_{nj}^p + \dot{w}_{nj}^d) \quad (6.7)$$

where \dot{w}_{sj}^p is the production of species s from species j and \dot{w}_{sj}^d is the destruction of species s into species j subject to the constraint that:

$$\sum_s \sum_j (\dot{w}_{sj}^p + \dot{w}_{sj}^d) = 0 \quad (6.8)$$

similarly, the species momentum equations can be written as[36, 69]:

$$\partial_t (n_e \mathbf{v}_e) + \nabla \cdot (n_e \mathbf{v}_e \otimes \mathbf{v}_e) = -\frac{n_e e}{m_e} (\mathbf{E} + \mathbf{v}_e \times \mathbf{B}) - \frac{\nabla P_e}{m_e} + \frac{\mathbf{F}_{coll,e}}{m_e} + \sum_j (\mathbf{v}_e \dot{w}_{ej}^p + \mathbf{v}_j \dot{w}_{ej}^d) \quad (6.9)$$

$$\partial_t (n_i \mathbf{v}_i) + \nabla \cdot (n_i \mathbf{v}_i \otimes \mathbf{v}_i) = \frac{n_i q_i}{m_i} (\mathbf{E} + \mathbf{v}_i \times \mathbf{B}) - \frac{\nabla P_i}{m_i} + \frac{\mathbf{F}_{coll,i}}{m_i} + \sum_j (\mathbf{v}_i \dot{w}_{ij}^p + \mathbf{v}_j \dot{w}_{ij}^d) \quad (6.10)$$

$$\partial_t (n_n \mathbf{v}_n) + \nabla \cdot (n_n \mathbf{v}_n \otimes \mathbf{v}_n) = -\frac{\nabla P_n}{m_n} + \frac{\mathbf{F}_{coll,n}}{m_n} + \sum_j (\mathbf{v}_n \dot{w}_{nj}^p + \mathbf{v}_j \dot{w}_{nj}^d) \quad (6.11)$$

where $\mathbf{F}_{coll,s}$ is a force term for species s due to collisions and the last term on the right hand side of Equations (6.9)-(6.11) is the transfer of momentum due to creation and destruction of the species.

For the wave propagation problem, the variables are perturbed about the steady state solution obtained from the non-equilibrium solution.

$$\begin{aligned} \mathbf{E} &= \mathbf{E}_0 + \mathbf{E}_1 & \mathbf{B} &= \mathbf{B}_1 \\ n_e &= n_{e,0} + n_{e,1} & \mathbf{J}_e &= \mathbf{J}_{e,0} + \mathbf{J}_{e,1} \\ n_i &= n_{i,0} & \mathbf{J}_i &= \mathbf{J}_{i,0} \\ n_n &= n_{n,0} & \mathbf{v}_n &= \mathbf{v}_{n,0} \end{aligned}$$

As the plasma is assumed quasi-neutral, $n_{i,0} \approx n_{e,0} \equiv n_0$. The neutral species are unaffected by the wave propagation due to the lack of charge, while the ions can be considered “frozen” in relation to the electrons due the electron mass being significantly smaller than the ion mass. For the same reason, the collision force term is only a function of electron velocity:

$$\frac{\mathbf{F}_{coll,e}}{m_e} = -\nu_e n_e \mathbf{v}_e$$

where ν_e is taken as an average collision frequency between the electrons and neutrals. Electron-ion collisions are neglected with respect to the electron-neutral collisions due to the weak ionization of the flow[70]. When the steady-state solution is subtracted from (6.1)-(6.11), the following dimensional equations hold:

$$\epsilon_0 \partial_t \mathbf{E}_1 + \mathbf{J}_{e,1} - \nabla \times (\mathbf{B}_1 / \mu_0) = 0 \quad (6.12)$$

$$\partial_t \mathbf{B}_1 + \nabla \times \mathbf{E}_1 = 0 \quad (6.13)$$

$$\partial_t n_{e,1} - \frac{\nabla \cdot \mathbf{J}_{e,1}}{e} = 0 \quad (6.14)$$

$$\partial_t \mathbf{J}_{e,1} - \nabla \cdot \left(\frac{\mathbf{J}_e \otimes \mathbf{J}_e}{en_e} \right) = \left(\frac{e^2 n_e}{m_e} \right) \mathbf{E}_1 - \frac{e}{m_e} (\mathbf{J}_e \times \mathbf{B}_1) + e \frac{\gamma_e R T_e \nabla n_{e,1}}{m_e} - \nu_e \mathbf{J}_{e,1} \quad (6.15)$$

where the term proportional to $n_{e,1} \mathbf{E}_0$ is neglected due to the quasi-neutral approximation of the plasma. Because the electron plasma waves are driven by the Lorentz force, the compressions tend to be anisotropic and act locally one-dimensional, so $\gamma_e \approx 3$ is normally assumed [70, 71].

The following non-dimensionalizations may be made:

$$B^* = \mathbf{B}_1 / \mathcal{B}, E^* = \mathbf{E}_1 / \mathcal{E}, \mathbf{J}^* = \mathbf{J}_e / \mathcal{J} \quad (6.16)$$

$$t^* = t / \tau, \mathbf{x}^* = x / L \quad (6.17)$$

$$\mathbf{v}_e^* = \mathbf{v}_e / \mathcal{V} \quad (6.18)$$

$$n_e^* = n_e / n_{0,max} \quad (6.19)$$

$$m_e^* = 1 \quad (6.20)$$

$$\nu_e^* = \nu_e \tau \quad (6.21)$$

where the non-dimensional parameters are chosen such that:

$$L/\tau = c_0 \equiv 1/\sqrt{\mu_0 \epsilon_0} \quad (6.22)$$

$$\mathcal{B} = \mathcal{E}/c_0 \quad (6.23)$$

$$\mathcal{J} = \epsilon_0 \mathcal{E}/\tau = e n_{0,max} \mathcal{V} \quad (6.24)$$

which reduces to the non-dimensional form:

$$\partial_{t^*} \mathbf{E}_1^* + \mathbf{J}_{e,1}^* - \nabla^* \times \mathbf{B}_1^* = 0 \quad (6.25)$$

$$\partial_{t^*} \mathbf{B}_1^* + \nabla^* \times \mathbf{E}_1^* = 0 \quad (6.26)$$

$$\partial_{t^*} n_{e,1}^* - \beta \nabla^* \cdot \mathbf{J}_{e,1}^* = 0 \quad (6.27)$$

$$\partial_{t^*} \mathbf{J}_{e,1}^* - \beta \nabla^* \cdot \left(\frac{\mathbf{J}_e^* \otimes \mathbf{J}_e^*}{n_e} \right) = (\omega_p^2 \tau^2) (n_e^* \mathbf{E}_1^* - \beta (\mathbf{J}_e^* \times \mathbf{B}_1^*)) + \frac{v_{rms}^2}{c_0 \mathcal{V}} T_e^* \nabla^* n_{e,1}^* - \nu_e^* \mathbf{J}_{e,1}^* \quad (6.28)$$

where $\beta \equiv \mathcal{V}/c_0$ is a characteristic relativistic Mach number, $\omega_p = \sqrt{n_{0,max} e^2 / (\epsilon_0 m_e)}$ is the electron plasma frequency based on maximum electron density and $v_{rms} = \sqrt{3K\theta_e/m_e}$ is the molecular velocity of electrons with temperature scale θ_e ($T_e^* \equiv T_e/\theta_e$).

Defining new nondimensional variables: $\Omega_p \equiv \omega_p \tau$ and $\mathcal{M}_{th} \equiv \mathcal{V}/v_{rms}$, the equation for the electron current may be rewritten as:

$$\partial_{t^*} \mathbf{J}_{e,1}^* - \beta \nabla^* \cdot \left(\frac{\mathbf{J}_e^* \otimes \mathbf{J}_e^*}{n_e} \right) = \Omega_p^2 (n_e^* \mathbf{E}_1^* - \beta (\mathbf{J}_e^* \times \mathbf{B}_1^*)) + \frac{\beta T_e^*}{\mathcal{M}_{th}^2} \nabla^* n_{e,1}^* - \nu_e^* \mathbf{J}_{e,1}^* \quad (6.29)$$

For non-relativistic electrons one may assume $\beta \ll 1$ and the non-linear term $\mathbf{J}_e^* \otimes \mathbf{J}_e^*$ may be neglected. Since the current simulation assumes that there is no externally applied \mathbf{B} field, the $\mathbf{J}_e^* \times \mathbf{B}_1^*$ term may also be neglected.

Dropping the $*$'s for convenience, the equation set may be reduced to:

$$\partial_t \mathbf{E}_1 + \mathbf{J}_{e,1} - \nabla \times \mathbf{B}_1 = 0 \quad (6.30)$$

$$\partial_t \mathbf{B}_1 + \nabla \times \mathbf{E}_1 = 0 \quad (6.31)$$

$$\partial_t n_{e,1} - \beta \nabla \cdot \mathbf{J}_{e,1} = 0 \quad (6.32)$$

$$\partial_t \mathbf{J}_{e,1} = \Omega_p^2 n_e \mathbf{E}_1 + \frac{\beta T_e}{\mathcal{M}_{th}^2} \nabla n_{e,1} - \nu_e \mathbf{J}_{e,1} \quad (6.33)$$

Note that the divergence of current in Equation (6.32) cannot be dropped until \mathcal{M}_{th}^2 is defined.

6.3 Hypersonic Model

For the current simulation the background electrons are determined using the same second order Roe solver developed by Josyula and Bailey.[36] The hypersonic code utilizes a seven species model consisting of N_2 , O_2 , N , O , NO , NO^+ and e^- . The mass conservation assumed only binary collisions and the mobility was determined using a constant Lewis number. The ions experienced ambipolar diffusion while the electrons were assumed to be in Boltzmann equilibrium with the ions. In the original work, the wall was assumed non-catalytic and held at a fixed temperature of 1500K; however in the present work, catalytic walls for the electrons was assumed. For more details of this solution methodology, the reader is directed to reference [36].

The free-stream concentrations in the original code were too high for the atmospheric conditions at 61 km. While the values were still small enough to not affect the hypersonic shock or boundary layer, the electron density was still too high to allow waves to propagate in the free-stream. Figure 6.1 demonstrates this insensitivity to the free-stream values to the boundary layer along the stagnation line.

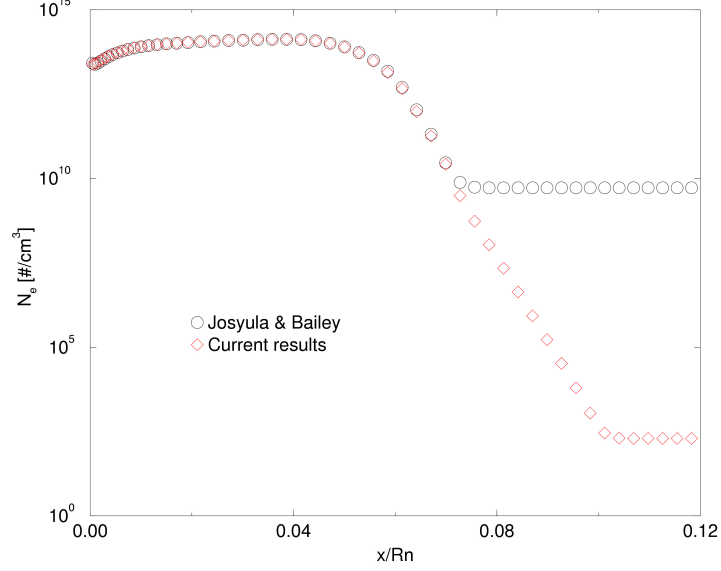
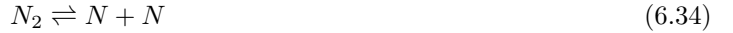


Figure 6.1: Comparison of electron density along the stagnation line with original and modified free-stream values. Distance is normalized by nose radius ($R_n=15.24$ cm).

Another modification to the code was the addition of catalytic boundary conditions at the wall. The accumulated space charge on the re-entry vehicle is not considered, as it would likely require not only solving the plasma sheath in more detail, but also the trajectory of the vehicle to account for its history. While the exact catalytic nature of the wall is not known in general, in the absence of space charge accumulation, the surface should probably be fully catalytic to at least the electrons and ions[72]. Although the code solves the non-equilibrium equations, it was not trivial to use these routines to determine the equilibrium conditions needed for the catalytic surface. Instead, a simple algebraic model for the equilibrium conditions was incorporated.

The equilibrium reactions for the 7 species model are (cf. [73]):



with equilibrium constants satisfying:

$$\frac{(p_N)^2}{p_{N_2}} = K_N(T) \quad (6.38)$$

$$\frac{(p_O)^2}{p_{O_2}} = K_O(T) \quad (6.39)$$

$$\frac{p_{NO}}{p_N p_O} = K_{NO}(T) \quad (6.40)$$

$$\frac{p_{NO^+} p_{e^-}}{p_N p_O} = K_{NO^+}(T) \quad (6.41)$$

Recalling that the mole-fractions are given by:

$$C_s = p_s/P \quad (6.42)$$

where p_s is the partial pressure of species s , and P is the total pressure; the mole fraction for atomic nitrogen and oxygen are related as:

$$C_N = \sqrt{C_{N_2} K_N(T)/P} \quad (6.43)$$

$$C_O = \sqrt{C_{O_2} K_O(T)/P} \quad (6.44)$$

Since at 1500 K, there is very little dissociation of oxygen and nitrogen, $C_{N_2}, C_{O_2} \approx \text{const}$, and the atomic species can be approximated as:

$$C_N = C_{N, P_{ref}} \sqrt{\frac{P_{ref}}{P}} \quad (6.45)$$

$$C_O = C_{O, P_{ref}} \sqrt{\frac{P_{ref}}{P}} \quad (6.46)$$

Similarly, for the mole fraction of NO :

$$C_{NO} = C_{NO, P_{ref}} C_N C_O \frac{P}{P_{ref}} \quad (6.47)$$

and utilizing the conservation of charge:

$$C_{e^-} = C_{NO^+} = C_{NO^+, P_{ref}} \sqrt{\frac{P_{ref}}{P}} \quad (6.48)$$

To ensure that the total number of species is conserved, the mole fractions for molecular nitrogen and oxygen are calculated from:

$$C_{N_2} + C_{O_2} + C_{NO} + C_O + C_N + C_{NO^+} + C_{e^-} = 1 \quad (6.49)$$

$$\frac{2C_{O_2} + C_{NO} + C_O + C_{NO^+}}{2C_{N_2} + C_{NO} + C_N + C_{NO^+}} = f_{tot} \quad (6.50)$$

where f_{tot} is the fraction of the total number of oxygen atoms divided by the total number of nitrogen atoms.

The algebraic approximations used the equilibrium values for $T = 1500^\circ K$ and $P_{ref} = 1$ atm. Equilibrium constants were calculated from values in the JANAF tables.[74] Figure 6.2 shows the agreement between the approximation and exact solution of the equilibrium equations along the body. The maximum deviation from the exact solution is less than 0.12%.

6.4 Results

The configuration modeled is that of the RAM C-II flight at an altitude of 61 km and Mach number of 23.9.[34, 35, 36, 64] The maximum electron temperature in the flow field was just under 10000 K and the maximum electron density was approximately $1.4 \times 10^{14}/\text{cm}^3$. The length scale (L) was taken to be 1 cm, the temperature scale θ_e to be 11600K and the electric field scale was chosen to be equal to that of a horn transmitting at 1 kW of power. Figure 6.3 shows the plasma shielding an incoming wave transmitting at 9.21 GHz.

The non-equilibrium solver was re-run with fully catalytic walls and walls that are only catalytic to charged particles. Unlike the change in the free-stream conditions[64], adding a catalytic wall boundary significantly alters the electron concentration throughout the boundary layer as seen in figure 6.4.

The horn antenna at a location 23.16 cm along the axis (location 2)[34] is shown in figure 6.5. While the original horn was circular, an equivalent rectangular horn was used to simplify the geometry. The vehicle grid and sub-domain including the horn can be seen in figure 6.6.

The presence of the ionized gas blocking signal can be seen in figure 6.7. The main factor affecting the signal propagation is the frequency of the wave. The effect of the catalytic boundary condition was also not apparently a large factor as seen in the 9.2 and 10.5 GHz signals in figure 6.8. The difference between that and an equivalent radiating aperture, while quantitatively different closer to the vehicle, the two signals become more similar further away. An early study[64] indicated that the solution did not appear to be converged. It was later determined that in the three grids, the antenna apertures were slightly different

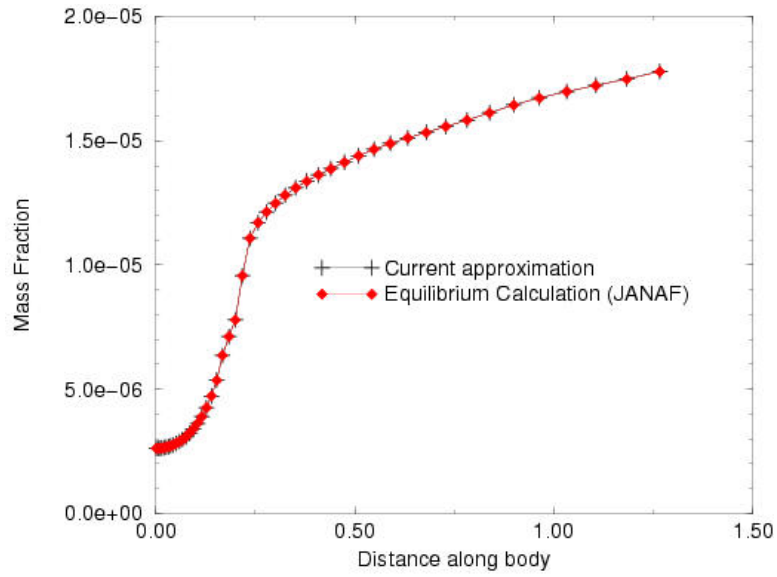


Figure 6.2: Comparison of atomic oxygen on surface of vehicle for fully catalytic walls.

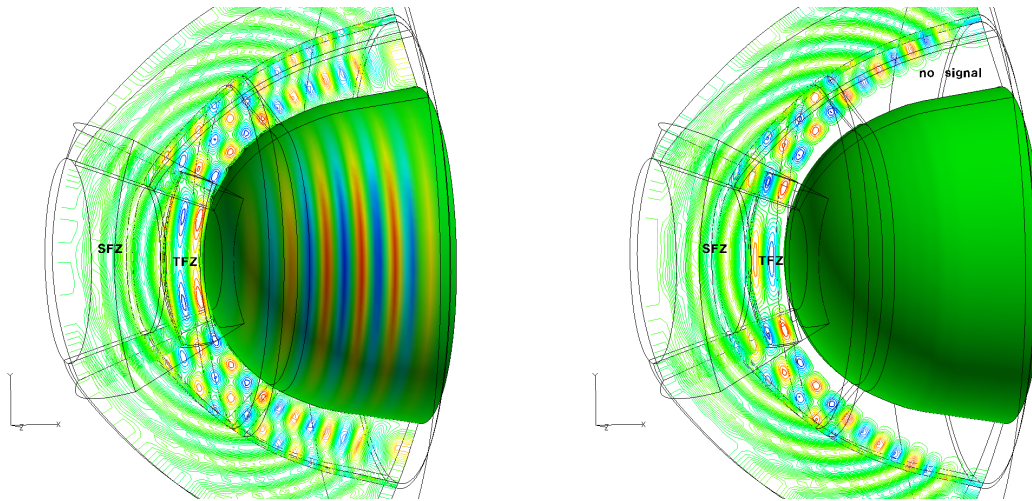


Figure 6.3: Plasma shielding incoming 9 GHz wave. Left: no plasma, right: plasma

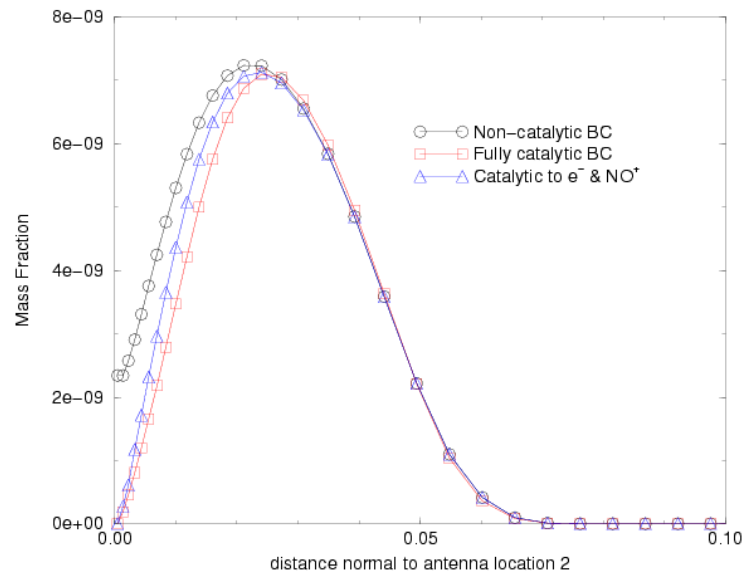


Figure 6.4: Comparison of electron density profile normal to antenna location #2 with catalytic and non-catalytic boundary conditions.

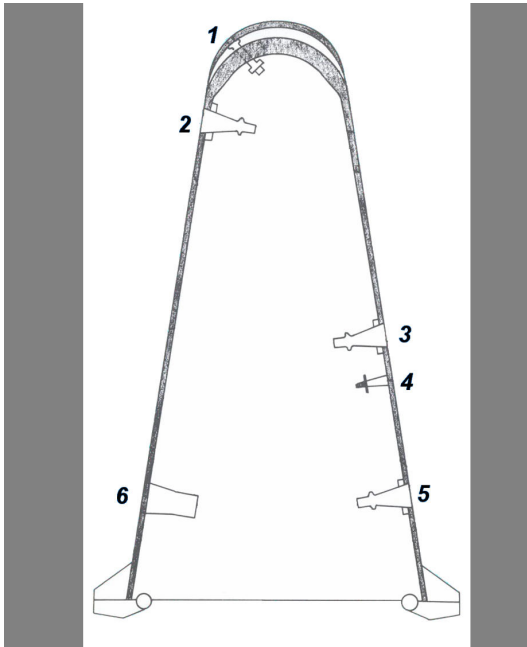
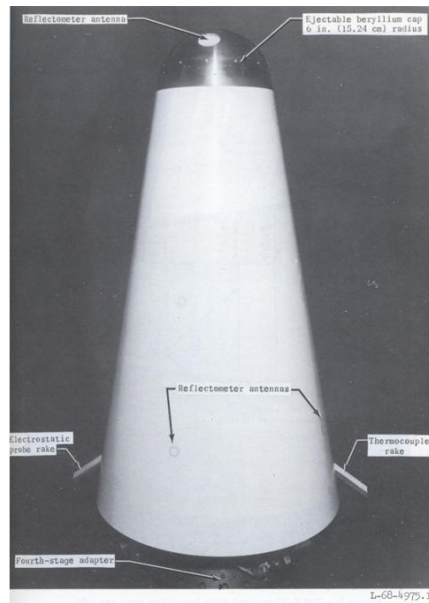


Figure 6.5: RAM C-II re-entry vehicle with locations of various antennas (ref: *NASA TN D-6062*).

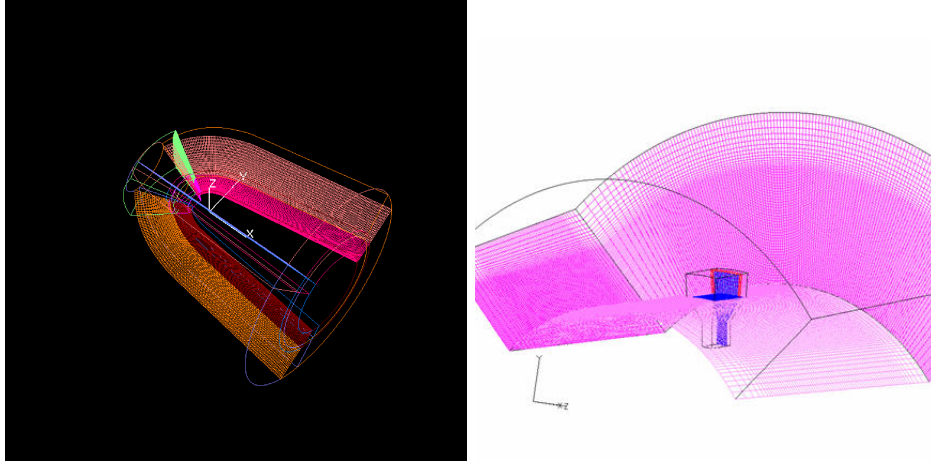


Figure 6.6: Computational grids. Left: RAM vehicle prior to decomposition. Right: Grid subset near location #2 for embedded horn.

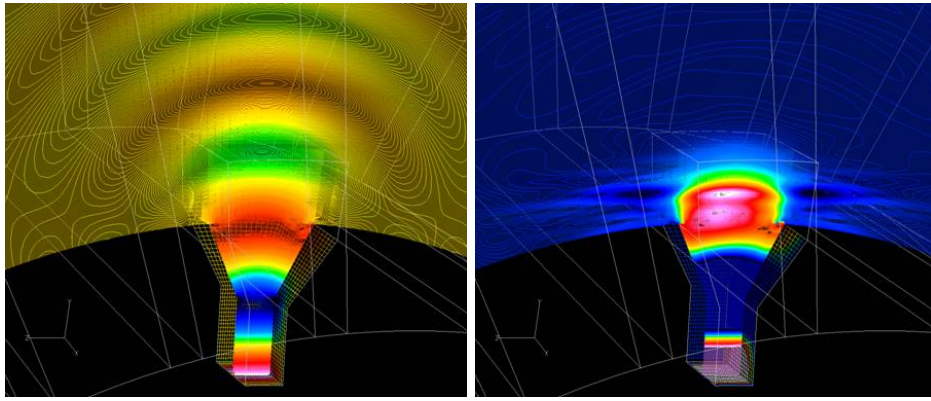


Figure 6.7: Horn driven at 9.2 GHz from antenna location #2. Left: no plasma, right: plasma

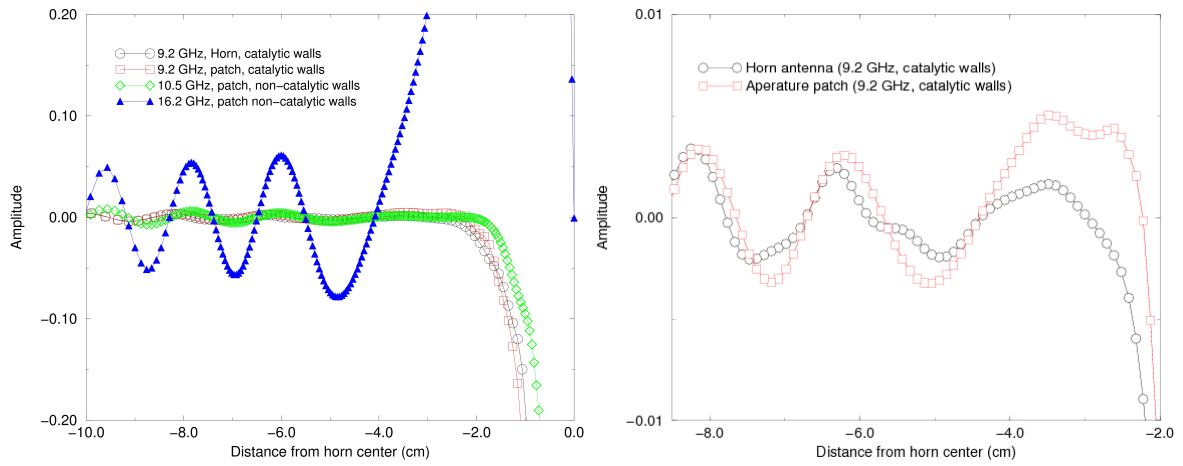


Figure 6.8: Different frequencies and different configurations for radiation from location #2.

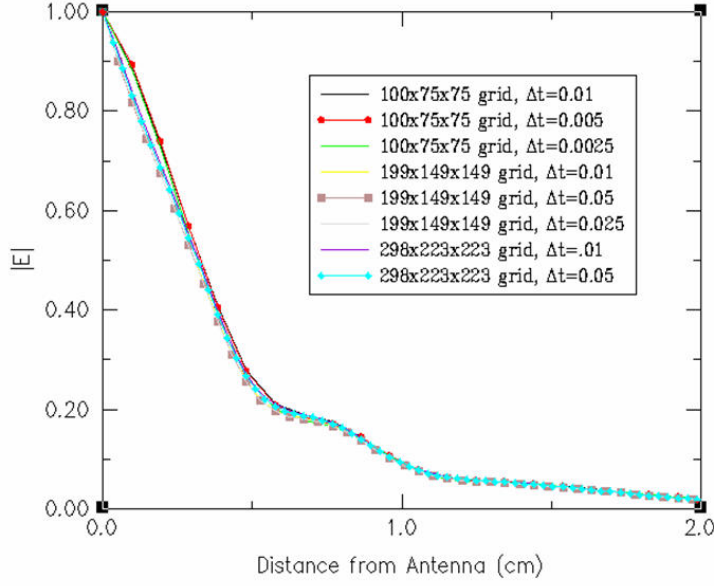


Figure 6.9: Magnitude of instantaneous electric field normal to the center of the radiating antenna for different time-steps and grid densities.

sizes. Figure 6.9 shows the grid and timestep convergence along the centerline of the antenna with the non-catalytic wall.

It turns out that retaining the extra terms in the equations had a negligible effect on the solution (difference was on the order of 10^{-5} of maximum current). In hindsight, this should not have been surprising. For the current configuration with the horn transmitting at 1 kW and an electron temperature (KT_e) of 1eV, $\Omega_p \approx 22$, $\frac{\beta}{\mathcal{M}_{th}^2} \approx 8$ and $\nu_e \approx 0.01$. While it appears that the electron density might have an effect, the factor of β in (6.32) is small enough here to preclude this. Nor would increasing the horn power (which would increase β) help in retaining the extra terms in this linear analysis. This is because the relevant characteristic parameter is $\frac{\beta}{\mathcal{M}}$ which is independent of Mach number and is approximately 2×10^{-3} .

To see this, an alternate perturbation may be defined for the number density:

$$n_e = n_{e,0} + \beta \tilde{n}_{e,1} \quad (6.51)$$

in which case (6.32) and (6.33) simplify to:

$$\partial_t \tilde{n}_{e,1} - \nabla \cdot \mathbf{J}_{e,1} = 0 \quad (6.52)$$

$$\partial_t \mathbf{J}_{e,1} = \Omega_p^2 n_e \mathbf{E}_1 + \beta_{th}^2 T_e \nabla \tilde{n}_{e,1} - \nu_e \mathbf{J}_{e,1} \quad (6.53)$$

where $\beta_{th} \equiv v_{rms}/c_0$. Therefore, in order to see an effect from the electron pressure term, the electron temperature must be significantly higher than is generated in the current conditions.

THIS PAGE INTENTIONALLY LEFT BLANK

Chapter 7

CONCLUSIONS

A higher-order compact-difference based method has been adapted to simulate aeroacoustic phenomena using the Euler and Maxwell equations. The components of the scheme include fourth and sixth-order Padé-type spatial differencing formulas coupled with up to tenth-order implicit filters which are required to maintain stability in the presence of mesh stretching and complex boundary conditions. Significant grid stretching, common in practical calculations, is shown to have profound impact on the solution, manifested in the generation of high-frequency oscillations. This characteristic is employed to positive effect in conjunction with the filtering procedure to enhance the decay of acoustic radiation outside the domain of interest. The potential of the procedure for parallel implementation is demonstrated by successful application to multidomain scattering cases. Special metric procedures are shown to be essential in the simulation of acoustic phenomena in highly curvilinear three-dimensional meshes.

A new preprocessing code *BELLERO* has been developed to automate many of the tasks associated with domain decomposition for the parallel, high-order overset-grid flow solver *FDL3DI*. Highlighted capabilities of *BELLERO* include; (1) automatic generation of the grid indices for the domain decomposition taking into account minimum stencil requirements for the high-order algorithm, (2) automatic generation of the block-level connectivity including periodic boundary conditions, (3) automated decomposition of the grid-level boundary conditions thus eliminating the need to manually specify block-level boundaries in the code, and (4) calculation of high-order interpolation coefficients and management of hole points to fully implement the high-order overset-grid (HO-OG) approach. Improvements have also been made to the *FDL3DI* solver itself in order to further enhance the overall flexibility of the HO-OG implementation. The new capability was demonstrated for benchmark problems of acoustic scattering from three circular cylinders and electromagnetic scattering from a single sphere. Development of the approach is continuing, including application on more complex and realistic problems.

The ability to extend the wave propagation to include weakly ionized gases has been demonstrated in a flexible high-order overset framework. It has been shown that the effect of adding the conservation of number density to the equation set does not improve the solution enough to justify the extra time and storage for re-entry blackout problems. Surprisingly, it has been shown that changing the boundary condition to make the electrons catalytic at the wall also does not seem to have a very large effect.

THIS PAGE INTENTIONALLY LEFT BLANK

REFERENCES

- [1] Gaitonde, D. V., Shang, J., and Young, J., “Practical Aspects of High-order Accurate Finite-Volume Schemes for Electromagnetics,” AIAA Paper 97-0363, 1997.
- [2] Tam, C. K., “Computational Aeroacoustics: Issues and Methods,” *AIAA J.*, Vol. 33, No. 10, October 1995, pp. 1788–1796.
- [3] Wells, V. L. and Renaut, R. A., “Computing aerodynamically generated noise,” *Annual Review of Fluid Mechanics*, Vol. 29, 1997, pp. 161.
- [4] Tam, C. K. and Webb, J., “Dispersion-Relation-Preserving Finite Difference Schemes for Computational Aeroacoustics,” *J. Comput. Phys.*, Vol. 107, 1993, pp. 262–281.
- [5] Holberg, O., “Computational aspects of the choice of operator and sampling interval for numerical differentiation in large-scale simulation of wave phenomena,” *Geophys. Prospect*, Vol. 35, 1987, pp. 629.
- [6] Lele, S. K., “Compact Finite Difference Schemes with Spectral-like Resolution,” *J. Comput. Phys.*, Vol. 103, 1992, pp. 16–42.
- [7] Casper, J. and Meadows, K. R., “Using High-Order Accurate Essentially Nonoscillatory Schemes for Aeroacoustic Applications,” *AIAA J.*, Vol. 34, No. 2, February 1996, pp. 244–250.
- [8] Kim, C., Roe, P. L., and Thomas, J. P., “Accurate schemes for advection and aeroacoustics,” AIAA Paper 97-2091, 1997.
- [9] Kim, C., Roe, P. L., and Thomas, J. P., “Advances in numerical boundary conditions for computational aeroacoustics,” AIAA Paper 97-1774, 1997.
- [10] Hirsch, R., “Higher Order Accurate Difference Solutions of Fluid Mechanics Problems by a Compact Differencing Technique,” *J Comput Phys.*, Vol. 19, 1975, pp. 90–109.
- [11] Visbal, M. R. and Gaitonde, D. V., “High-Order Accurate Methods for Unsteady Vortical Flows on Curvilinear Meshes,” AIAA Paper 98-0131, 1998.
- [12] Gaitonde, D. V. and Visbal, M. R., “Further Development of a Navier-Stokes solution procedure based on higher-order formulas,” AIAA Paper 99-0557, 1999.
- [13] Rizzetta, D., Visbal, M., and Blaisdell, G., “Application of a High-Order Compact Difference Scheme to Large-Eddy and Direct Numerical Simulation,” AIAA Paper 99-3714, 1999.
- [14] Ladeinde, F., Cai, X., Visbal, M., and Gaitonde, D., “Comparison of the ENO and compact schemes for DNS/LES,” *Second AFOSR Int. Conf. on Direct and Large-Eddy Simulation*, 1999.
- [15] Koutsavdis, E., Blaisdell, G., and Lyrantzis, A., “Compact Schemes with Spatial Filters in Computational Aeroacoustics,” *AIAA J.*, Vol. 38, No. 4, 2000, pp. 713–715.
- [16] Steger, J. L., Dougherty, F. C., and Benek, J. A., “A Chimera Grid Scheme,” *Advances in Grid Generation*, edited by K. Ghia and U. Ghia, ASME-FED-Vol.5, The American Society of Mechanical Engineers, 1983, pp. 59–69.

- [17] Josyula, E. and Gordnier, R. E., "Computational Simulation of the F-22 Aircraft," AIAA Paper 98-0526, 1998.
- [18] Gomez, R. J., Vicker, D., Rogers, S. E., Aftosmis, M. J., Chan, W. M., Meakin, R., and Murman, S., "STS-107 Investigation Ascent CFD Support," AIAA Paper 2004-2226, 2004.
- [19] Prewitt, N. C., Belk, D. M., and Shyy, W., "Parallel computing of overset grids for aerodynamic problems with moving objects," *Prog. Aero. Sci.*, Vol. 36, 2000, pp. 117–172.
- [20] Meakin, R. L. and Wissink, A. M., "Unsteady Aerodynamic Simulation of Static and Moving Bodies Using Scalable Computers," AIAA Paper 99-3302, 1999.
- [21] Noack, R. W. and Slotnick, J. P., "A Summary of the 2004 Overset Symposium on Composite Grids and Solution Technology," AIAA Paper 2005-0921, 2005.
- [22] Visbal, M. R. and Gaitonde, D. V., "High-Order-Accurate Methods for Complex Unsteady Subsonic Flows," *AIAA J.*, Vol. 37, No. 10, 1999, pp. 1231–1239.
- [23] Gaitonde, D. V. and Visbal, M. R., "Padé-Type Higher-Order Boundary Filters for the Navier-Stokes Equations," *AIAA J.*, Vol. 38, No. 11, 2000, pp. 2103–2112.
- [24] Visbal, M. R. and Gaitonde, D. V., "On the Use of Higher-Order Finite-Difference Schemes on Curvilinear and Deforming Meshes," *J. Comput. Phys.*, Vol. 181, 2002, pp. 155–185.
- [25] Gordnier, R. E. and Visbal, M. R., "Compact Difference Scheme Applied to Simulation of Low-Sweep Delta Wing Flow," *AIAA J.*, Vol. 43, No. 8, 2005, pp. 1744–1752.
- [26] Rizzetta, D. P. and Visbal, M. R., "Numerical Simulation of Separation Control for Transitional Highly Loaded Low Pressure Turbines," *AIAA J.*, Vol. 43, No. 9, 2005, pp. 1958–1967.
- [27] Visbal, M. R. and Gaitonde, D. V., "Very High-Order Spatially Implicit Schemes for Computational Acoustics on Curvilinear Meshes," *Journal of Computational Acoustics*, Vol. 9, No. 4, 2001, pp. 1259–1286.
- [28] Shang, J., "High-Order Compact-Difference Schemes for Time-Dependent Maxwell Equations," *J. Comput. Phys.*, Vol. 153, 1999, pp. 312–333.
- [29] Gaitonde, D. V., "Simulation of Local and Global High-Speed Flow Control with Magnetic Fields," AIAA Paper 2005-0560, 2005.
- [30] Sherer, S. E. and Scott, J. N., "High-Order Compact Finite-Difference Methods on General Overset Grids," *J Comput Phys.*, Vol. 210, No. 2, 2005, pp. 459–496.
- [31] Sherer, S. E. and Visbal, M. R., "Implicit Large Eddy Simulations Using a High-Order Overset Grid Solver," AIAA Paper 2004-2530, 2004.
- [32] Sherer, S. and Visbal, M., "High-Order Overset-Grid Simulations of Acoustic Scattering from Multiple Cylinders," *Fourth Computational Aeroacoustic (CAA) Workshop on Benchmark Problems*, NASA CP-2004-212954, 2004, pp. 255–266.
- [33] Sherer, S. E. and Visbal, M. R., "Time-Domain Scattering Simulations Using a High-Order Overset Grid Approach," 2005 Workshop on Computational Electromagnetics in Time-Domain (CEM-TD), Sept 12-14, 2005.
- [34] Grantham, W., "Flight Results of 25,000 Foot per Second Reentry Experiment Using Microwave Reflectometers to Measure Plasma Electron Density and Standoff Distance," Tech. Rep. TN D-6062, NASA, Dec 1970.
- [35] Jones, W., J. and Cross, M., "Electrostatic Probe Measurements of Plasma Parameters for Two Re-entry Flight Experiments at 25,000 Feet per Second," Tech. Rep. TN D-6617, NASA, Feb 1972.

- [36] Josyula, E. and Bailey, W. F., “Governing Equations for Weakly Ionized Plasma Flowfields of Aerospace Vehicles,” *J. Spacecraft and Rockets*, Vol. 40, No. 6, Nov-Dec 2003, pp. 845–857.
- [37] Joseph, R. M., Hagness, S. C., and Taflove, A., “Direct time integration of Maxwell’s equations in linear dispersive media with absorption for scattering and propagation of femtosecond electromagnetic pulses,” *Optics Letters*, Vol. 16, No. 18, Sept 1991, pp. 1412–1414.
- [38] Young, J. L., “A Higher Order FDTD Method for EM Propagation in a Collisionless Cold Plasma,” *IEEE Trans. Ant. Prop.*, Vol. 44, No. 9, Sept 1996, pp. 1283–1289.
- [39] Shang, J. S., “Simulating Microwave Radiation for Plasma Diagnostics,” AIAA Paper 2004-2155, Jun-Jul 2004.
- [40] Gaitonde, D. V. and Visbal, M., “High-Order Schemes for Navier-Stokes Equations: Algorithm and Implementation into FDL3DI,” Technical Report AFRL-VA-WP-TR-1998-3060, Air Vehicles Directorate, Air Force Research Laboratory, August 1998.
- [41] Pulliam, T. H. and Steger, J. L., “Implicit finite-difference simulation of three-dimensional compressible flows,” *AIAA J.*, Vol. 18, No. 2, 1980, pp. 159.
- [42] Thomas, P. D. and Lombard, C. K., “Geometric conservation law and its application to flow computations on moving grids,” *AIAA J.*, Vol. 17, No. 10, 1979, pp. 1030.
- [43] Fyfe, D. J., “Economical evaluation of Runge-Kutta formulae,” *Math. Comput.*, Vol. 20, 1966, pp. 392.
- [44] Merewether, D. E., Fisher, R., and Smith, F. W., “On implementing a numeric Huygen’s source scheme in a finite difference program to illuminate scattering bodies,” *IEEE Transactions on Nuclear Science*, Vol. 27, No. 6, Dec 1980, pp. 1829–1833.
- [45] Umashankar, K. and Taflove, A., “A novel method to analyze electromagnetic scattering of complex objects,” *IEEE Trans. Electromagnetic Compatibility*, Vol. 24, 1982, pp. 397–405.
- [46] Holland, R. and Williams, J. W., “Total-field versus scattered-field finite-difference codes: A comparative assessment,” *IEEE Trans. Nucl. Sci.*, Vol. NS-30, No. 6, 1983, pp. 4583–4588.
- [47] Friedrich, M., Gumbel, J., and Pilgram, R., “Adding generic sources to high-order finite-difference schemes,” *Workshop on Computational Electromagnetics in Time-Domain, CEM-TD 2005*, Atlanta, GA, USA, 12-14 Sept 2005, 2005, pp. 12–15.
- [48] Carpenter, M. H., Gottlieb, D., Abarbanel, S., and Don, W.-S., “The Theoretical Accuracy of Runge-Kutta Time Discretations for the Initial Boundary Value Problem: A Careful Study of the Boundary Error,” Tech. Rep. 93-83, ICASE, Nov 1993.
- [49] Alpert, P., “Implicit filtering in conjunction with explicit filtering,” *J. Comput. Phys.*, Vol. 44, 1981, pp. 212.
- [50] Vichnevetsky, R., “Numerical Filtering for Partial Differential Equations,” *Numerical Applications Memorandum (Rutgers University)*, Vol. NAM 156, 1974.
- [51] Vichnevetsky, R., “Propagation through numerical mesh refinement for hyperbolic equations,” *Math. and Comp. in Simulation*, Vol. 23, 1981, pp. 344–353.
- [52] Kurbatskii, K. A., “Analytical Solutions of the Category 1, Benchmark Problems 1 and 2,” *Second Computational Aeroacoustic (CAA) Workshop on Benchmark Problems*, NASA CP-3352, 1997, pp. 9–14.
- [53] Morris, P. J., Long, L. N., Bangalore, A., and Wang, Q., “A parallel three-dimensional computational aeroacoustics method using nonlinear disturbance equations,” *J. Comput. Phys.*, Vol. 133, 1997, pp. 56.
- [54] Barnette, D. W., “BREAKUP: A Computer Code for Parallelizing the Overset Grid Approach,” AIAA Paper 98-2732, 1998.

- [55] Chan, W. M., Gomez, R. J., Rogers, S. E., and Buning, P. G., “Best Practices in Overset Grid Generation,” AIAA Paper 2002-3191, 2002.
- [56] Suhs, N. E., Rogers, S. E., and Dietz, W. E., “PEGASUS 5: An Automated Pre-processor for Overset-Grid CFD,” AIAA Paper 2002-3186, 2002.
- [57] Benek, J., Steger, J., Dougherty, F., and Buning, P., “Chimera: A Grid-Embedding Technique,” Technical Report AEDC-TR-85-64, Arnold Engineering Development Center, April 1986.
- [58] Benek, J., Buning, P., and Steger, J., “A 3-D Chimera Grid Embedding Technique,” AIAA Paper 85-1523, 1985.
- [59] Morgan, P., Visbal, M. R., and Rizzetta, D., “A Parallel High-Order Flow Solver for LES and DNS,” AIAA Paper 2002-3123, 2002.
- [60] Blake, D. C., *Advances in Time-Domain Electromagnetic Simulation Capabilities Through the Use of Overset Grids and Massively Parallel Computing*, Ph.D. thesis, Air Force Institute of Technology, 1997.
- [61] Suhs, N. and Tramel, R., “PEGSUS 4.0 User’s Manual,” Technical Report AEDC-TR-91-8, Arnold Engineering Development Center, November 1991.
- [62] Chesshire, G. and Henshaw, W., “Composite Overlapping Meshes for the Solution of Partial Differential Equations,” *J. Comput. Phys.*, Vol. 90, 1990, pp. 1–64.
- [63] Delfs, J. W., “An Overlapped Grid Technique for High Resolution CAA Schemes for Complex Geometries,” AIAA Paper 2001-2199, 2001.
- [64] White, M. D. and Sherer, S. E., “High-Order Simulation of Communication Through a Weakly Ionized Plasma for Re-entry Vehicles,” AIAA Paper 2006-1173, 2006.
- [65] *Fourth Computational Aeroacoustic (CAA) Workshop on Benchmark Problems*, edited by M. D. Dahl, NASA CP-2004-212954, 2004.
- [66] Sherer, S. E., “Scattering of sound from a axisymmetric sources by multiple circular cylinders,” *J. Acoust. Soc. Am.*, Vol. 115, No. 2, February 2004, pp. 488–496.
- [67] Balanis, C. A., *Advanced Engineering Electromagnetics*, John Wiley & Sons, 1st ed., 1989.
- [68] Jackson, J. D., *Classical Electrodynamics*, McGraw-Hill Book Company, 2nd ed., 1990, pp. 303–306, 811–821.
- [69] Colella, P., Dorri, M. R., and Wake, D. D., “A Conservative Finite Difference Method for the Numerical Solution of Plasma Fluid Equations,” *J. Comput. Phys.*, Vol. 149, 1999, pp. 168–193.
- [70] Holt, E. H. and Haskell, R. E., *Foundations of Plasma Dynamics*, The Macmillan Company, 1965.
- [71] Chen, F. F., *Introduction to Plasma Physics and Controlled Fusion*, Vol. 1, Plenum Press, 2nd ed., June 1985.
- [72] Park, C., *Nonequilibrium Hypersonic Aerothermodynamics*, John Wiley & Sons, 1990, pp. 139–141.
- [73] Anderson, J. D., *Hypersonics and High Temperature Gas Dynamics*, AIAA, 2000.
- [74] Chase, M. W., *NIST-JANAF Thermochemical Tables*, ACS, AIP, NIST, 4th ed., 1998.

NOMENCLATURE

Uppercase variables

\mathbf{B}	Magnetic Induction
\mathcal{B}	Reference Magnetic Field
C_s	Mole-fraction of species s
\mathbf{E}	Electric Field Intensity
\mathcal{E}	Reference Electric Field
E	Energy
$\hat{\mathbf{F}}, \hat{\mathbf{G}}, \hat{\mathbf{H}}$	Fluxes
\mathbf{F}_{coll}	Force due to collisions
\mathbf{J}	Current Density
\mathcal{J}	Reference current
J	Jacobian of metric transformation
K_M	Equilibrium constant of molecule M
L	Reference length
\mathbf{M}	Magnetization
M_∞	Reference Mach number
M_{th}	Thermal Mach number
N	Atomic Nitrogen
N_2	Nitrogen molecule
NO	Nitric Oxide
NO^+	Nitric Oxide ion
O	Atomic Oxygen
O_2	Oxygen molecule
P_s	Pressure of species s
R	Residual
\mathbf{S}	Source vector
T	Temperature
T_e	Electron temperature
\mathbf{U}	Solution vector
U, V, W	Velocity components in generalized coordinates
\mathcal{V}	Reference velocity

Lowercase variables

c_0	Speed of light in free space
e	Electron, or charge of electron
k	Wavenumber
n_s	Number density of species s
m_s	Mass of species s
p	Static pressure
q_s	Charge of species s
t	Time

u, v, w	Velocity components in Cartesian coordinates
\mathbf{v}_s	velocity of species s
v_{rms}	Electron molecular velocity
\dot{w}_{sj}^d	Destruction of species s into species j
\dot{w}_{sj}^p	Production of species s from species j
\mathbf{x}	A general coordinate system
x, y, z	Cartesian coordinates

Greek variables

α	Tuning parameter for compact-differences
α_f	Tuning parameter for filters
β	Relativistic Mach number
ϵ_0	Permittivity of free space
Δ	Change of variable (i.e. $\Delta t = t^{n+1} - t^n$)
μ_0	Permeability of free space
ν_s	Collision frequency of species s
ρ	Density
τ	Reference time
θ_e	Reference temperature
ϕ	Generic scalar
ξ, η, ζ	Generalized curvilinear coordinates
ω_p	Plasma frequency
Ω_p	Non-dimensional plasma frequency

Abbreviations

AIAA	American Institute of Aeronautics and Astronautics
ASC/MSRC	Aeronautical Sciences Center Major Shared Resource Center
BC	Boundary Condition
$C4$	Fourth-order compact-difference scheme
$C6$	Sixth-order compact-difference scheme
$CnFm$	Compact-difference of order n with filter of order m
CAA	Computational Aeroacoustics
DRP	Dispersion-Relation-Preserving
E2	Second-order explicit difference scheme
ENO	Essentially Non-Oscillatory
$F8$	Eighth-order implicit filter
$F10$	Tenth-order implicit filter
$FDTD$	Finite-Difference Time-Domain (staggered grid)
HO	High-Order
HO-OG	High-Order Overset-Grid
<i>inc</i>	Incident field
JANAF	Joint Army, Navy, Air Force
LOC	Lower-Order Centered
<i>MUSCL</i>	Monotone Upstream-centered Schemes for Conservation Laws
MVG	Method of minimization of group velocity errors
OLOC	Optimized Lower-Order Centered
NASA	National Aeronautics and Space Administration
<i>RAM</i>	Radio Attenuation Measurement
<i>RK</i>	Runge-Kutta integration
<i>RK4</i>	Standard 4 th -order Runge-Kutta
<i>scat</i>	Scattered field
<i>SFZ</i>	Scattered Field Zone

<i>TFZ</i>	Total Field Zone
<i>TN</i>	Technical Note
<i>tot</i>	Total field

Codes mentioned

<i>BELLERO</i>	Preprocessing tool for high-order overset-grids (developed in-house)
<i>BREAKUP</i>	Code to decompose overset grids developed at Sandia National Laboratories
<i>FDL3DI</i>	High-order overset code to solve fluid and aeroacoustics problems (developed in-house)
<i>OHMS</i>	Overset High-order Maxwell Solver derived from <i>FDL3DI</i> (developed in-house)
<i>PEGASUS</i>	Hole cutting program for overset grids developed by NASA